Title

The Effect of Carbides on the Small-Scale Mechanical Behavior of F82H-RAFM Steel

ISBN

9798276019529

Author

Lam, Sebastian

Publication Date

2025-12-06

Peer reviewed|Thesis/dissertation

The Effect of Carbides on the Small-Scale Mechanical Behavior of F82H-RAFM Steel

By

Sebastian Ryan Lam

A dissertation submitted in partial satisfaction of the

requirements for the degree of

Doctor of Philosophy

in

Nuclear Engineering

in the

Graduate Division

of the

University of California, Berkeley

Committee in charge:

Professor Peter Hosemann, Chair

Professor Guanyu Su

Professor Andrew Minor

Fall 2025

The Effect of Carbides on the Small-Scale Mechanical Behavior of F82H-RAFM Steel

by

Sebastian Ryan Lam

Abstract

The Effect of Carbides on the Small-Scale Mechanical Behavior of F82H-RAFM Steel

by

Sebastian Ryan Lam

Doctor of Philosophy in Nuclear Engineering

University of California, Berkeley

Professor Peter Hosemann, Chair

As fusion energy is being developed, a fundamental mechanistic understanding of how materials will behave when exposed to the intense reactor environment is imperative. F82H is one of the most mature candidate materials for the structural vessel of the pioneering ITER experiment. The alloy is a tempered martensitic steel developed to withstand the fusion reactor environment however much is still not known about it. Particularly, the mechanical effects of carbide nucleation in the steel has not been deeply studied across the microstructure. To investigate this, quenched and tempered F82H needs to be mechanically investigated using small scale mechanical testing to probe individual boundaries. Small scale mechanical testing probes micron-scale volumes of material in order to understand specific material defect interactions. Using such resolved techniques will allow for conclusions to be formed about carbide precipitation and the effects on mechanical properties within different microstructural features of F82H. In general, it was found that carbide nucleation on the different features of the martensitic microstructure have widely varying effects in terms of mechanical behavior which can be explained through preferred nucleation of carbides to high angle grain boundary interfaces. In static tension loading, the nucleation of carbides along high angle grain boundaries strengthened these boundaries, while low angle grain boundaries often initiated fracture. In dynamic loading, the nucleation of carbides along high angle grain boundaries prevented their interaction with damping mechanisms. On the other hand, carbides away from high angle grain boundaries were able to interact with dislocations causing a large increase to the damping capabilities of F82H.

Table of Contents

List of Figures & Tables

List of Acronyms

ASTM	-	American Society for Testing and Materials
ATR	-	Advanced Test Reactor
ATT	-	Axial Tube Tension
BCC	-	Body Centered Cubic
BCT	-	Body Centered Tetragonal
BPP	-	Basic Performance Phase
BSE	-	Backscattered Electron
CLAM	-	China Low Activation Martensite
CRSS	-	Critical Resolved Shear Stress
D	-	Deuterium
DIC	-	Digital Image Correlation
dpa	-	Displacement Per Atom
EBSD	-	Electron Backscatter Diffraction
EDS	-	Energy Dispersive Spectroscopy
FCC	-	Face Centered Cubic
FIB	-	Focused Ion Beam
FS	-	Femtosecond
FWHM	-	Full Width Half Max
HAGB	-	High Angle Grain Boundary
HAZ	-	Heat Affected Zone
HCP	-	Hexagonal Close Packed
INL	-	Idaho National Laboratory
IPF	-	Inverse Pole Figure

ITER	-	International Thermonuclear Experimental Reactor
KW	-	Kammrath-Weiss
LAGB	-	Low Angle Grain Boundary
LMIS	-	Liquid Metal Ion Source
LWR	-	Light Water Reactor
M	-	Metal
ND	-	Normal Direction
PAG	-	Prior Austenite Grain
PI	-	Picoindenter
RAFM	-	Reduced Activation Ferritic Martensitic
RD	-	Rolling Direction
RHT	-	Ring Hoop Tension
SDOF	-	Single Degree of Freedom
SE	-	Secondary Electron
SEM	-	Scanning Electron Microscope
SSMT	-	Small Scale Mechanical Testing
T	-	Tritium
TD	-	Transverse Direction
TEM	-	Transmission Electron Microscope
uMS	-	Micromechanical Spectroscopy
UTS	-	Ultimate Tensile Strength
WCCB	-	Water Cooled Ceramic Breeder
Zry-4	-	Zircaloy-4

Chapter 1

Introduction

1.1 A Brief History of Nuclear Power

Fission based nuclear power is an essential part of the global power grid supplying approximately 10% of the world's energy demand and around 20% of America's energy demand [1,2]. At first, nuclear energy figuratively exploded in the years following World War II leading to the "nuclear renaissance" of power generation. There were numerous reasons for this spike in nuclear interest including desires for geopolitical dominance through advanced technologies, positive public perception of nuclear industry, fears of heavy reliance on oil, and an unprecedented push for research into nuclear technology just to name a few [3]. The atomic age was upon the world as nuclear tech was seen as a solution to everything. Cosmetics laced with radioactive elements and radon infused drinking water were sold as health products [4]. Even the vast majority of nuclear power plants were commissioned in the 70s and 80s due to this hopeful optimism on nuclear tech [5]. However, the figurative explosion in nuclear technologies turned into fear as literal explosions occurred at nuclear plants. Whether due to operator error or inherent design flaw, these mistakes set the stage for the beginning of the tragic history of nuclear energy. Accidents at the Chernobyl nuclear power plant in 1986 and Fukushima Daiichi nuclear power plant in 2011, political squabbles over nuclear waste, and anti-nuclear war sentiment tarnished the relations of nuclear energy with the public [3]. Hope turned to distress as ideas of nuclear technology being the high-tech solution to everything were replaced with fears of an invisible threat. Still to this day, media portrayal of nuclear power to the public often evokes images of Godzilla, superpowers, or hydrogen bombs breeding fear into the use of the promising technology.

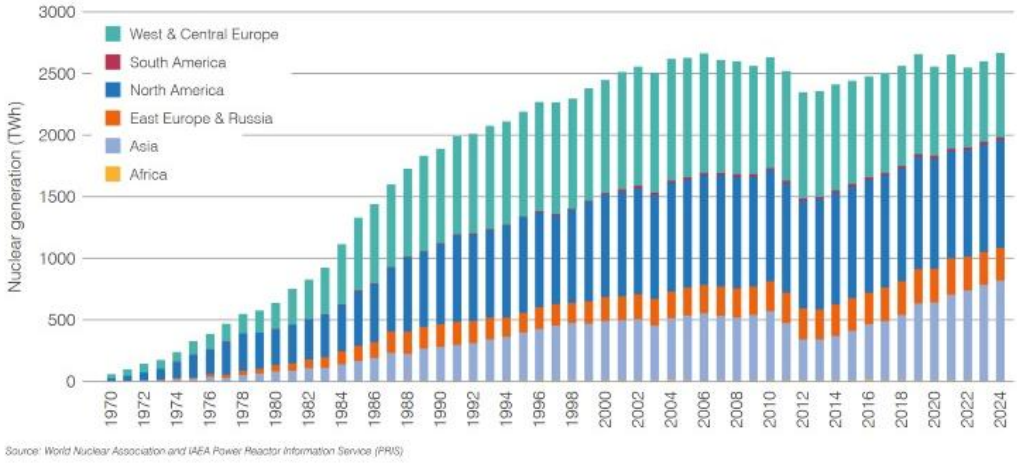

Figure 1 Total nuclear power capacity over time in different areas of the world [1,2]

Many of the initial nuclear reactors built during the 80s which are now reaching their quoted 40-year lifespans leave many countries with the big question of whether to renew these leases, expand nuclear reactor development, or dismantle the technology entirely [5]. Some countries like Germany have already made the decision to decommission all nuclear plants and decrease reliance on nuclear technology due primarily to public opinions souring.

On the other hand, we have global warming, another invisible danger which threatens to cause catastrophe. The global community is mostly united against the threat of global warming, aware of the threat it will pose in the future. Nuclear energy has been repeatedly proposed as a carbon emission free remedy for the looming global warming crisis. Since no part of the ideal nuclear fuel cycle involves the production of carbon emissions it has been viewed as a realistic part of the solution to reducing man-made greenhouse gas production. However, as concern of global warming grows larger every year, views of nuclear energy have never been more divided. Advocates see it as a saving grace from the clutches of global warming and critics see it as a vehicle to invisibly poison the public. Only time can tell whether nuclear energy will become a crucial component of the global warming challenge or if it will fade into obscurity. If nothing changes, estimates of nuclear power's impact on the reducing carbon emissions look bleak [6].

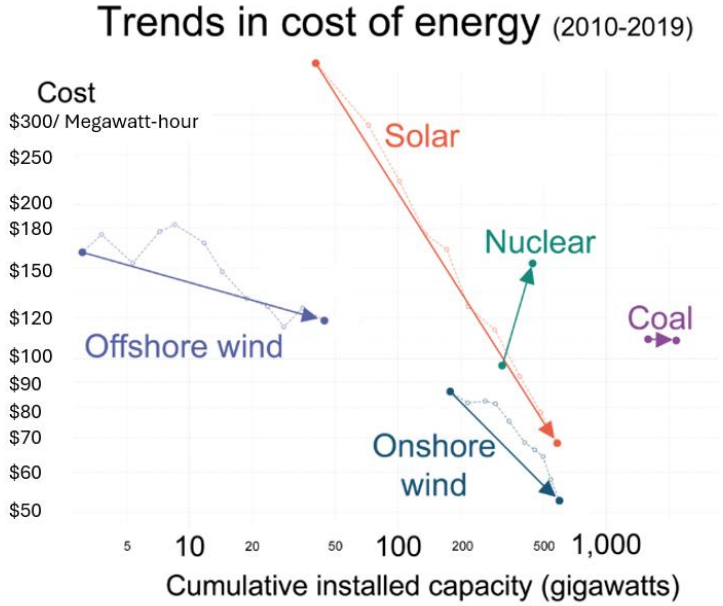

Figure 2. Levelized cost of energy of different energy sources from 2010-2019 [7].

The nuclear equation is one which balances nonproliferation, defense, global warming, economics and public health. All these factors are unmistakably intertwined into the politics of the advancing nuclear energy in every country. But the deciding factor in the battle for nuclear energy will inevitability be the change or lack thereof in public opinion. The influence of public opinion has a massive, understated influence over the future of nuclear power due to the poor economics of building a single nuclear reactor [8,9]. Once built, nuclear reactors are monetarily competitive with their alternatives if not better. Yet, the astronomical up-front capital expenditure and long construction time frames for a single unit compared to solar and fossil fuel plants make it a risky investment for private equity [10]. It has been decades since the last nuclear reactor started construction in the US and if this trend continues, the industrial knowledge of building reactor

components is bound to be lost and become prohibitively expensive to relearn. In the US, you can purchase a home solar system for $10,000 but for nuclear on the other hand, a power plant with a 1GW capacity is expected to cost somewhere in the ballpark of $6 billion to $15 billion to construct which is extremely risky for even the most speculative of private investment [11]. With this bleak economic situation, public opinion on nuclear technology becomes a heavy influence on the prospects of fission power. Passing bills like carbon taxes, providing subsidies, more government funding, approving of geological repositories, and increasing speculative investment in nuclear energy are all potential benefits of a positive public perception [11]. This benefit can be seen in the rise of renewable energy sources which experiences massive public approval and governmental subsidies to the point of it being commonplace in many American households. Approval for nuclear power is much higher in the younger generations, which might prove to be the light at the end of the tunnel for fission reactors but with legislation stalling, the prospects of nuclear energy look bleak [12].

The term nuclear power typically refers to fission based nuclear power plants. Though, a new contender in the nuclear power space is beginning to gain widespread appeal called nuclear fusion or fusion power. The sentiment of negativity and fear entirely changes when talking about fusion power which is marketed as the ideal energy source. It's carbon-emission free, futuristic, powered by water, and best of all, has (mostly) no radioactivity. Estimates even say that if the entire world was powered off fusion energy, we would have enough fuel to last us longer than predictions for when the Sun would collapse [13,14]. What is there to hate about infinite, carbon free power? These prospects almost seem too good to be true, with many startups and international collaborations being developed in the pursuit of this futuristic concept while making grand promises.

Commonwealth Fusion Systems promises a commercially available fusion reactor by 2027 [15]. Pacific Fusion lead the largest Series A funding round in 2023 with more than $900 million raised and pledges to have a grid connected reactor in the late 2030s [16]. Inertia Enterprises, founded by the lead designer of the groundbreaking NIF experiment, formed in 2025 promising cheap laser based inertial fusion [17]. Around the world, more than 50 startups and 50 publicly funded fusion projects are chasing the goal of developing commercialized fusion energy. The only problems seem to be that only one of these projects has reached the point where it could (theoretically) generate a positive amount of energy and the most mature project, the International Thermonuclear Experimental Reactor (ITER), is heavily over budget and constantly 30 years away from operation [18].

1.2 Fusion Energy

	Thermonuclear Fusion Reaction	Probability	Q MeV
1	${}^{2}_{1}D+{}^{2}_{1}D \rightarrow {}^{3}\mathrm{He} + \mathrm{n}$	50%	3.269
2	${}^{2}_{1}D+{}^{2}_{1}D \rightarrow {}^{3}_{1}T + \mathrm{p}$	50%	4.033
3	${}^{2}_{1}D + {}^{3}_{1}T \rightarrow {}^{4}\mathrm{He} + \mathrm{n}$	100%	17.589
4	${}^{2}_{1}D + 3\mathrm{He} \rightarrow {}^{4}\mathrm{He} + \mathrm{p}$	100%	18.353
5	${}^{3}_{1}T + {}^{3}_{1}T \rightarrow {}^{4}\mathrm{He} + 2\,\mathrm{n}$	100%	11.332
6	${}^{3}_{1}T + {}^{3}He \rightarrow {}^{2}_{1}D + {}^{4}He$	43%	14.320
7	${}^{3}_{1}T + {}^{3}He \rightarrow p + {}^{5}He$	6%	14.320

Figure 3. Typical fusion reactions expected in a fusion reactor with listed Q value [19]

Fusion operates on the basic concept of the deuterium–tritium (DT) fusion reaction. When gaseous deuterium (D) and tritium (T) are brought together in a high-pressure, high-temperature environment, they can overcome their mutual Coulombic repulsion and fuse to form helium and a high-energy neutron. This exothermic reaction releases a total energy of approximately 17.6 MeV [19]. While this is the primary reaction expected, many other reactions occur within the plasma as more fusion products form shown in Figure 3. The underlying nuclear reaction is the same process that fuels the Sun and the hydrogen bomb where the fusion of light nuclei into heavier ones releases vast quantities of energy according to Einstein's mass-energy equivalence principle, $E=mc^2$. In a theoretical reactor environment, the energetic helium ions remain magnetically confined and contribute to maintaining the plasma temperature from further reactions and collisions, while the fast neutrons escape confinement and deposit their kinetic energy into surrounding structural materials and coolants through elastic collisions. The heat extracted from this neutron energy can then be transferred using a coolant loop, transferred to steam turbine setup, and generate useful electrical energy [13].

All fusion systems are aimed at making a device which is able to fuse D and T in an environment which is hot enough and pressurized enough for a long enough time to achieve fusion. The Lawson criterion is a figure of merit which defines these conditions under which a fusion plasma can produce more energy than it loses. Following this point, the fusion reaction becomes self-sustaining and achieves ignition. This criteria was first proposed by John Lawson in 1955 and evaluates the balance between energy generated by fusion reactions and energy lost through radiation and particle escape. In its original form, Lawson expressed is as the product of the plasma density n_e and the energy confinement time τ_e. When $n_e\tau_e$ exceeds a critical threshold then ignition is achieved. This was expanded later to the fusion triple product, which adds a third factor, plasma temperature T, to capture the full physics required for practical reactors. The higher the triple product $n_eT\tau_e$, the closer the system is to reaching ignition [13]. This criterion is frequently used as a benchmark for evaluating how close projects are to achieving fusion ignition shown in Figure 4.

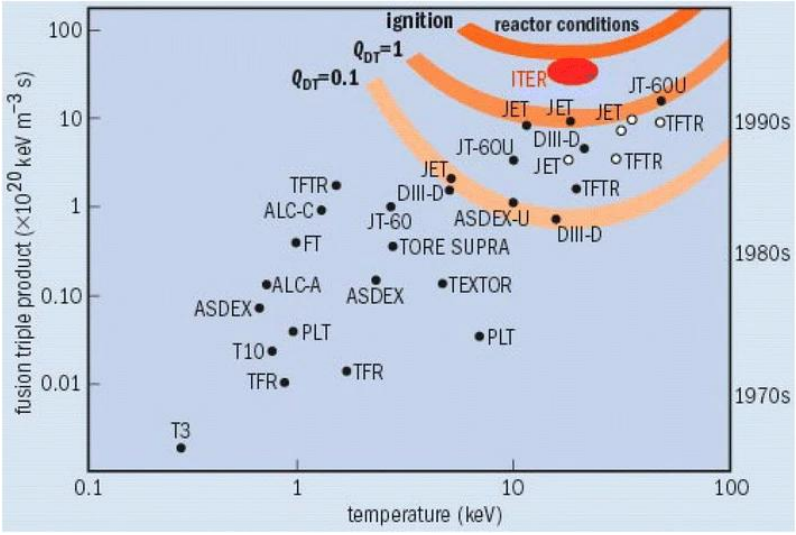

Figure 4. Fusion triple product plotted for different experimental fusion reactors [20].

If or when a reactor is able to consistently achieve fusion ignition and a commercial scale reactor is developed as a result, the benefits that fusion energy offer over fission energy are immense. Theoretically the framework for fusion energy is simple: a reaction chamber filled with hot gaseous D and T needs to be compressed and heated until fusion is achieved. The heat of the fusion reaction can be siphoned to boil water and spin turbine systems to generate useful electrical energy. Early nuclear scientists, encouraged by the rapid postwar advances in nuclear fission, initially believed that practical fusion power would be achieved within a few decades by the 1990s [21]. The theoretical foundation appeared solid, and the technological hurdles were assumed to be surmountable with the same momentum that had led to the successes of fission power and the space race. However as of today, the goal of commercialized net-positive fusion energy remains unachieved. The joke within the nuclear community that fusion energy is always 10 years away lies as a constant reminder of the magnitude of the challenge fusion energy poses [21]. This immense delay in expectations can largely be attributed to the immense technological challenge that fusion presents.

There are currently several technological approaches to fusion energy which are being pursued by a variety of private startup companies, national labs, and international collaborations. The magnetic confinement method pursued by ITER has been in development since the 1950s and is easily the most researched fusion approach. In magnetic confinement fusion (MCF) powerful magnets take advantage of magnetic-electric field interactions to confine hot D-T plasma in a toroidal shaped reactor [13]. Alternative approaches, such as inertial confinement fusion (ICF), magnetic mirror devices, stellarators, and other unique concepts offer tradeoffs between confinement, scalability, and engineering feasibility. In ICF for instance, powerful lasers are used to directly or indirectly compress tiny hydrogen fuel pellets to extreme densities and temperatures, triggering fusion reactions for brief periods. The National Ignition Facility (NIF) in the United States achieved a major milestone in 2022 by producing a fusion reaction that generated more energy than was delivered to the target landmark step for the fusion community [22]. However, the overall system energy efficiency remains far below breakeven and the scaleup prospects of such a device into a commercialized energy generation system remain dubious, giving rise to interesting discussions into the actual purpose of ICF devices. The most promising approach which

has seen the most successes in achieving fusion milestones so far has been the magnetic confinement method followed by ITER [13]. Nevertheless, only time will tell if ITER is able to succeed in its initial goals of achieving sustainable, commercialized fusion energy.

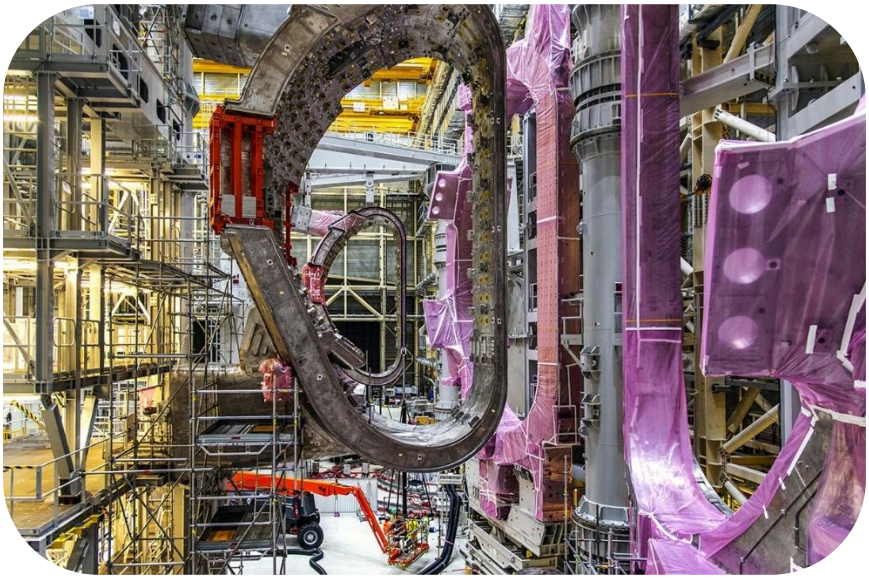

Figure 5. ITER progress in 2024 before announcing first ignition delay to 2034 [23].

It is often said that ITER is the greatest scientific endeavor of modern times and poses a challenge equal to this magnitude [24]. The sheer complexity of ITER can be seen in the conceptual images of the reactor shown in Figure 5 and Figure 6. The ITER experiment combines of multiple disciplines all aiming at the goal of developing a commercial, sustainable route towards fusion power. Plasma physics, materials science, and nuclear engineering intersect in a big optimization problem balancing tradeoffs between the different fields of study. Just from the materials science view of reference, the engineering challenge is immense and requires specifically tailored materials to resist the intense fusion energy environment generated within the reactor.

However beyond concerns of physics and engineering lies even more questions of economics and scalability. If or when ITER successfully demonstrates net energy gain, translating that success into a commercial power plant will require a new generation of reactors capable of continuous operation, automated tritium breeding and handling, efficient heat extraction, and robust materials capable of decades-long operation under the intense fusion environment. The economic viability of fusion energy will depend on minimizing capital costs and ultimately competing with other energy technologies such as advanced fission reactors, solar, and wind [25,26]. Fusion energy promises a technology which could shake geopolitical order, stave off global warming, and secure humanity's energy future for the indefinite future, but even with all the research done so far, the journey ahead looks arduous, fraught with countless obstacles. However "nothing ventured, nothing gained" and the benefits can only be realized if the immense technical challenges are overcome.

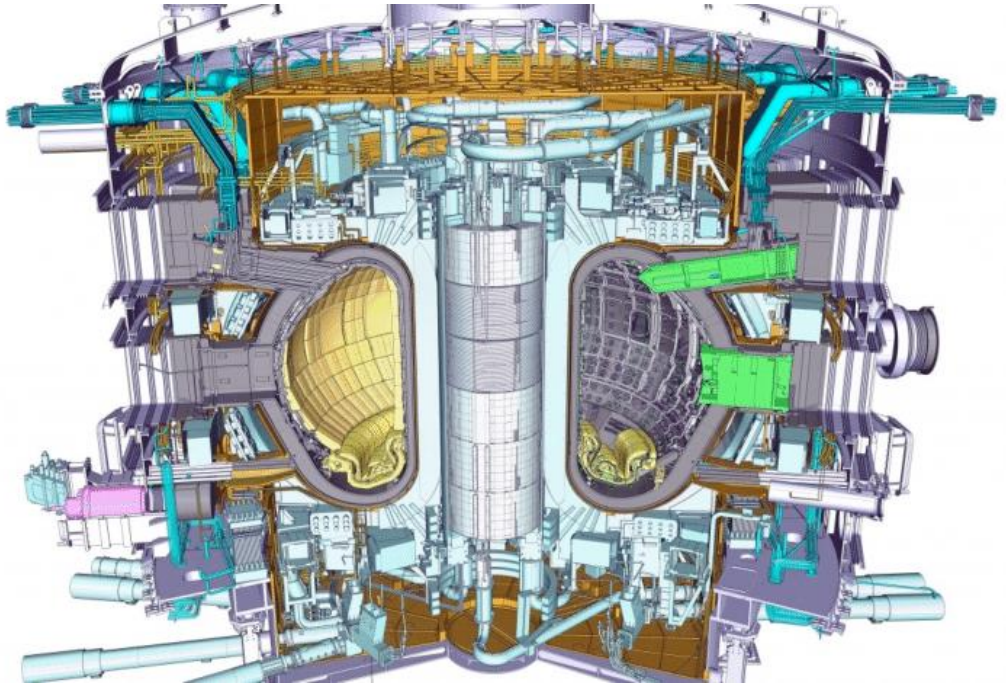

Figure 6. Conceptual design of ITER showing the primary vessel and supporting components [27].

1.3 Materials Challenge of MCF and ITER

One of the biggest roadblocks in the development of ITER is the materials challenge: the challenge of researching, manufacturing, and machining materials capable of resisting, controlling, and containing the intense environment created within the fusion reactor [28,29]. Thermal, radiation, mechanical, corrosion, and magnetic effects all combine within the reactor, requiring specifically tailored materials capable of withstanding these conditions. Thermally, the temperature of the plasma is often quoted in excess of 100 million degrees Celsius, much hotter than the melting temperature of any known material. While this will be confined by magnets, some of this heat will reach the first wall of the vacuum vessel and demands a material resistant to these thermal fluctuations. Radiation from the fusion reactions will bombard the reactor material causing microscopic radiation damage that accumulates and serves to weaken the entire structure. Mechanically, pressure differences and magnetic forces will stress, fatigue, and twist components during reactor operation [29,30]. On top of this, corrosion from coolant flowing through pipes will serve to degrade tubes and structures over time. These challenges present a unique problem in choosing materials which optimize all of these conditions and can be put into service for an extended duration without replacement.

1.3.1 Mechanical Properties of Materials

Understanding the mechanical properties of materials is fundamental to explaining how solids behave when subjected to forces, and it forms the basis for designing durable structures. Leonardo Da Vinci pioneered the subject through his exploration into testing the strength of wires. His wire experiments, aimed holding heavy baskets with thin metal wires, concluded that strength

of the wires were both a function of the force applied and the cross sectional area of the wire, forming the fundamentals of strength measurement [31]. Modern day mechanical testing uses these fundamentals and tests a material's response to applied stress. Stress is typically defined as the force per unit area applied to a material, in units of pascals (Pa). When a material is loaded with this stress, it deforms, and the amount of deformation per unit length is called the strain. By applying a controlled load through a precise mechanical testing setup and measuring the corresponding deformation a stress-strain curve can be extracted, which describes how a material behaves under mechanical loading.

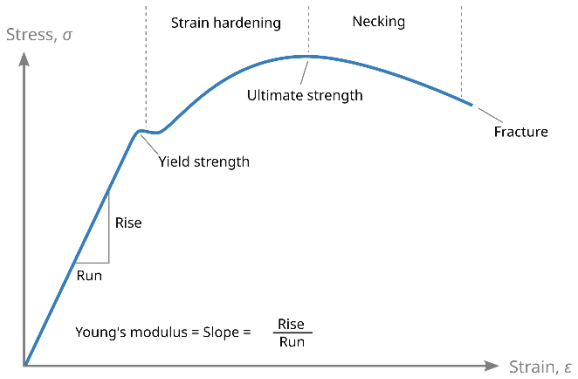

Figure 7. Typical tensile stress strain curve with labelled features [32].

A typical tensile stress-strain curve, like the one shown in Figure 7, begins with a linear region where stress and strain are directly proportional called the elastic regime. Within this region, the material will return to its original shape if the load is removed. The slope of this linear portion is the elastic or Young's modulus and quantifies the material's stiffness. Materials with a high modulus resist deformation like steel while a low modulus indicates greater flexibility like a rubber band. Beyond the linear elastic region, the yield strength of a material is reached, and the material enters the plastic regime where deformation is permanent. Here as the material is stretched, defects are generated within the material, causing the material to gain hardness (strain hardening) until an eventual breaking point. In ductile materials like copper or aluminum, the curve typically rises to a maximum stress which the material can withstand called the ultimate tensile strength (UTS). After this peak, necking and eventual fracture occur. The exact magnitude and shape of these features on the stress-strain curve are extremely material dependent and can be related to deformation mechanisms of the individual material. Brittle materials like ceramics, behave differently form metals showing little to no plastic deformation and often fracture suddenly.

Materials often behave differently when loaded in different ways. Stress-strain curves often depict mechanical testing when simple compression (push) or tension (pull) forces are applied to materials. However, in most real world scenarios, parts with complex geometries are manufactured with various loading conditions, seemingly limiting the utility of simple stress-strain curves from simple compression or tension experiments. However, most stress states on structures can be simplified to a combination of tension and compression forces. Combined with computational tools like finite element analysis (FEM) or on the analysis of simple structures like tubes or beams, simple compression and tension testing probing material properties becomes integral part in engineering design of mechanically safe structures. Mechanical testing encompasses various

methods, each highlighting different material properties. Tensile tests measure strength and ductility by pulling apart materials samples. Compression tests measure strength under pushing forces. Flexural and bending tests using cantilevers or bars measure strength and deflection under a mixed compression and tension state. Other specialized tests like hardness measurements, Charpy impact tests, and fatigue tests probe different parts of mechanical behavior like resistance to plastic deformation, fracture, or under dynamic loading conditions. Multiple small scale mechanical tests are shown in Figure 8. These all together provide essential insights into how materials respond to forces to predict performance.

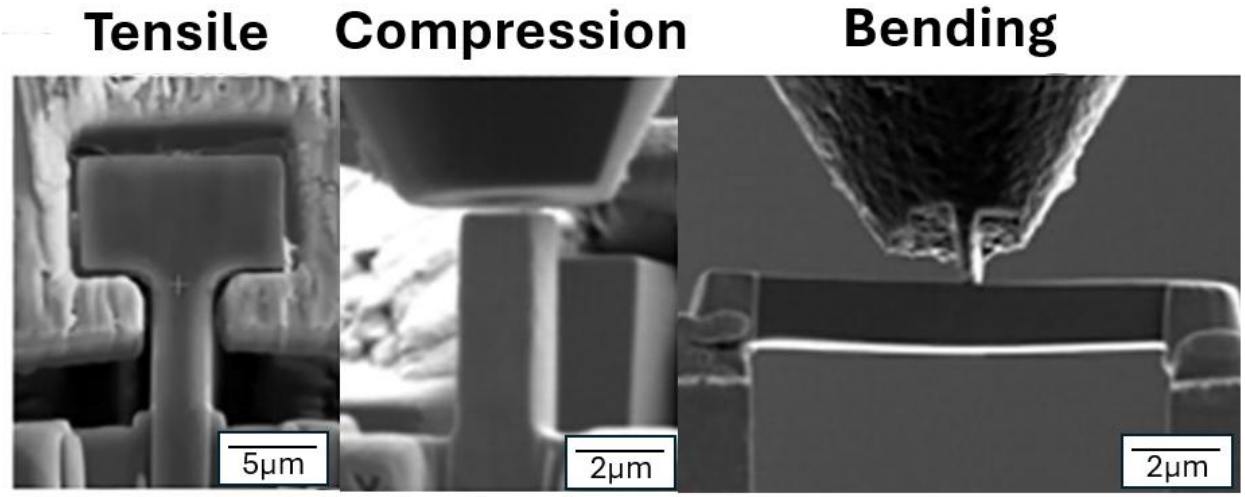

Figure 8. Small scale mechanical testing for tension, compression and bending tests [33].

Mechanistically, the onset of plastic deformation in materials is heavily governed by the movement of dislocations. Dislocations are line defects which break the periodicity of a lattice and allow for a low energy pathway for atomic planes to slip past each other under an applied stress. The interactions of these dislocations with other defects within a crystal lattice like grain boundaries, precipitates, and other dislocations are key in the mechanistic understanding of material deformation. Many strengthening mechanisms explored throughout this dissertation are directly linked with the impedance or facilitation of dislocation motion within the lattice. These interactions form some of the absolute fundamentals of the complex behavior of matter and thus is an extremely active area of research being constantly expanded.

The engineering platitude of “leakage before breakage” explains that slow failure of component is desired over fast catastrophic failures. For a structure, visible signs of degradation which can be addressed like a leak are greatly preferred to total breakage of a system. This manifests itself in ductility and strength being key factors for material property selection. For this reason, the understanding of mechanisms for why materials might become brittle or lose strength and relating this to the mechanistic understanding of dislocation motion are important. While mechanical properties are one of the most important factors in materials selection other factors like cost, machineability, weldability, corrosion resistance, radiation resistance, among many others, need to be assessed and optimized for an ideal material.

1.3.2 Radiation Damage in Materials

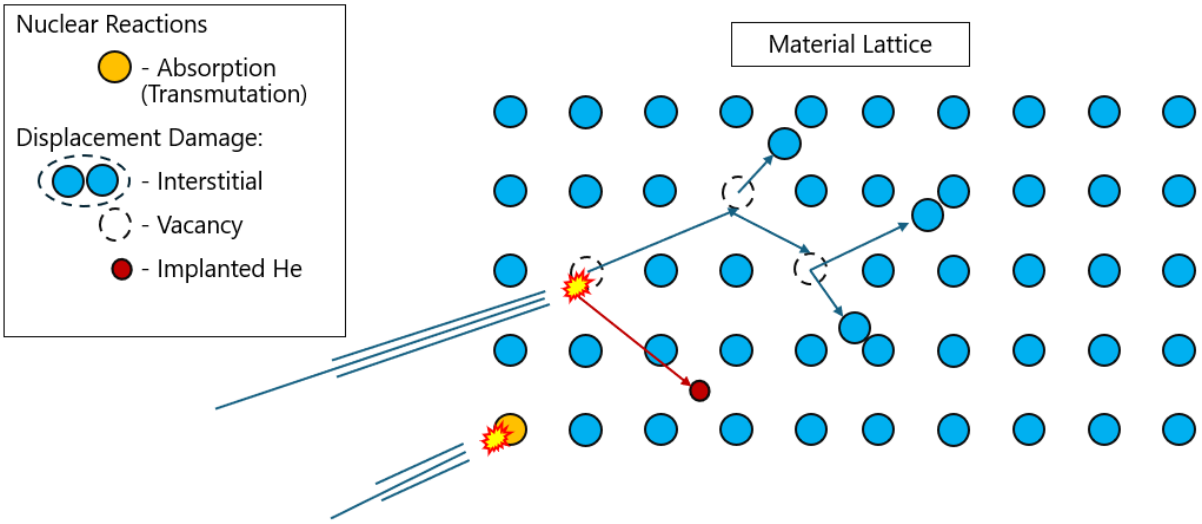

Figure 9. Basic schematic of radiation damage in materials

Radiation damage in materials is particular concern within fusion environments and cause a wide variety of degradation mechanisms. In a fusion environment a variety of damaging radiation is expected to reach both the structural materials and first wall of a fusion reactor. Among these are fast neutrons and escaped plasma ions like D, T, and He which are all expected to have a significant effect on the properties of the materials within the fusion reactor. The mechanisms and effects of radiation on materials are a widely studied field encompassing aerospace, fission reactor, fusion reactor, accelerator, and medical applications. Most measured effects of radiation on materials are negative, due to the chaotic nature of the interaction, serving to embrittle, weaken, and introduce defects into the host material, however this can sometimes be leveraged in cases like radiation therapy or isotope production [34]. When energetic particles hit a lattice of material, their interactions disrupt the atomic structure of the material, generating defects that can drastically alter its physical and mechanical properties. Understanding the processes that govern this damage, from the initial collision events to the long-term evolution of defects, is therefore central to predicting and improving materials performance in radiation environments.

When an energetic particle such as a neutron or ion penetrates a solid a wide variety of reactions can happen [35]. Most commonly, the atom strikes a lattice atom, transferring a portion of its kinetic energy through an elastic collision much like a billiard ball. The first atom in the lattice to receive a significant recoil energy is called the primary knock-on atom (PKA). If the PKA has sufficient energy it can be displaced from its lattice site, creating a vacancy and an interstitial atom (Frenkel pair). With enough energy this PKA can displace other atoms, generating a chain of further displacements known as a displacement cascade. This simple interaction is the foundation of much of the radiation damage in materials and the unit of displacements per atom (dpa) is typically used to assist in quantification. The Kinchin-Pease (KP) model, shown in Figure 10, was proposed to describe the energy barrier for displacement generation and is the foundation for radiation damage quantification. The model idealizes the elastic collisions initiated by a PKA on a lattice. Here it is assumed that there is a threshold displacement energy, E_d, below which no permanent atomic displacement occurs. PKA energies are then divided into discrete regimes of

displacement generation. For a PKA energy of $E<E_d$, the lattice remains intact the PKA energy is too low to cause a displacement, and nothing occurs. For $E_d<E<2E_d$, a single Frenkel pair is formed. Above $2E_d$ the number of displacements scales approximately linearly with PKA energy, approximating an idealized collision cascade. Finally at higher energies above a threshold critical or cutoff energy, E_c, the KP model saturates at a constant value of displaced atoms, to show that only a fraction of the PKA's kinetic energy remains available for displacement generation.

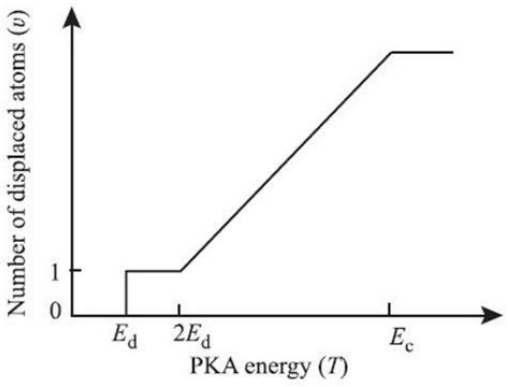

Figure 10. Kinchin-Pease model for radiation damage [36].

While simple in ideation, the KP model provides a conceptual foundation for quantifying radiation damage in terms of dpa. However one major drawback in all dpa estimations is the lack of direct observability or measurement. When the displacement cascade is generated, a majority of the displacements and Frenkel pairs generated recombine within the lattice, effectively negating the radiation damage event. This phenomena known as recombination is directly linked to the diffusion of atoms within a lattice and is hence governed by time and temperature. Due to recombination, much less of the actual dpa assessed by the KP model is actually incorporated as permanent defects within the lattice. While modern day transmission electron microscopy (TEM) is resolved enough to view atomic arrangements in thin foil materials allowing for dpa estimation, this does not account for the fact that many of the initial collision cascades have already recombined or have been allowed to coalesce into other defect clusters. From this perspective, estimation or quantification of radiation damage is particularly challenging. Time following irradiation, irradiation temperature, irradiation time, material analyzed, recombination rate, defects generated, radiation energy, and radiation fluence, all ideally interact to form the basis for an ideal model for radiation damage quantification. The KP model has been refined over time with multiple corrections and modifications to account for some of these phenomena [37–39]. Most commonly, the Norgett–Robinson–Torrens (NRT) modification and molecular-dynamics (MD) based damage functions have been used to account for gaps in the KP model.

The permanent displacements from the radiation damage interaction when left to accumulate over long irradiation times are the basis for much of the bulk changes in irradiated materials. MD simulations have been used to model the timescales of radiation interaction in materials like the one shown in Figure 11. Nordlund et al. estimates that permanent damage due to the displacement cascade forms within 100ps of the radiation interaction [40]. However past 100ps, the radiation defects generated begin to mobilize where the agglomeration, coalescence,

and interactions of these of all these defects can cause measurable property changes such as swelling, segregation, hardening, or embrittlement [35]

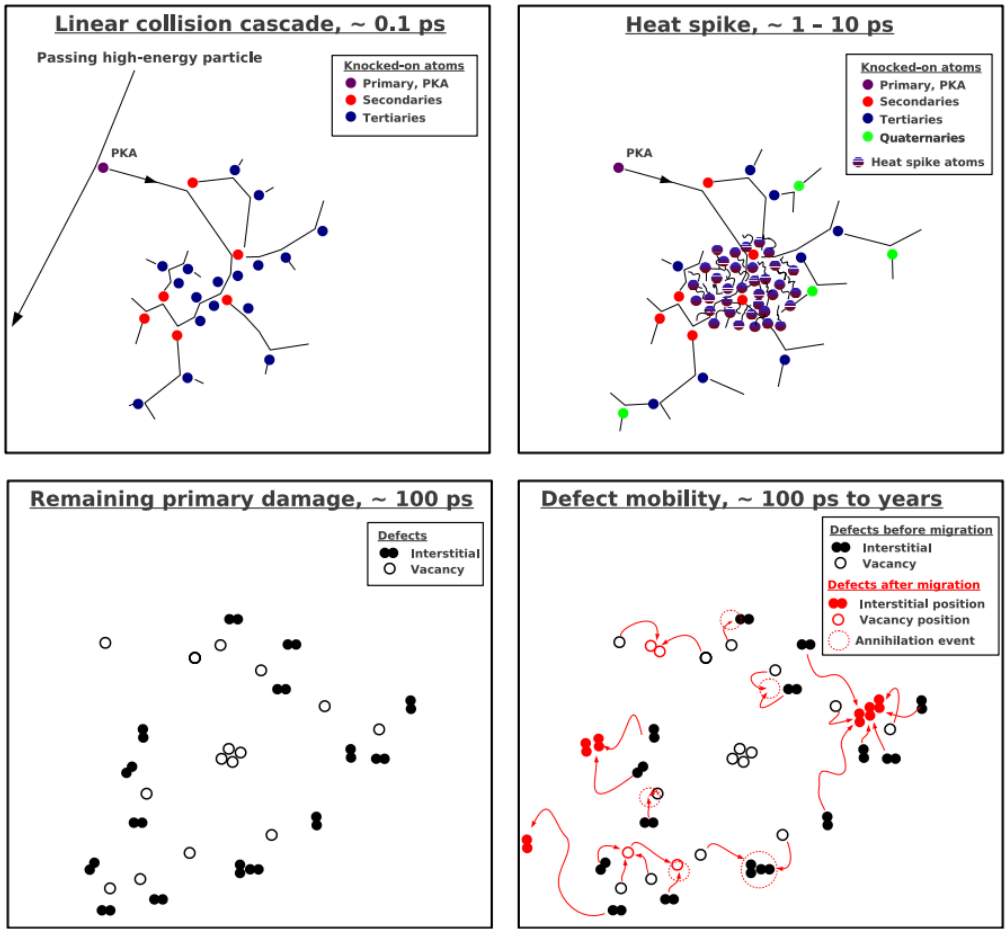

Figure 11, Timescales of defect evolution due to a radiation damage event [40].

Void swelling is a primary concern in irradiated materials. Irradiation at elevated temperatures can lead to the formation and growth of voids and inert-gas bubbles. First observed in the late 1960s, voids, formed from clusters of vacancies, in certain materials can reach densities and sizes large enough to produce volumetric swelling of irradiated materials. Due to the geometrical changes of void swelling, parts not only lose density and strength, but can exert external stresses on nearby parts. Bubbles, similar in their vacancy-driven formation mechanisms, form through transmuted and implanted gases like helium which can agglomerate into large clusters. At ITER, the first-wall experiences high gas implantation, leading to bubble formation while the high radiation fluxes can cause extensive void formation in certain materials. Bubbles which can evolve into blisters, upon reaching a critical pressure can burst, causing delamination of a small layer of material which can introduce plasma impurities into the reactor system. The underlying mechanisms of void and bubble nucleation and growth is a large area of research looking to identify the key factors governing their evolution. Mitigation of both void swelling and bubble/blister formation is key for materials used for the ITER breeding blanket. The first wall experiences the highest degree of bubble and blister formation and is the first barrier against the intense fusion environment. Tungsten is the most mature candidate material for the first wall and

has been shown to sufficiently protect against bubble and blister formation in the short term [41,42]. The results of reactor relevant implantation energies and fluences on blistering on a long time scale remain to be seen. Void swelling is a large concern for the surrounding structural material of the fusion reactor vessel. Austenitic steels, while initially pursued for fusion energy structural material applications, was found to have very high void swelling rates, attributed to its FCC crystal structure and associated high vacancy diffusion rates [43]. An extreme example of a fission reactor irradiated piece of 316 steel is shown in Figure 12. Following this, BCC steels are now considered the most practical option for their low void swelling rates [29]. While other materials like high entropy alloys (HEA), oxide dispersion strengthened (ODS), and silicon carbide (SiC) have shown exceptional resistance to void swelling, ferritic/martensitic BCC steels are the most promising option for fusion applications due to optimizing other factors like weldability, manufacturability, and cost [44–46].

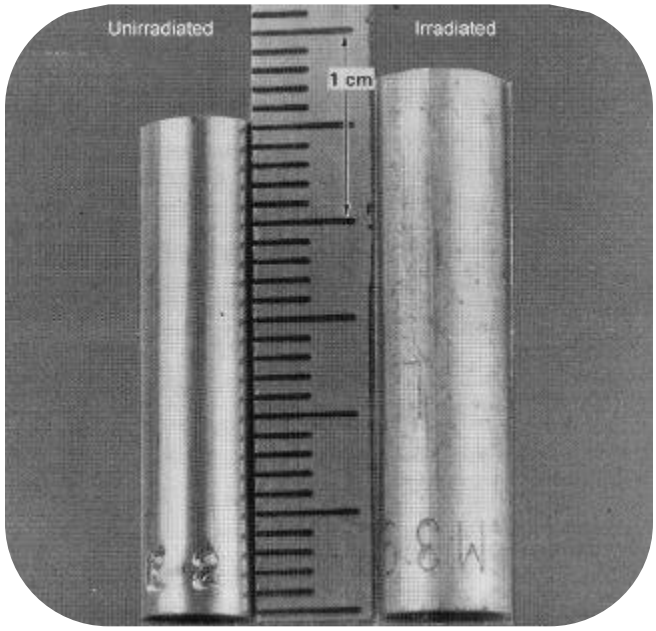

Figure 12. Radiation induced void swelling on 316 steel before and after neutron irradiation at the Argonne experimental breeeder reactor [47].

Hardening and embrittlement due to irradiation is one of the most concerning effects from dpa accumulation in irradiated materials. Figure 13 shows the expected irradiation hardening behavior of a BCC steel. Hardening from radiation is often accompanied by reduced ductility, as irradiation elevates the yield strength far more than the ultimate tensile strength (UTS). Once the yield strength surpasses the UTS, uniform elongation diminishes and at very high dpa, may eliminate necking and produce fully brittle fracture through a variety of mechanisms. The hardening arises from irradiation-generated microstructural defects, including defect clusters, impurity–defect complexes, dislocation loops and lines, voids, bubbles, and precipitates. These defects impede dislocation motion, thereby increasing resistance to plastic deformation through mechanisms like source hardening and friction hardening. The magnitude and kinetics of

hardening depend strongly on irradiation conditions like temperature and dpa as well as alloy composition and microstructure.

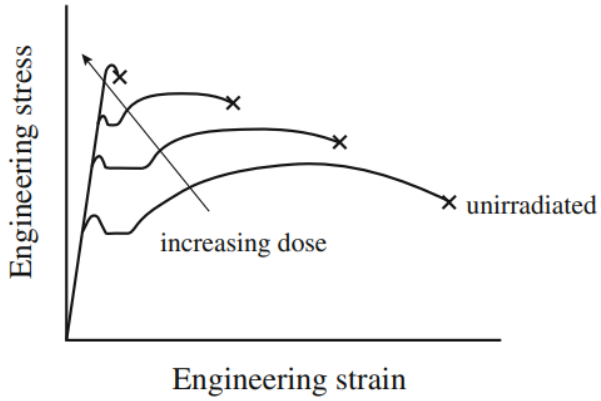

Figure 13. Expected irradiation effect on stress strain behavior for a typical bcc steel [35].

While void swelling and hardening are some of the most significant effects from radiation from a mechanical perspective, radiation damage also produces a very broad spectrum of microstructural and property changes in materials. At the fundamental level, the defects generated from the displacement cascades from a radiation event, cause a variety of effects as the material begins to reach an equilibrium state. One consequence is radiation-induced segregation (RIS), where point-defect fluxes interact with alloying elements to produce a diffusion gradient. Because vacancies and interstitials often have different mobilities with various solute species, irradiation drives solutes toward or away from defect sinks such as grain boundaries or free surfaces. This redistribution commonly affects stainless steels where elements like Ni or Si enrich at these interfaces while depleting Cr. This can degrade an alloys corrosion resistance and weaken local mechanical behavior. Radiation-induced amorphization can also occur, in which extreme displacement damage causes a loss of crystallinity primarily in materials with large negative heats of formation [35]. Irradiation creep happens when a material slowly strains under constant stresses during irradiation, even at temperatures where conventional thermal creep would be negligible. Here when a material is under tensile stress, dislocations act as defect sinks, absorbing interstitials and vacancies at different rates depending on their orientation, creating a net movement of the crystal lattice. Over long service lifetimes of a fusion reactor this mechanism can be influential for structural components where steady stresses combined with radiation can accumulate large dimensional changes [48,49]. Irradiation-assisted stress corrosion cracking (IASCC) occurs from the interaction between the irradiation modified microstructure through mechanisms like RIS which can enhance corrosion and mechanical degradation. This interaction between a crack tip formation in a material with radiation and corrosion can weaken a material's resistance to crack propagation. IASCC was originally studied and found to be a life-limiting factor for austenitic stainless steels in LWRs but is mitigated in fusion reactors through the use of ferritic steels [30]. Across all these phenomena examined so far, the non-equilibrium vacancy and interstitial population produced by purely from elastic and inelastic collisions with the lattice create a wide variety of irradiation phenomena. These vacancies and interstitials, when left to equilibrate and interact with other microstructural features like with solutes, sinks, chemical environments, and applied stresses, collectively cause complex material degradation behavior under radiation which need to be understood.

Aside from elastic and inelastic collisions, radiation which strikes a material lattice has a small chance to interact with the host atoms causing nuclear reactions. The probability of a specific nuclear reaction occurring is quantified by the nuclear cross section, which has units of barns, a unit of area equivalent to 10^{-24} cm^2. This cross section effectively represents the size of hitting the a nuclear target, causing a reaction. The size of these cross sections, and thus how easily a nuclear reaction occurs is highly dependent on the energy of the incident particle. For fission reactors, uranium has a higher cross section for lower energy thermal neutrons around 0.025 eV necessitating the need for neutron moderators to slow down neutrons. Resonances in the cross section occur at specific energies where the probability of interaction sharply increases due to matching of the neutron energy with quantized nuclear energy levels. With this, the rate of nuclear reactions in a material is then calculated using the flux of incoming radiation particles multiplied by the relevant cross section of the target and the number density of target, giving the nuclear reaction rate.

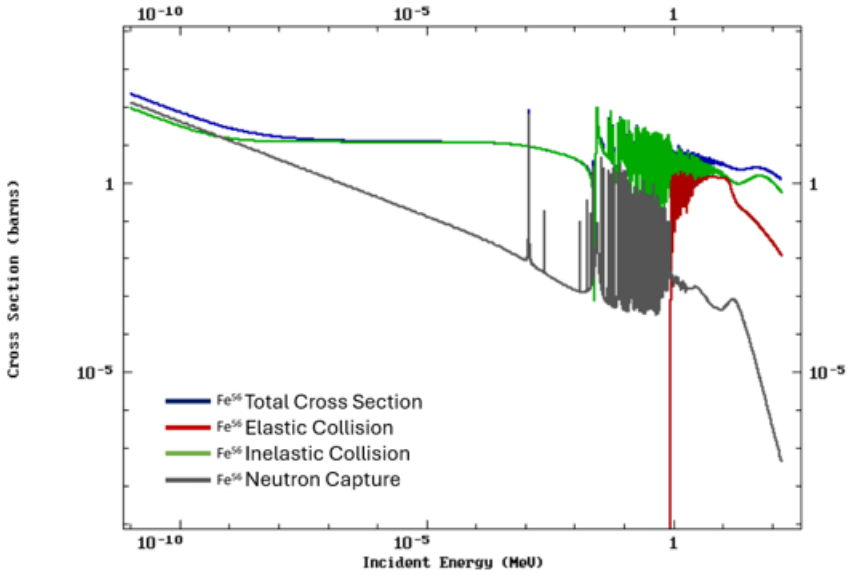

Figure 14. Cross section for various nuclear reactions of a neutron with Fe-56 from the ENDF database [50].

A large linear combination of reactions can occur in a fusion reactor with neutrons, escaped plasma ions like protons, D, T, and He, and gamma rays interacting with every element of structural and first wall material in fusion reactors, including tungsten, iron, nickel, chromium and many more. While many of these reactions are simply elastic or inelastic collisions which results in the aforementioned dpa accumulation, some result in nuclear reactions. While many nuclear reactions are possible, the one of particular concern in fusion reactors is neutron capture. When neutrons are captured, the host atom transmutes into an isotope of the same element with an additional neutron. In the case of Fe-56, this can absorb a neutron to transmute into Fe-57 and emit a gamma ray as shown in Figure 14. However there are certain elements which pose great transmutation threats due to dangerous levels of radioactivity emitted in the process or from undesired particle emission.

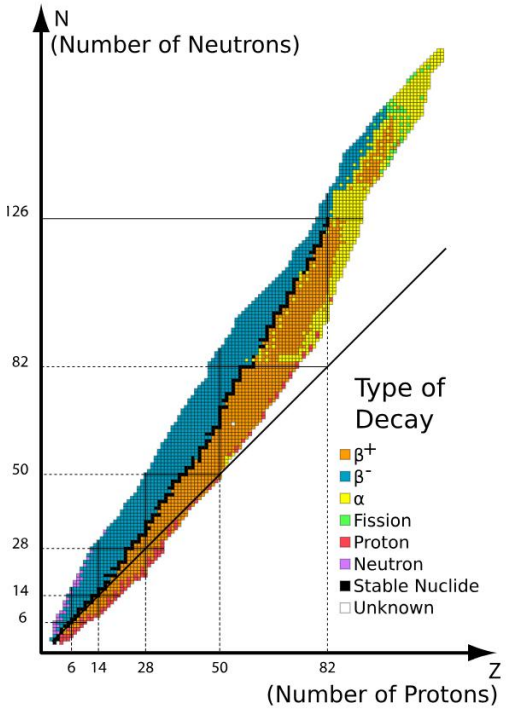

Figure 15. Band of stability graph showing every known isotope as a combination of proton and neutron as well as their preferred decay route [51].

Neutron capture resulting in gas production, like helium and hydrogen generation via (n,α) and (n,p) reactions are particularly dangerous as they have the potential to enhance void swelling. Elements like Fe, Be, and Cu have a particularly large cross section for these gas generating capture reactions at high neutron energies, limiting their use as a first wall material [52]. In addition to this, neutron capture resulting in transmutation to an unstable isotope causes a nuclear activation of irradiated materials. Here, the transmuted or activated isotope, which is typically unstable releases energy through radioactive decay. Decay mostly happens through three usual routes, alpha decay, beta decay, or gamma emission. Figure 15 shows a graph of every known isotope and their propensity for the different decay pathways. Due to the unstable nature of the isotope generated through nuclear activation, it will decay until it becomes a stable isotope, emitting harmful radiation in the process. This process sometimes initiating whole chains of subsequent decays until a finally a stable isotope is reached. Due to the seemingly random nature of nuclear decay, a nuclear half-life probabilistically explains the time it will take for half of the initial radioactive sample to have decayed. Due to the radiation emitted as a result of this nuclear activation process as the unstable isotopes decay to stable isotopes releasing radiation along the way, this contributes to the long-term radioactivity of irradiated materials and poses a radiological hazard. Commonly, this happens with Fe-58 and Co-59 in fission reactors which can absorb neutrons forming Co-60, an isotope with a long half-life and high energy radiation causing it to be a radiological hazard for decades.

1.3.3. Radiation Damage Mitigation in Materials

The mitigation or healing of radiation damage in materials is a fundamental area of study for nuclear materials. From all the previously covered radiation materials degradation mechanisms

identified, two disparate pathways for mitigation can be found. One focuses on the remedying the effects of the displacement cascades and subsequent dpa accumulation which result from the elastic and inelastic interactions. The other reduces the effects of nuclear transmutation on materials which arise from nuclear reactions.

Methods to mitigate the effects of dpa accumulation in materials are varied and relate to the diffusion of atoms within a lattice. It can be readily seen that all of the previously mentioned mechanisms for material degradation from radiation exposure like irradiation embrittlement, hardening, and void swelling are intrinsically tied to atomic diffusion processes. The displacement cascade from radiation damage is nonequilibrium process, introducing a supersaturated amount of vacancies and interstitials into the lattice. To reduce energy and depending on the material, the lattice will then form structures like dislocation loops, void, and stacking fault defects. In addition to this, the localized concentration of vacancies cause diffusion rates of solute atoms within the target lattice to change and move. Due to this intrinsic link of diffusion and radiation damage accumulation, factors like temperature which affect diffusion play an important role. Void swelling exhibits a strong temperature dependence, peaking at intermediate temperatures. At low temperatures, limited vacancy mobility suppresses swelling because vacancies are immobile and cannot diffuse to growing voids, halting their growth. At high temperatures, vacancy are very mobile, emitting from voids and offsetting vacancy influx, reducing swelling. Maximum swelling occurs at intermediate temperatures where vacancy thermal emission from voids is minimized and net vacancy flow to voids is largest. Figure 16b graphs the expected void swelling phenomena in 316 steel versus temperature.

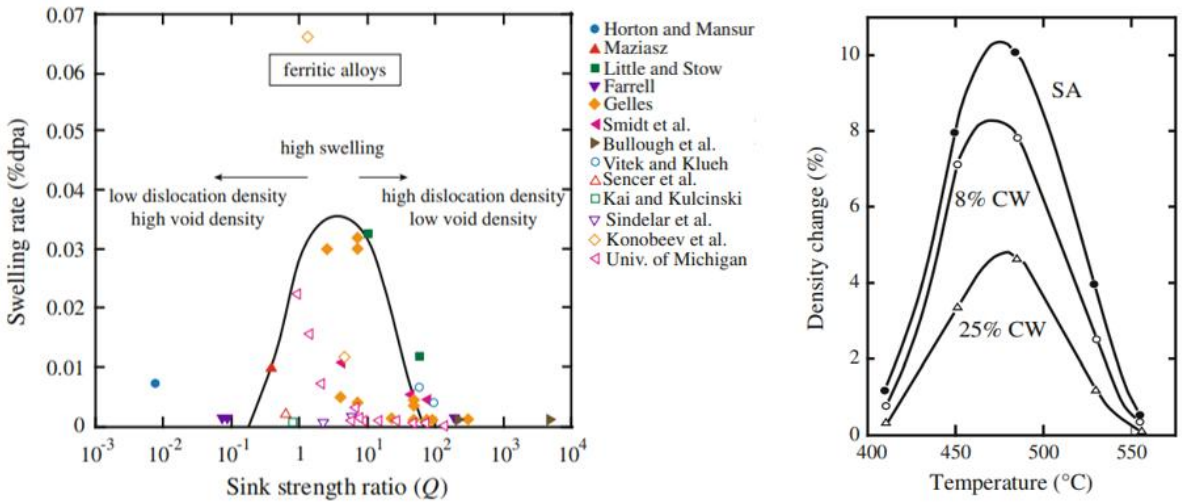

Figure 16. Void swelling rate versus sink strength ratio for ferritic alloys and density change versus irradiation temperature on 316 austenitic steel that has been cold worked (CW) [35].

Like swelling, the effects of radiation hardening and embrittlement are reduced due to temperature. At elevated temperatures, irradiation-induced defects become highly mobile and can recombine or annihilate at sinks such as dislocations, grain boundaries, and surfaces. This defect recovery reduces the long-term accumulation of defect clusters, dislocation loops, and also voids that would otherwise impede dislocation motion to cause hardening.

Along with temperature, the presence of sinks which provide an easy low energy pathway for irradiation defect diffusion provides another radiation damage mitigation method. Sinks like grain boundaries, free surfaces, incoherent precipitates, voids, and dislocations can absorb certain irradiation induced defects, effectively healing some dpa damage. The exact defect reaction ultimately decides the propensity of a certain defect for attracting irradiation defects. Sinks like dislocations and grain boundaries attract excess vacancies and interstitials, making materials with a fine grain structure or cold worked (which introduces a large amount of dislocations) excellent for reducing radiation damage effects. Figure 17 shows a graph of the temperature dependence of different deformation mechanisms for unirradiated and irradiated 316 steel. It can be readily seen that there is a large temperature dependence on the expected plasticity mechanisms, with high temperatures greatly mitigating the barrier for dislocation glide in irradiated materials.

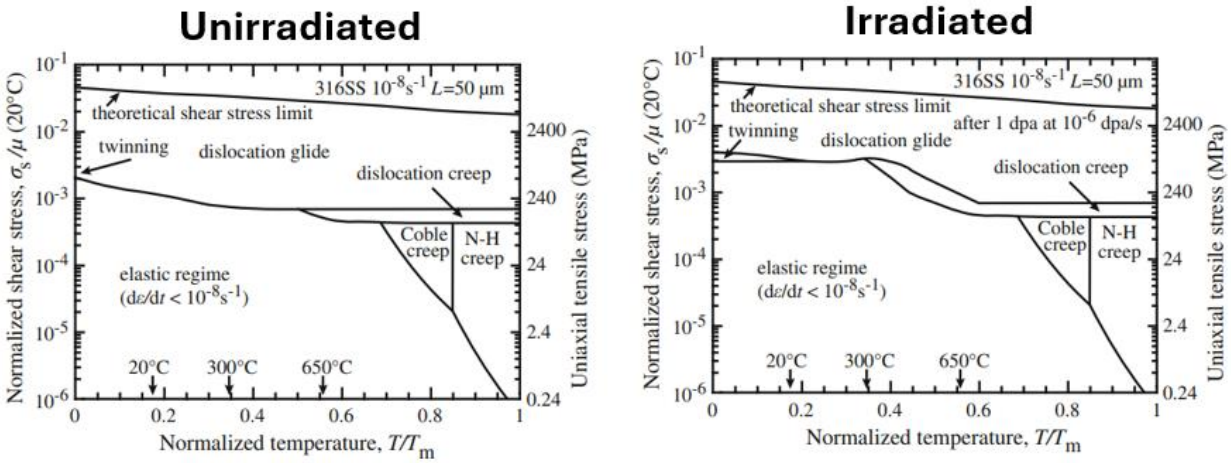

Figure 17. Temperature dependence of deformation mechanisms in irradiated and unirradiated 316 steel [35].

Methods to reduce the effects of nuclear transmutation resulting from nuclear reactions are fairly limited due to the heavily intrinsic nature of these interactions. The nuclear cross sections of the different nuclear reactions are inherent to the elements of the particle and target and cannot be modified. Therefore, the only realistic way to reduce the effects from nuclear transmutation within a fusion reactor is to modify the elemental composition of the material which radiation will interact with. This means that the elements of the materials chosen for the ITER blanket structure which will experience the highest radiation loads will need to be specifically tuned for reducing nuclear activation. Moschetti et al. provides a reference for different elements which are expected to heavily activate under fission and fusion reactor radiation spectrums shown in Figure 18 [53]. It can be readily seen that elements like Re, Mo, Nb, Ni, Co, and Ag have very long lasting radioactive emission following activation from exposure to a fusion reactor radiation spectrum. For this reason, traditional alloys which have proven to be successful in a nuclear fission environment like HT9, T91, and Inconel 600 which contain elements like Ni, Mo, and Nb are not suited for fusion reactors due to elevated nuclear activation concerns. As a result of this, new "reduced activation" classes of materials are being developed for fusion reactors which meet both the purity and compositional requirements demanded for reduced nuclear transmutation [29].

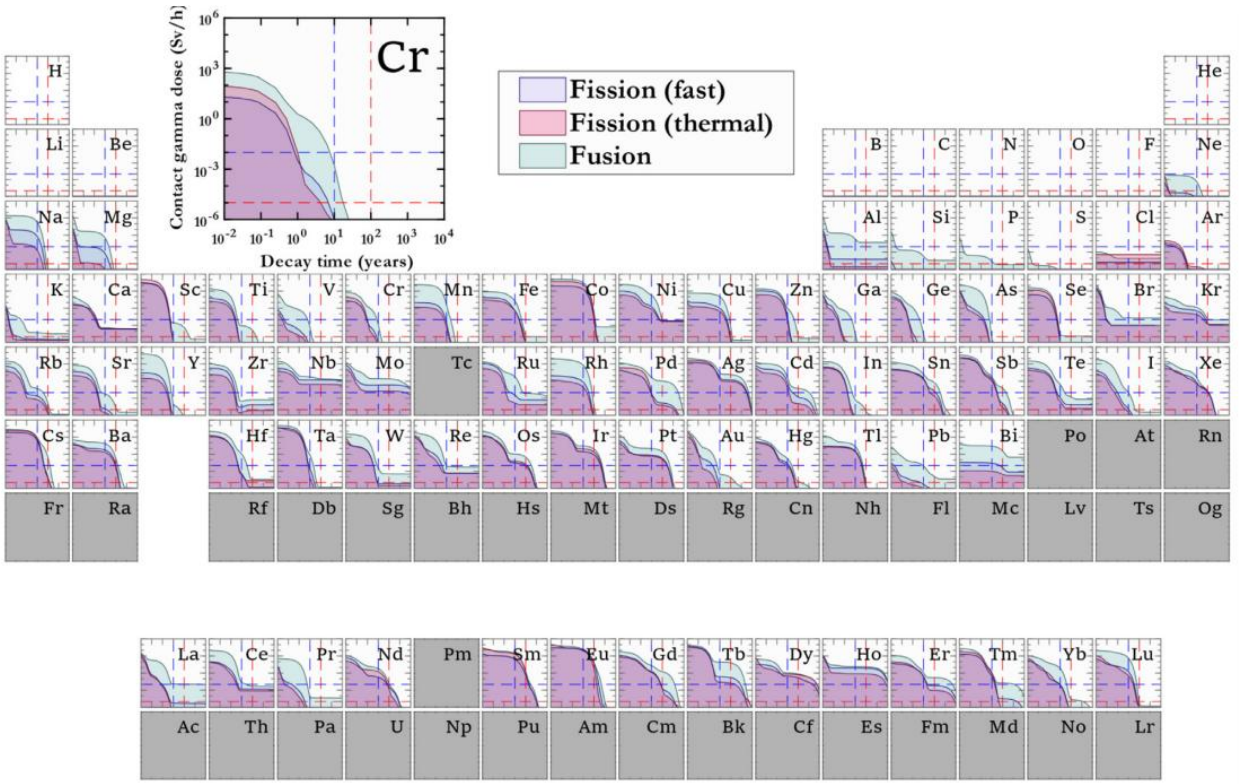

Figure 18. Nuclear activation of periodic table elements when subject to a theoretical 5 year irradiation under fission and fusion reactor neutron spectrums. The red and blue dashed lines indicate the remote recycling and "hands-on" limits, defined at 10 mSv h−1 after 10 years and 10 μSv h−1 after 100 years, respectively. [53].

1.3.4 The ITER Blanket Design

In addition to radiation damage producing a wide array of material degradation phenomena, fusion reactors will also be subject to many of the same challenges inherent to non-nuclear structures. A combination of dynamic and static stresses will be applied to the fusion reactor structure from a combination of gravity, pressure differences from the high vacuum, and magnetic forces from the superconducting magnets demanding exceptionally tough materials. Thermal effects created from the rapid heating and cooling of the plasma additionally will also modulate material properties of the structure. Corrosion effects within pipes carrying coolant to heat exchangers will also degrade structures. For this, an ideal structural material for the system will ideally be one which is thermally stable, corrosion resistant, mechanically strong, does not interact strongly with the magnetic field, resists radiation swelling/activation, and can be cheaply fabricated with current technologies [29].

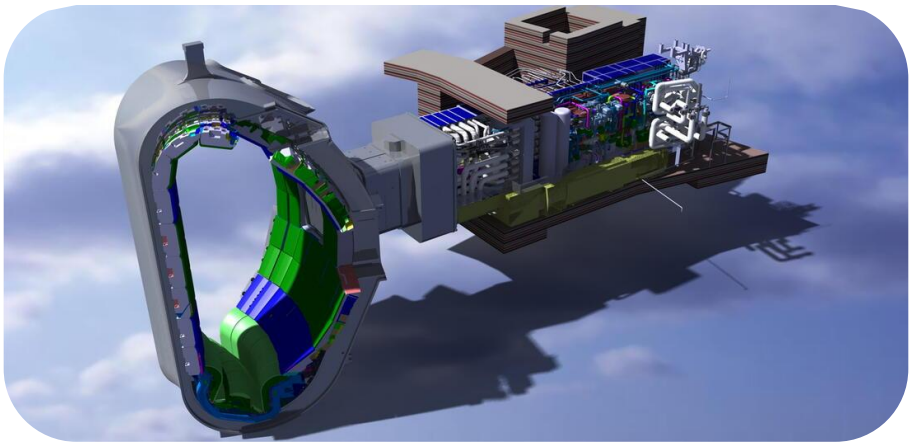

Figure 19. ITER test blanket module concept design showing one of eight modular blankets [54].

Coupled with all the aforementioned materials degradation phenomena in a fusion reactor plus their varying degrees of influence depending on the exact component creates a huge materials challenge for ITER. There are many parts and components for ITER serving different functions and collaborating countries have been assigned the task of researching and developing different materials systems for each component. The main component which poses the greatest scientific and engineering challenge is the blanket module which performs many functions [55]. The blanket module incorporates a breeding blanket whose primary purpose is to breed tritium (T) fuel within its structure. Tritium, due to its short half life, is not readily available naturally on Earth in the quantities needed to sustain a fusion reactor as a fuel source. For this reason, the breeding blanket has to create tritium within its walls from a neutron reaction with Li-6. The goal is that the neutrons generated from the fusion reactor operating, will react with Li-6 in the breeding blanket, producing more T fuel which can keep the fusion reactor operating forming a chained fuel cycle. The blanket also has to accommodate cooling channels to siphon the heat from the fusion reaction for power generation. It also has to hold a high vacuum with minimal leakage while withstanding the radiation environment and serve as the primary barrier from the fusion reactions to the outside. With all these functions, optimization of the blanket structure is one of the most important objectives of the ITER project. An example blanket design is shown in Figure 19. Many different designs have been proposed ranging from ones using helium as a coolant, water as a coolant, different alloys for the structure, different geometries of the structure, among many other designs [56]. Each design has varying degrees of benefits and downsides between each other, offering tradeoffs between thermal efficiency, breeding feasibility, corrosion mitigation, and radiation tolerance between many more factors. Due to the complexity and the lack of a clear option, ITER has tasked every collaborating country to develop their own experimental breeding blanket system using their own alloys and coolant designs [55]. These individual test bed modules (TBM) will be individually assessed for feasibility, where one will be chosen to be incorporated into the final ITER design.

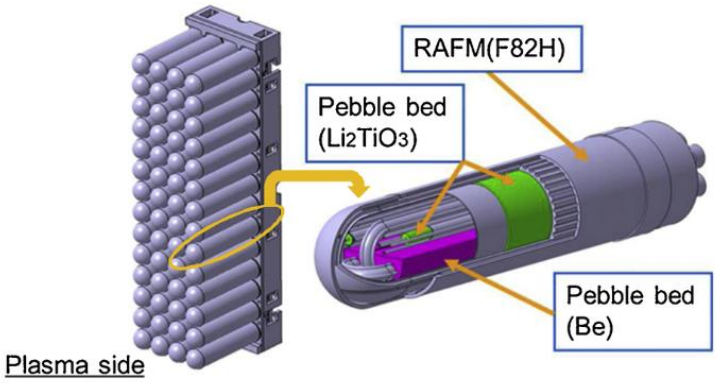

Figure 20. Conceptual design of Japan's test bed module (TBM) for their WCCB design [56,57].

Japan, a key collaborator in ITER, is currently developing a water-cooled ceramic breeder (WCCB) blanket design. Here, they will test the viability of using water coolant in the breeding blanket for heat transfer combined with ceramic LiO_2 pellets which will be used for breeding more tritium. Work is being done to progressively iterate and improve the different proposed TBMs. Following this, Japan's breeding blanket design is still a work in progress and every year their design changes as new simulations and tests are being done to validate its performance. As of 2020, the conceptual design for Japan's WCCB is shown in Figure 20 [56,57]. Since the early 1990's ITER has been in its "Basic Performance Phase". This phase has been described as making an initial stage build of the entire tokamak design without any tritium breeding or electrical generation as a proof of concept [58]. Due to the extreme difficulty of the tritium breeding process and the many unknowns of the process, this phase will aim to make a non-sustainable, cheaper version of the reactor to address the main question of feasibility [58].

1.4 F82H: The Japanese RAFM Steel

For a structural material in the ITER project, cost, weldability, easy machinability, radiation resistance, corrosion resistance, and structural stability lie at the core of concerns for candidate materials [29,59]. With these criteria, austenitic steels were first considered for this application due to meeting all the many of the core requirements while also lacking magnetic property. This was seen as an advantage in a fusion environment where high magnetic fields are used and would not strongly interact with an austenitic material. However, austenitic steels were found to heavily void swell at reactor relevant temperatures and above 20dpa, martensitic steels were considered [29,35]. Martensitic steels are magnetic, making designers initially concerned with local distortions produced by their ferromagnetic properties which could interfere with plasma stability. Also, it was thought that the superconducting magnets would produce large magneto-mechanical torque forces within a magnetic structural material causing high stresses potentially breaking the structure. However improved simulations began to support the idea that magnetic effects could be mitigated with careful magnetic control leading to martensitic steels being pursued [29]. However, concerns of nuclear activation were still present with martensitic steels. Traditional martensitic steels like HT9 or T91, already proven effective in nuclear fission reactors, had elements like Ni, Nb, and Mo which would heavily activate in a nuclear fusion environment. With the high neutron

flux of a fusion reactor interacting with elements whose isotopes are radioactive, a structural material could become extremely radioactive. Moschetti et al. tabulates the activation of all elements under a fission and fusion spectrum [53]. While this not a major issue in fission reactors where fission products dominate the radioactive spectrum, in fusion reactors where the only inherent activity comes from tritium, activation becomes more important [60]. Due to the nature of ITER being an experiment, lowering the residual radioactivity to levels so that active research can be done is imperative. In addition to this, early marketers of fusion energy wanted to distance the technology as far away from radioactivity concerns leading to reduced activation being a key concern. Martensitic steels also benefit from having a fine grain structure composed of martensitic laths. These laths have been proven in fission reactors to effectively provide sinks for radiation defects, mitigating irradiation hardening and void swelling by proving diffusion pathways for vacancies and interstitials [29]. Due to these factors, novel alloy development focusing on creating a martensitic steel with elements specifically tuned to reduce the activation of the steel manifested leading to the creation of a special class of steels for fusion reactors. Reduced activation ferritic/martensitic (RAFM) steels were created specifically for fusion applications and are the most mature option for structural materials for fusion reactors. The composition of RAFMs differ only slightly from that of other commonly used martensitic steels for nuclear applications like HT9 and T91. Many of the highly activatable elements like Mo, Ni, and Nb were replaced with elements like W, Ta, and V which do not activate as heavily but serve similar purposes for grain refinement and martensitic stabilization [61]. Multiple types of RAFMs are being considered for ITER and many countries have developed similar alloys for use in their prototype breeding blanket designs. The European team has developed the RAFM alloy EUROFER97, China has developed RAFM alloy China low activation martensite (CLAM), and Japan has developed the RAFM alloy F82H for their blanket concepts [62]. These RAFMs are currently envisioned to be the primary structural material forming much of the body of the blanket structure making it a key material within the project.

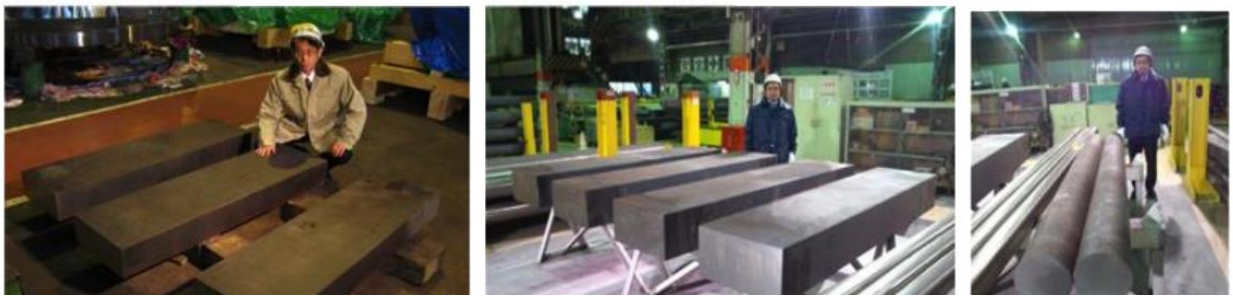

Figure 21. Billets and slabs of the first heat of production scale F82H made in 2007 [63].

Currently, F82H is the structural material of choice for the Japanese team's proposed WCCB design with a composition listed in Table 1. An SEM image of the microstructure of F82H is also shown in Figure 25. to show the complex ferritic/martensitic microstructure. Since F82H was developed in the 90s, research about the material has been steadily progressing. As of 2025, a total of 557 peer reviewed articles with "F82H" in the abstract, title, or keywords have been published according to Scopus. Due to its only application currently being in fusion reactors, this makes it a relatively niche material but one of the most mature in its class of RAFMs.

Fe	Cr	W	C	V	Mn	Ta
Bal.	8%	2%	0.1%	0.2%	0.1%	0.04%

Table 1. Nominal Composition of F82H

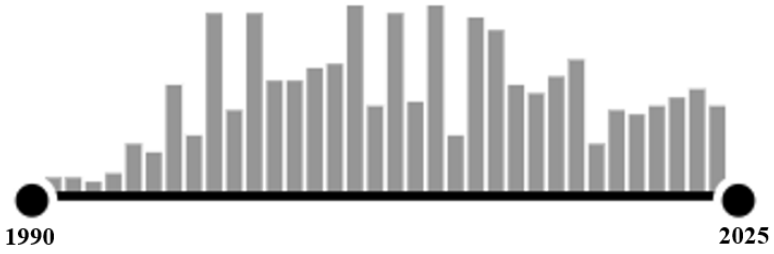

Figure 22. Time history of peer reviewed articles published on F82H since 1990 from Scopus

F82H was pursued for its balanced mechanical strength, phase stability, weldability, and superior irradiation resistance, particularly with minimal radiation-induced hardening and embrittlement. The current demonstration (DEMO) reactor which ITER is constructing would require more than 3500 tons of F82H to build much of the structure. For this a large-scale melting, refining, forging, and heat-treatment process was designed to achieve the low activation and consistent mechanical property standards for scaled production. The current process developed begins with blast-furnace iron, melted by Vacuum Induction Melting (VIM) and then Electro-Slag Remelting (ESR) to control impurities. The ESR ingots are hot-forged into slabs, then hot-rolled into plates of various thicknesses. After shaping, the material is normalized at ~1040ºC and tempered at ~750ºC. Initial studies show that air cooling after normalizing provides mechanical properties equivalent to water quenching, supporting scalable mass production. This full process from melt to ingot forms a tempered martensitic microstructure within the F82H whose microstructure will be explored in the following section.

1.5 The Tempered Martensitic Microstructure

Steel is by far the most investigated material in materials science. Due to its abundance, cheap price, and broad range of material property depending on different microstructural engineering steps, the study of steel metallurgy is extremely important. While many phases of steel exist and more than a century of study behind their each of their properties, the following discussion will be centered around martensite and ferrite, the predominant phases within F82H. Martensite is both one of the single phases and microstructures of the iron carbon system [64]. Figure 23a shows the phase diagram for a basic iron-carbon system which explains the different phases expected of a binary mix of Fe and C. However, at room temperature, martensite does not appear on the phase diagram due to the phase diagram representing only the thermodynamic equilibrium of the Fe-C system. Instead, a time temperature transformation (TTT) diagram is needed to explain the formation of martensite. Figure 23b shows the TTT diagram for mild steel and accounts for the kinetic part of phase transformation. Here it can be readily seen that a lattice

which is austenite at a high temperature, needs to be cooled to low temperatures within a quick enough time period to form martensite.

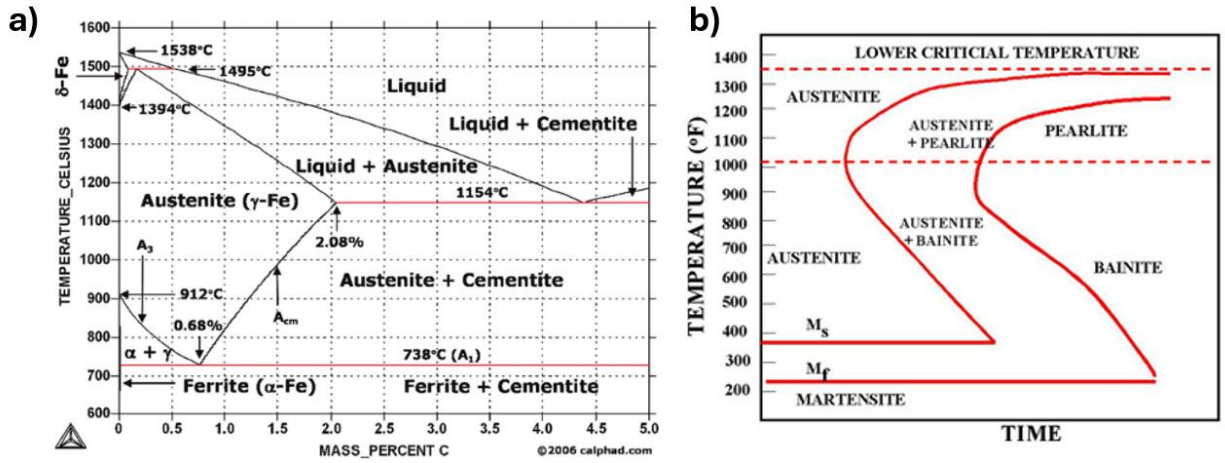

Figure 23. a) Phase diagram of the Fe-C system. b) Time temperature transformation diagram for mild steel [65,66].

As a result of this heating and quick cooling, martensite has an extremely fine grain structure due to the fast transformation kinetics. The original microstructure starts as an austenitic large grained structure at high temperatures. However, upon quenching, the austenitic grain interior forms a fine structure full of the sharp parallel features. This microstructure is typically divided into 4 defined groups of features: prior austenite grains (PAGs), packets, blocks, and laths. Prior austenite grains or PAGs are the grain boundaries forming the largest structure where the large austenite grain was before quenching. Packets are a substructure of a PAG which form large, divided sections of parallel sections of the martensitic structure. Blocks are even smaller sub-structures within the packet which form parallel oriented laths. Finally, laths are the smallest substructure which are the individual single orientation grains formed in the martensitic transition which are often only hundreds of nanometers in diameter. The orientation and formation of these structures is governed by the Kurdjumov-Sachs relationship which builds upon the Bain relationship explaining the orientation correlations for the FCC to BCC transformation [67]. Figure 24 gives a schematic illustration of these martensitic features.

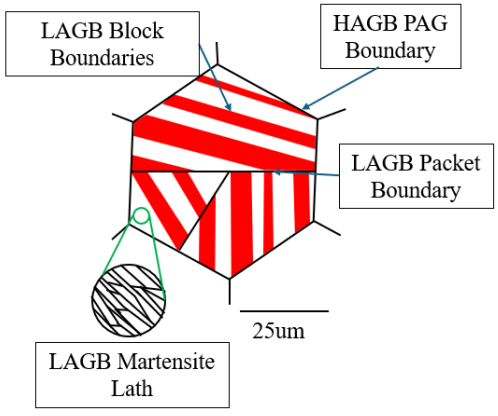

Figure 24. Schematic illustration of the martensite grain structure and substructures.

This martensitic microstructure is often desired and can be seen in many high performance applications like knives, turbine blades, springs, bearings, and automotive components. In fact, the reason why blades, knives and swords are forged and then subsequently quenched into oil is to induce this transformation due to the attractive material properties of martensite. This microstructure is often exceptionally strong due to a variety of metal strengthening mechanisms [68]. Its unique microstructure, which forms when austenite is rapidly quenched, prevents carbon from diffusing out. This results in a supersaturated body-centered tetragonal (BCT) phase where carbon atoms occupy interstitial sites, creating local strain within the lattice. These strains serve to hinder dislocation movement in a process called solid-solution strengthening. The tetragonal distortion of the lattice further impedes crystallographic slip by making the crystal structure asymmetric, increasing the critical resolved shear stress and making plasticity more difficult. In addition, the martensitic transformation introduces a very high dislocation density into the lattice which impedes further dislocation motion causing hardening. The fine grain structure of martensite formed from the lath, block, and plate grain substructures further inhibits dislocation movement and causes strengthening in accordance with the Hall–Petch relationship. Together all of these mechanisms including solid solution strengthening, lattice distortion, high dislocation density, and fine grain structure make martensite extremely hard and strong [64,68].

Martensite, which has just been rapidly cooled, called quenched martensite, is usually not desired, however. Quenched martensite is extremely brittle and shows little toughness which is not preferred for most applications. The strengthening mechanisms for martensite aforementioned trade off with ductility making brittle fracture more prevalent. When stress is applied to martensite, dislocation motion is severely impeded. As dislocations move from applied stress, dislocation pile occurs at interfaces and barriers. This dislocation pile-up creates an area for localized stress concentration. In ductile materials, this would initiate other plastic deformation mechanisms like slip, twinning, or phase transformation within adjacent grains, redistributing the stress and allowing for plasticity. However for martensite where dislocation motion is severely impeded this can lead to crack formation and propagation due to the limited plasticity routes possible [69]. These cracks often propagate through interfaces like grain boundaries or lath boundaries, severely reducing ductility.

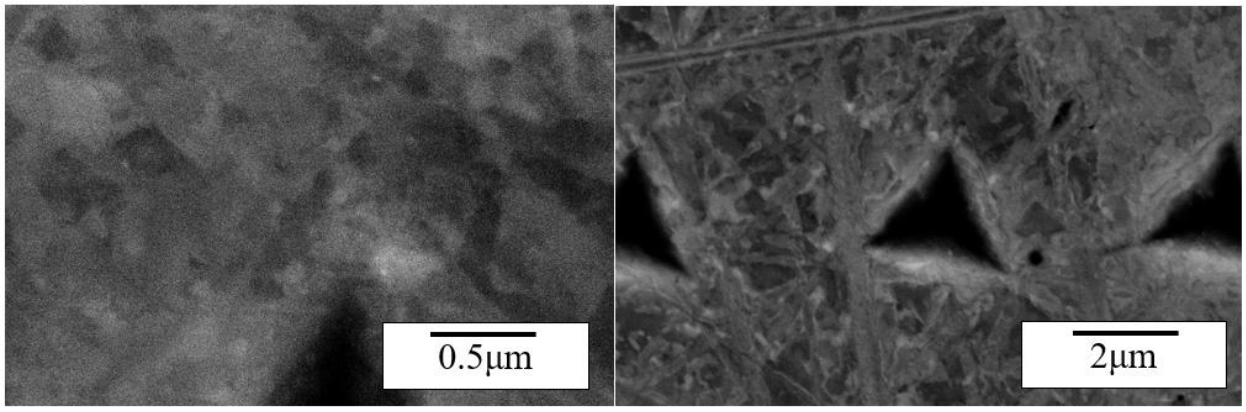

Figure 25. F82H microstructure showing complexity of grains imaged using ECCI from BSE/SEM electron imaging. Triangles are from nanoindentation hardness measurements

Tempering or heat treating is typically used in order to improve the ductility and toughness of quenched martensite. During the tempering step following quenching, there are multiple different mechanisms related to the increase in toughness of the alloy. In quenched martensite, there is a supersaturated amount of carbon which distorts the lattice into a BCT crystal structure, creating high residual stresses, lattice strains, and limiting the available slip systems. Tempering allows this carbon to diffuse to stable positions within the lattice resulting in an overall lattice relaxation effect where these high internal stresses are removed relaxing the crystal to a more symmetric BCC ferrite form [70]. BCC crystals with more available slip systems can accommodate plasticity more readily than BCT crystals leading to a more ductile behavior. Tempering also allows the extremely high dislocation density produced during the martensitic transformation to partially recover through dislocation rearrangement and annihilation, reducing stress concentrations and making dislocation pile-up less severe. At the same time, the lath, block, and plate boundaries in the martensite become more stable and less strained, removing weak, high-energy interfaces that can act as crack initiation sites. As the carbon atoms diffuse out of the BCT matrix, they form precipitates as fine carbides. During tempering the same hierarchical structure of laths, blocks, and plates which strengthen martensite are retained but with a now relaxed BCC ferrite crystal structure [64]. This process of quenching then subsequent heating produces the tempered martensite structure which is extremely useful and shows great ductility, toughness, and strength and is common in many engineering applications requiring resistance to extreme environments.

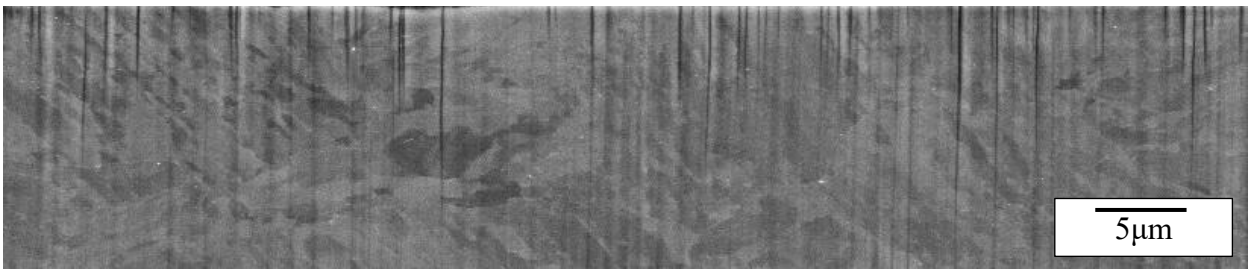

Figure 26. Backscattered electron image of the F82H microstructure showing fine lath martensite

One of the more influential effects of the tempering process is the formation of carbides as a result of the increased carbon diffusion during the heat treatment. Carbides are compounds which have the stoichiometry of M_XC_Y where X and Y are integers, M is one of the metal elements in the alloy, and C is carbon. The martensitic transformation traps carbon atoms in interstitial sites within the BCT iron lattice, generating significant lattice strain. This supersaturation creates a strong thermodynamic driving force for carbide precipitation upon heating and are formed through the diffusion of carbon atoms during the tempering of the alloy from their metastable positions in the as-quenched condition. This diffusion results in the carbon forming compounds with the alloying metals to typically form transition carbides (ε-$Fe_{2.4}C$), cementite (Fe_3C), and alloy carbides such as $M_{23}C_6$, M_6C, or MC with alloying elements like Cr, W, V, or Mo in F82H [71]. These carbides are an integral part in increasing the toughness, strength and fracture properties of the alloy .

Carbides rarely nucleate homogeneously within the martensitic matrix. Instead, they form preferentially at regions with high defect densities or structural discontinuities [71,72]. Primarily, incoherent interfaces like lath, block, and packet boundaries which form grain boundaries between martensite variants provide low-energy pathways for diffusion and as easy nucleation sites for

carbides. The preferential nucleation of carbides at these sites both accelerates precipitation but also strongly influences the resulting morphology leading to thin films, rods, or plate-like carbides aligned with crystallographic planes of the martensitic matrix.

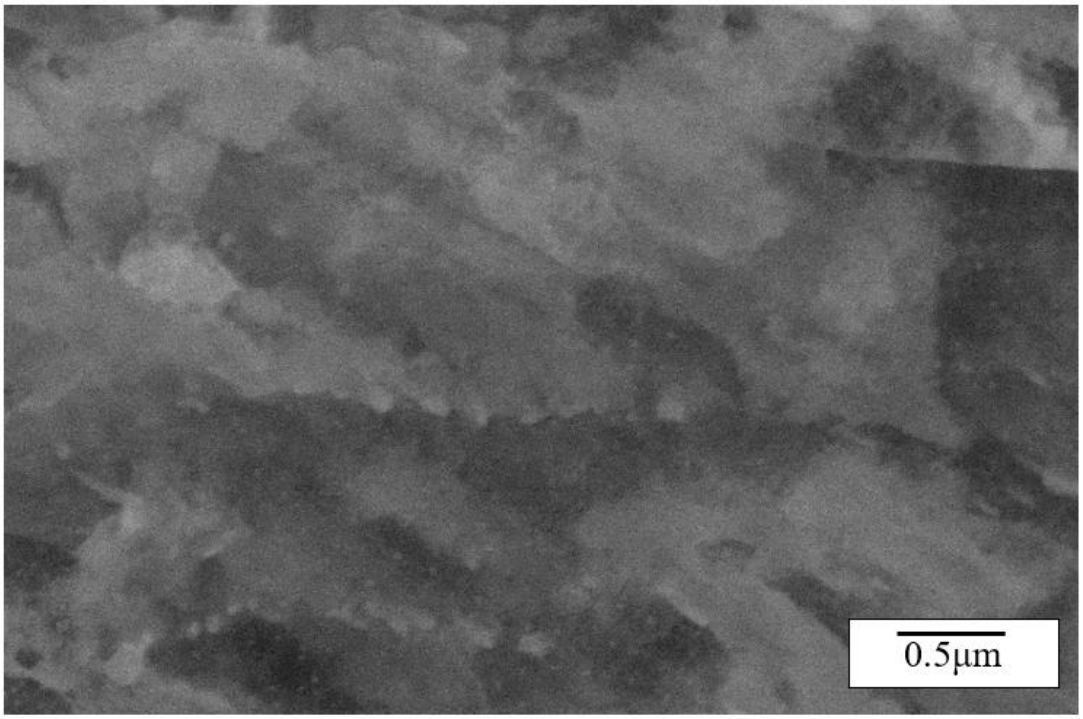

Figure 27. High resolution ECCI-BSE image of F82H showing carbides (brighter) decorating grain boundaries

The mechanisms of carbide strengthening are well known and involve a combination of precipitation hardening, martensitic structure stabilization through Zener pinning, and boundary hardening [72,73]. These mechanisms are all founded upon interactions with dislocations and boundaries with govern plasticity. The precipitation of carbides from metastable martensite directly governs the mechanical behavior of tempered steels. Precipitate hardening is maximized when fine, nucleated carbides provides barriers to dislocation motion but over coarsening and evolution of cementite, decreases precipitate density as they aggregate, leading to a reduction in hardness and strength. Finely distributed carbides act as strong obstacles to dislocation motion, forcing dislocations to bow past them through the Orowan strengthening mechanism [64]. Martensitic structure stabilization happens due to the fine carbide structure which pins grain boundaries. While metals tend to coarsen at elevated temperatures, having carbides nucleated at grain boundaries, pins these boundaries, preventing large grains from forming, enhancing high temperature strength through the Zener pinning mechanism. Finally, boundary hardening occurs when carbides nucleated at grain boundaries serve as barriers for slip transfer between grains enhancing plasticity [74]. These mechanisms serve to toughen the ferritic/martensitic matrix in tempered martensite and are ultimately desired for fusion applications.

Chapter 2

Thesis Aims and Objectives

2.1 Thesis Impact Statement

As fusion energy is being developed, a fundamental mechanistic understanding of how materials will behave when exposed to the intense reactor environment is imperative. F82H is one of the most mature candidate materials for the structural vessel of the pioneering ITER experiment. The alloy is a tempered martensitic steel developed to withstand the fusion reactor environment however much is still not known about it. Particularly, the mechanical effects of carbide nucleation in the steel has not been deeply studied across the microstructure. To investigate this, quenched and tempered F82H needs to be mechanically investigated using small scale mechanical testing to probe individual boundaries. Small scale mechanical testing probes micron-scale volumes of material in order to understand specific material defect interactions. Using such resolved techniques will allow for conclusions to be formed about carbide precipitation and the effects on mechanical properties within different microstructural features of F82H. The conclusions from this study serve to inform future research on fundamental carbide strengthening mechanisms within martensite while also giving an outlook into the degradation of mechanical properties of quenched martensite which can form in fusion reactors.

2.2 Dissertation Structure

This dissertation aims at studying the effect of carbides on the mechanical performance of the RAFM steel, F82H. To this end, small scale mechanical testing was used to probe specific martensitic interfaces. In the process, a technique was developed to rapidly make damage free small scale mechanical testing samples and the possibility of extrapolating this data to large-scale structures was discussed.

- Chapter 1 provides an introduction on the history of fission and fusion based nuclear power, basic metallurgy, and aspects of how F82H steel was developed to withstand the intense nuclear fusion reactor environment.
- Chapter 2 gives a concise summary of the dissertation goal, hypothesis, and structure,
- Chapter 3 outlines the methods and theory behind each of the testing techniques used to investigate the thesis hypothesis.
- Chapter 4 showcases a study which develops a high throughput technique for the small scale mechanical study of F82H.
- Chapter 5 explores the possibility of extending small scale mechanical results to the bulk scale and the important considerations needed to extrapolate results.
- Chapter 6 identifies the effects of carbides on the energy dissipation mechanisms across martensitic interfaces using small scale mechanical testing
- Chapter 7 quantifies the effects of carbides on the uniaxial tension behavior across martensitic interfaces using small scale mechanical testing.

Chapter 3

Methods

3.1 Experimental Methods

3.1.1 Mechanical Testing

Mechanical testing is an integral part of understanding how materials respond to external forces, and it encompasses a wide array of experimental techniques designed to probe different aspects of deformation and failure under loading conditions. These studies help connect material microstructure and macroscopic performance, serving to inform macroscale conclusions of in-service parts for safer design. In many of these tests, a load sensor is used in parallel with an extensometer to probe the material response as it is being compressed, bent, twisted, or pulled apart. The shape, magnitude, and features of the load-displacement curve recorded can give valuable insights on how a material will behave in real-world loading situations with properties such as strength, toughness, and ductility. It is common in most cases to convert load–displacement data to stress–strain data so that mechanical behavior becomes independent of specimen geometry and size, allowing direct comparison between material and sample. Stress and strain normalize the applied load and deformation to the test sample's cross-sectional area and original length, respectively. In this dissertation, three primary mechanical testing methods across two length scales were used to probe the mechanical effects of carbides in F82H.

3.1.1.1 Meso-Mechanical Testing

Meso-mechanical testing is a niche technique used to measure mechanical properties on the meso-scale. While micro-scale and bulk-scale mechanical testing are fairly well practiced, testing on the meso-scale occupies a space between these two length scales. The American Society for Testing and Materials (ASTM) releases guides for best practices in the mechanical testing of materials. However, these standards do not extend to the meso-scale or micro-scale due to size effects in material testing. Hosemann et al. describes how strength varies with length scale which ultimately concludes with higher strength values for smaller length scales [75]. Due to the difference in defects sampled, microscale tests are expected to appear stronger due to the lack of defects which can weaken the material. Bulk scale tests on the other hand, which test sample a large variety of material defects are expected to be mechanically weaker. However, depending on the material property tested, the change as a function of length scale is greatly dependent and the mechanisms of such remain an active area of study in materials science. Despite these size effects, meso-scale and micro-scale mechanical testing remain the only option for nuclear materials whose radioactivity limits sample volumes. A framework for extrapolation of results across length scales is imperative for correlation of meso-scale and micro-scale tests to bulk-scale commercial parts.

A high throughput method for meso-mechanical tensile testing was developed and iteratively improved upon in this dissertation to measure accurate stress-strain data. Due to the niche that meso-mechanical testing occupies, no commercial system specializes in this type of testing, requiring design and modification of existing systems. A Kammrath-Weiss (KW) Compression and Tension Module at UC Berkeley which uses a load frame to accurately test bulk scale mechanical test specimen was modified to test on the mesoscale. Furthermore, a custom movement stage was designed and machined to accommodate sequential accurate positioning of adjacent tensile bars. In this technique a femtosecond laser system was used as a machining tool to fabricate tensile bars and a custom fit shoulder gripper on this length scale. The modified KW tester, equipped with a 50N load cell and built in extensometer was used to accurately discern load-displacement data. This testing setup is pictured in both Figure 28 and Figure 30. The procedure developed in this dissertation to test femtosecond laser machined mesoscale tensile bars had 6 main steps:

1. A thin foil piece of a sample ~100μm in thickness is prepared through wafering and polishing steps
2. The thin foil piece is loaded into a fs-laser system and the outline of the tensile bar geometry is ablated from the foil, fabricating tensile bars.
3. The laser cut tensile bars are clamped firmly into the custom movement stage on the KW tensile tester.
4. The tensile bars are adjusted and accurately positioned within shoulder grippers connected directly to the load cell.
5. Force is applied to the tensile bars while connected to an extensometer to read the displacement data simultaneously with the load cell data.
6. Following testing, the axes of the custom movement stage are moved to insert the next tensile bar into the shoulder grippers to repeat testing on next sample.

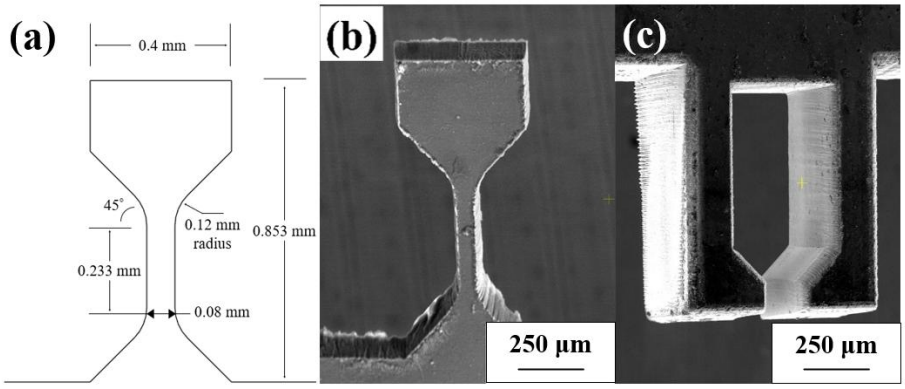

Figure 28. a) Dimensioned drawing of meso-scale tensile bar. b) fs-lasered mesoscale tensile bar. c) fs-lasered shoulder gripper for testing

This technique has been practiced recently with some success. Dong et al. used a femtosecond laser system to machine tensile bars of various dimension to detail its potential [76]. Harvey et al. also used the FemtoScribe system at LANL to rapidly machine tensile tests on AM

T91 and austenitic steels [77]. Choi et al. also produced cantilevers out of Cu to characterize elastic modulus [78]. However, questions on heat affected zone generation, test standardization, laser parameter optimization, and size effects still limit its widespread usage.

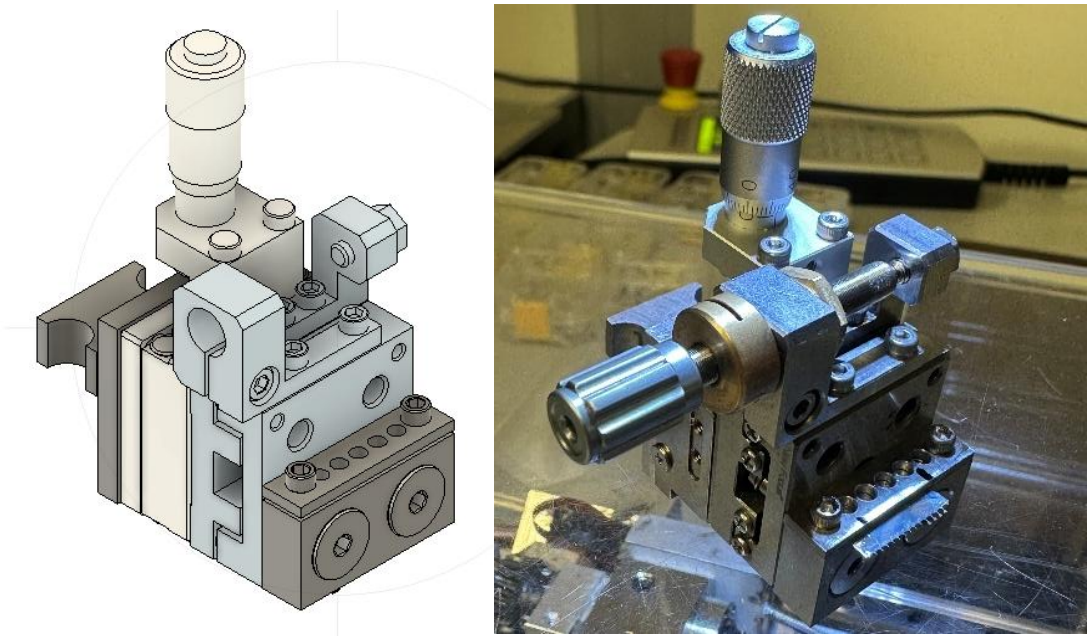

Figure 29. (left) 3D rendering of KW tensile bar gripper stage. (right) machined KW tensile bar gripper stage

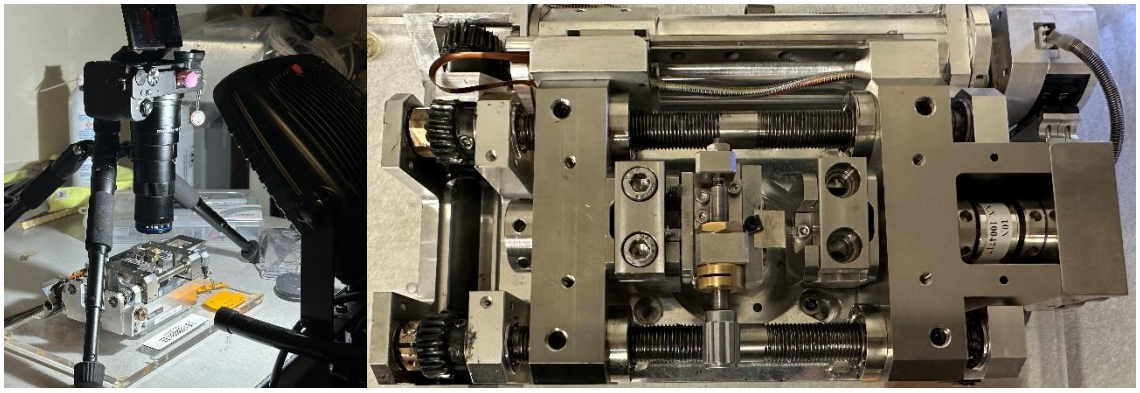

Figure 30. Meso-mechanical testing setup. (left) DIC lighting and camera setup during mechanical testing. (right) Close-up image of mechanical testing setup.

As with many mechanical testing setups, machine compliance influences testing results heavily. Stress-strain data is desired from these experiments, and it is straightforward to calculate this from the raw load-displacement data through adjustments from the measured gauge dimensions. However, the raw displacement data often accounts for more than the desired extension due to the material deformation. The measured displacement which is measured from the machine is a combination of multiple screw mechanisms coupling together, gripper deformation, load frame movement, and material deformation. In order to accurately remove all other effects other than material deformation, digital image correlation (DIC) was used assist in

data analysis. DIC is an optical imaging combined with software analysis technique used to measure full-field surface displacements and strains on materials under mechanical or thermal loading. It has become one of the most powerful tools in mechanics because it can provide detailed spatial information about deformation more resolved than traditional point-based methods like strain gauges or extensometers. DIC is based on optical pattern matching between images of a specimen's surface taken during deformation. The surface is typically prepared with a random speckle pattern created by spraying paint or applying a colloidal particle solution to the surface. This pattern provides a contrast variations that specialized software can track and correlate the deformation distances. The DIC process developed involved using a Nikon camera equipped with a high magnification lens, to accurately image the tensile bar as it deforms. The Zeiss GOM Correlate software was then used to analyze the images of the tensile bar deformation to record more accurate deformation data. Snapshots during the DIC correlation process displayed on a nickel test sample are shown in Figure 31. A calibration curve was made using this DIC process which then applied to all subsequent testing. Validation of this method was done by correlating the measured elastic modulus of the tests with literature values.

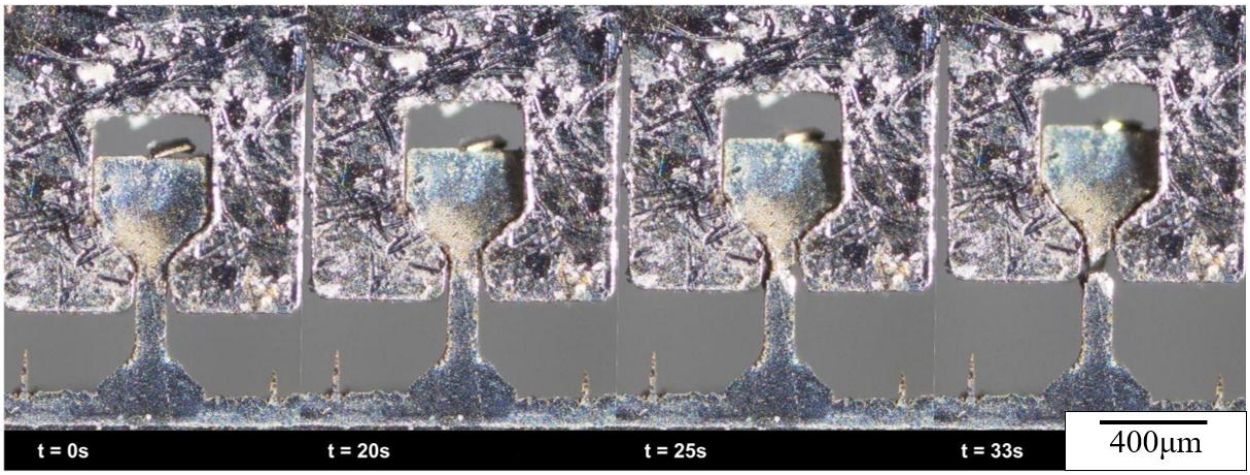

Figure 31. Snapshots of the DIC process as displayed on electroplated nickel tensile tests [79].

3.1.1.2 Small Scale Mechanical Testing

Small scale mechanical testing (SSMT) is a popular technique used to probe the mechanical properties of small volumes of materials. Typically micron-scale structures are fabricated and tested using precise load reading devices to probe the material response at this small length scale. For most applications and industries, SSMT is not usually needed for obtaining useful mechanical data. Data gained on samples with such small, confined volumes often do not give properties representative to the bulk scale due to length scale effects making data extrapolation difficult for those interested in engineering scale mechanical response. However, this technique offers a couple of advantages when compared to bulk scale testing methods. When testing on such limited volumes of samples, individual defect interactions can be isolated and investigated in isolation, giving valuable insights into fundamental material behavior. Also, SSMT is useful for samples which are difficult to test on larger scales like radioactive or toxic materials. The study of materials relevant to the nuclear industry in particular benefits from this, as SSMT allows for the mechanical investigation of materials which might be too radioactive to handle in large volumes. Also,

materials like micron-scale thin films or coatings which cannot be tested in conventional bulk scale tests benefit greatly from SSMT where it becomes the only way to probe mechanical properties. Hosemann et al. further highlights the importance of SSMT and showcases a variety of techniques relevant to the nuclear field [75]. A Hysitron PI-88 picoindenter system used for SSMT is pictured in Figure 32.

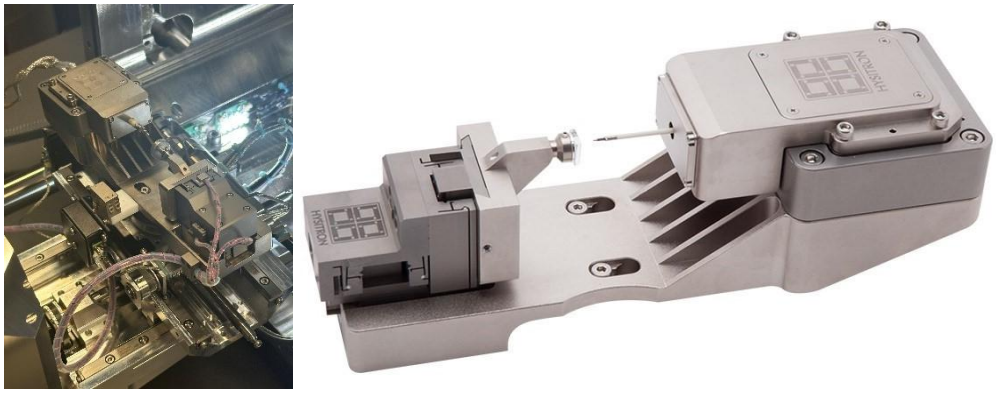

Figure 32. Hysitron PI-88 picoindenter system loaded with sample in-situ in an SEM

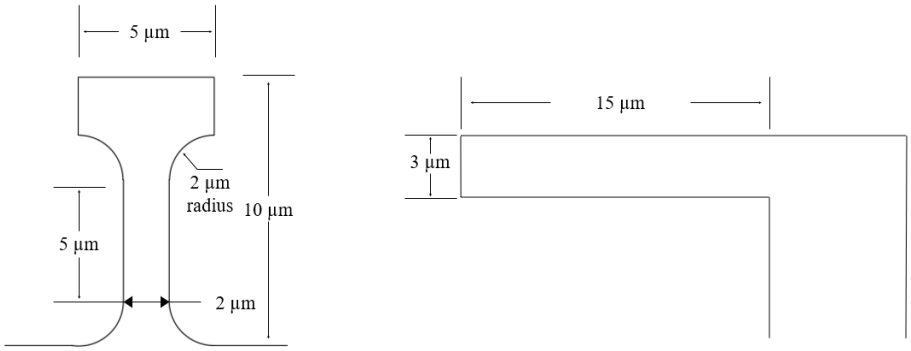

Figure 33. Scaled dimentioned drawings of microtensile bar and microcantilever for SSMT

SSMT encapsulates many techniques including but not limited to nanoindentation, microcompression, microtensile, and microbending experiments, all of which are enabled by highly accurate picoindenter systems. Common dimensions showing the length scales of microtensile and microcantilever tests are depicted in Figure 33. For this dissertation two SSMT experiments are used: Micromechanical spectroscopy and microtensile testing. The use of these techniques enables the detailed study of carbide behavior at interfaces in F82H.

While SSMT can reveal the important mechanical behavior of individual defect interactions and the behavior of confined volumes of material, it suffers from a couple of drawbacks making it not fit for many applications.

- Length scaling effects heavily affect the mechanical properties measured for microtensile bars. A "smaller is stronger" effect is usually seen with many small scale samples exhibiting a much higher measured strength than measured on the bulk scale making extrapolations to the bulk scale hard.

- Specimen fabrication and testing is usually lengthy and costly, requiring specialized tools like a FIB or lithography methods. As a result, studies usually on focus on small quantities of tests, limiting statistics.
- Artifacts present in SSMT samples have a magnified effect on a small length scale, making it more difficult to interpret data. FIB milling damage, small changes in surface roughness, and surface effects like oxidation, while negligible in larger scale tests become important to control on a small scale.

For most commercial applications and engineering questions, bulk scale testing is still the best option. However, for science inquiries trying to uncover the fundamental mechanisms of defect interactions and for industries with material volume restrictions, SSMT remains a foundational technique. For example, Kiener et al. directly observed dislocation interaction with irradiation defects in Cu using SSMT [80]. Vo et al. was able to investigate irradiation effects in austenitic steels and shifts in deformation mechanisms due to radiation using SSMT micropillars [81]. Liu et al. discovered mechanisms for high fracture toughness in high entropy alloys using SSMT [82].

Micromechanical Spectroscopy (μMS)

Micromechanical spectroscopy (μMS) is a SSMT technique developed at the Montanuniversität Leoben by Alfreider et al [83,84]. The technique probes resonance peak changes on focused ion beam (FIB) fabricated microscale cantilevers. A key advantage to this technique is that it nondestructively gives quantitative values for damping which can be correlated to sources for internal friction. Due to the scale and the nondestructive nature of this testing, the same cantilever can be tested before and after heat treatments to see how damping and internal friction evolves within cantilevers encompassing different microstructural features.

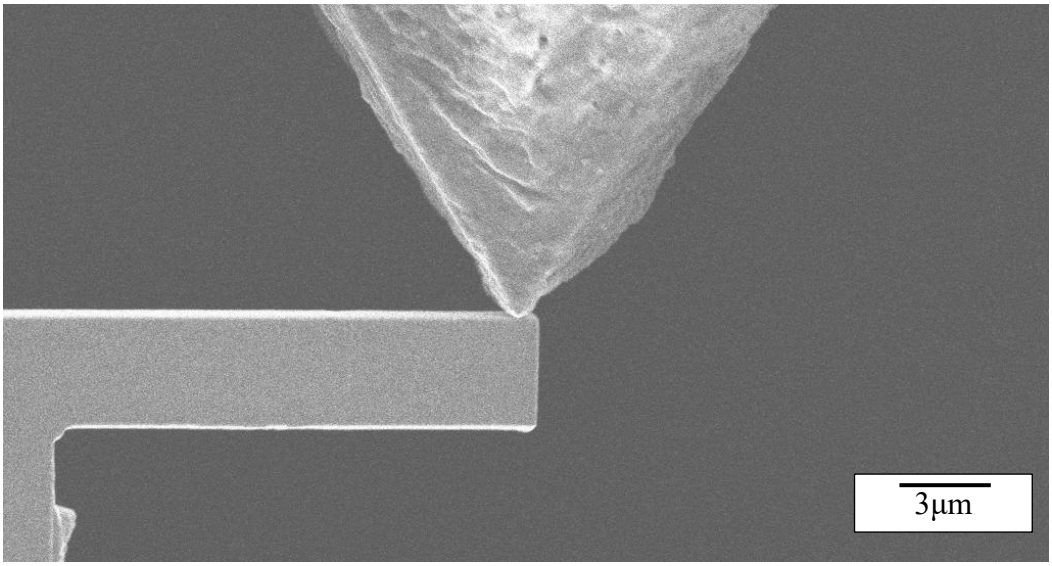

Figure 34. SEM image of microcantilever being loaded during μMS experiment

Internal friction and damping measurements were popular topics championed in the 1960s and 70s by scientists like Snoek, Granato, Lücke, Kê, and Köster who found interesting frequency and temperature dependent amplitude peaks in the torsion of metal wires [85–88]. As mechanical energy is transferred to a material, energy not transferred into plasticity has to be dissipated through other means. It was seen through twisting metal wires that the oscillation amplitude and frequency of the twisting motion was material dependent. Furthermore, upon cold working, heat treating, charging, or using different fabrication methods, the oscillation changed even further, forming the first studies on internal friction in materials. After much study, these peaks could be correlated directly to the movement of specific defects in the material by correlating the energy dissipated to the activation energies of the defect movement [88]. In the absence of advanced microscopy and other spectroscopy techniques, this was one of the few ways to gain an intricate view into the interactions of dislocations and interstitials with a relatively simple experimental setup. While research in the area has steadily declined with more resolved characterization methods, internal friction still remains a foundational niche in studying defects. Internal friction now is used to estimate fatigue material fatigue as dislocations are formed and also estimate interstitial content [85,89].

For μMS, a microcantilever is placed into a picoindenter system with dynamic measurement capabilities and brought into contact with the indenter tip. Following contact, a frequency scan is used to probe the resonance peak whose shape and magnitude can be used to estimate damping and elastic properties. The mathematical framework of μMS is explored further in the seminal work by Alfreider et al. In summary, the μMS experiments measure the dynamic compliance of the indenter tip as a function of the frequency. It is easier to think of this as the displacement of the cantilever tip as a function of the frequency being applied. The experimental system can then be simplified to a single degree of freedom (SDOF) oscillator model. The SDOF model is composed of stiffness contributions from the measured stiffness, b, frequency and resonance frequency, ω and ω_o, and the mass of the indenter tip, m.

$$c_{dyn} = \frac{1}{\sqrt{m^2(\omega_0^2 - \omega^2)^2 + (b_{tot}\omega)^2}}; \quad \omega_o = \sqrt{\frac{k_{tot}}{m}}$$

In this model, the total damping, b_{tot}, and stiffness, k_{tot}, can be extracted from the compliance, c_{dyn}, and frequency, ω, data. The raw frequency-compliance data can then be fit to a physical model equation to determine the best estimated values for damping and stiffness. These extracted values can be then used to calculate Q^{-1}. Additionally basic Euler-Bernoulli theory of a simple loaded beam can be used to estimate the elastic modulus, E, of each cantilever using the length, L, and moment of inertia, I.

$$k_s = \left(\frac{1}{k_{tot} - k_i} - \frac{1}{k_c}\right); \quad Q^{-1} = \frac{b_{tot}}{\sqrt{k_{tot}m}}; \quad \omega_o = \sqrt{\frac{k_{tot}}{m}}; \quad E = \frac{k_s L^3}{3I}$$

These equations derived from basic SDOF oscillator models form the basis for μMS and have previously produced incredibly resolved data which revealed specific defect interactions. Alfreider et al. found that this method was able to investigate defect recovery in fine grained Ta using this method [84]. In this dissertation μMS was used to probe defect interactions of carbides

with dislocations within F82H martensite. The Hysitron PI-88 in situ picoindenter system at UC Berkeley was used for all the measurements with a 1μm radius diamond wedge tip.

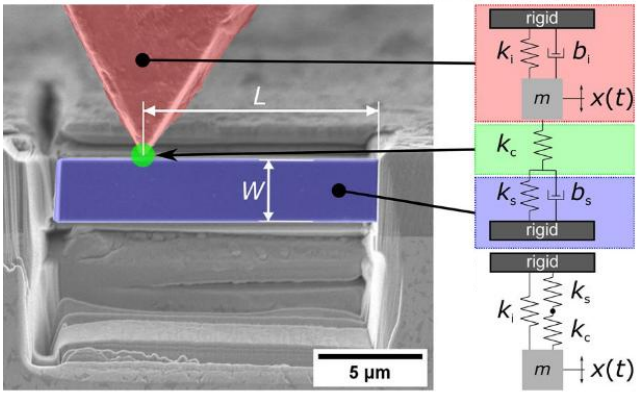

Figure 35. Single degree of freedom oscillator model showing model components adapted from Alfreider et al [83,84].

Microtensile Testing

Microtensile testing is the second SSMT technique used in this dissertation. This testing performs a uniaxial tensile test on micro-scale tensile bars while recording accurate load-displacement data from the same picoindenter system used for μMS. Using resolved measurements for the gauge dimensions, this raw load-displacement data can be correlated to stress-strain curves. The strain rate used for microtensile testing was set at 10^{-3}/s. Due to the micro-scale of these tensile bars, the mechanical behavior of individual grains or grain boundaries can be tested. Important values like critical resolved shear stress, ultimate tensile strength, yield strength, elastic modulus, and strain to failure can be obtained from this method making it a powerful technique in measuring mechanical properties. For this reason, there is no ASTM standard methodology for performing SSMT with microtensile bars. In addition to this, due to the limited defects present and material anisotropy, scatter in the data is usually very high, giving statistically inconsistent results. However careful analysis of the individual tensile curves helps to reveal fundamental trends in deformation which can be applied to bulk scale mechanisms.

In this dissertation, microtensile testing was used to probe the effect of carbides at interfaces in F82H martensite. A Hysitron PI-88 picoindenter system was used for this testing equipped with a custom machined diamond shoulder gripper. Microtensile testing has been gaining popularity from a wide variety of fields who demand the small volumetric constraints of the micro scale. Goracci et al. measures the microtensile strength of tooth root canals to inform dental practice [90]. Frazer et al. further tests hot isostatic pressed aluminum to probe bond line failure using microtensile testing [91].

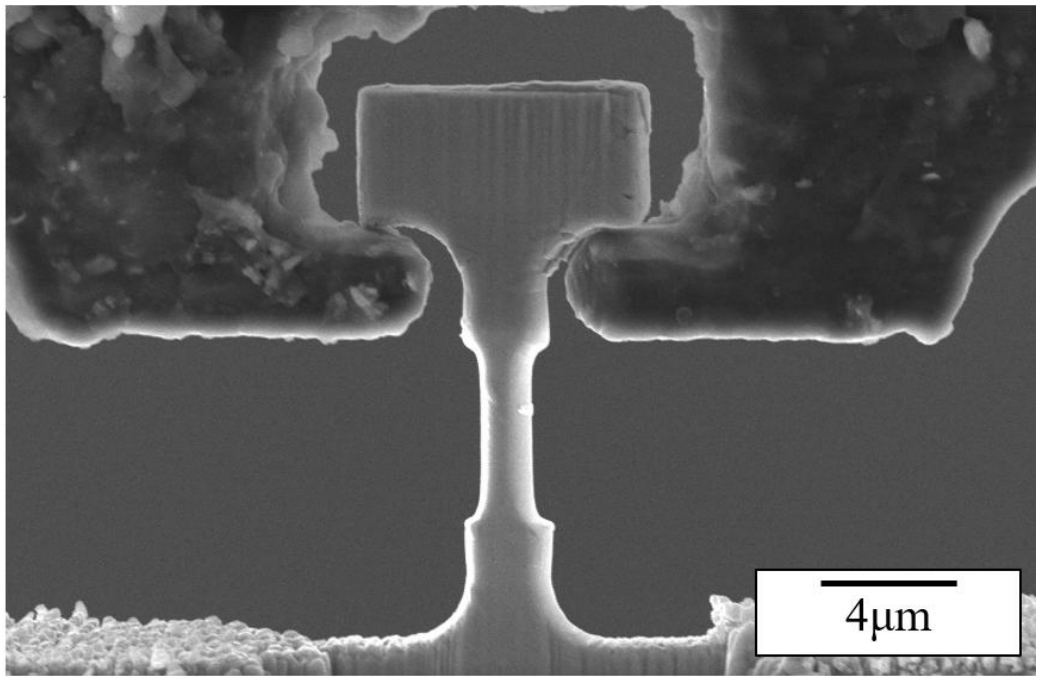

Figure 36. SEM image of microtensile bar fabricated using FIB during microtensile experiment.

3.1.3 Electron Backscatter Diffraction

Electron backscatter diffraction (EBSD) is a common method for measuring crystallographic orientations of conductive materials. In this dissertation an Oxford symmetry s3 detector was used in-situ in a ThermoFisher Quattro SEM for EBSD measurements. The technique is usually combined with scanning electron microscope (SEM) systems which already offer an electron beam used for imaging. The EBSD technique involves positioning a flat, highly polished specimen at a shallow tilt relative to an incident electron beam in the path of the electron beam. When the electron beam interacts with the crystal lattice, a portion of the backscattered electrons give rise to diffraction effects. These diffracted electrons impinge upon a phosphor screen placed in close proximity to the specimen surface, producing luminescence upon impact. The emitted light is subsequently captured by a light-sensitive detector generating a characteristic diffraction pattern known as a Kikuchi pattern. These Kikuchi patterns can then be indexed with crystallographic databases to rapidly identify phase and crystal structure. Using a rastered electron beam allows for signal mapping directly to sample coordinates. From the EBSD signal important information like spatial distributions of orientation, misorientation distribution, geometrically necessary dislocations, grain size, phases present, and texture can be obtained making it an incredibly versatile technique. In this dissertation, EBSD is used to scan the individual SSMT samples before testing. Doing this provides accurate grain properties which can then be correlated with the mechanical data to discern which microstructural features contribute to the observed mechanical response.

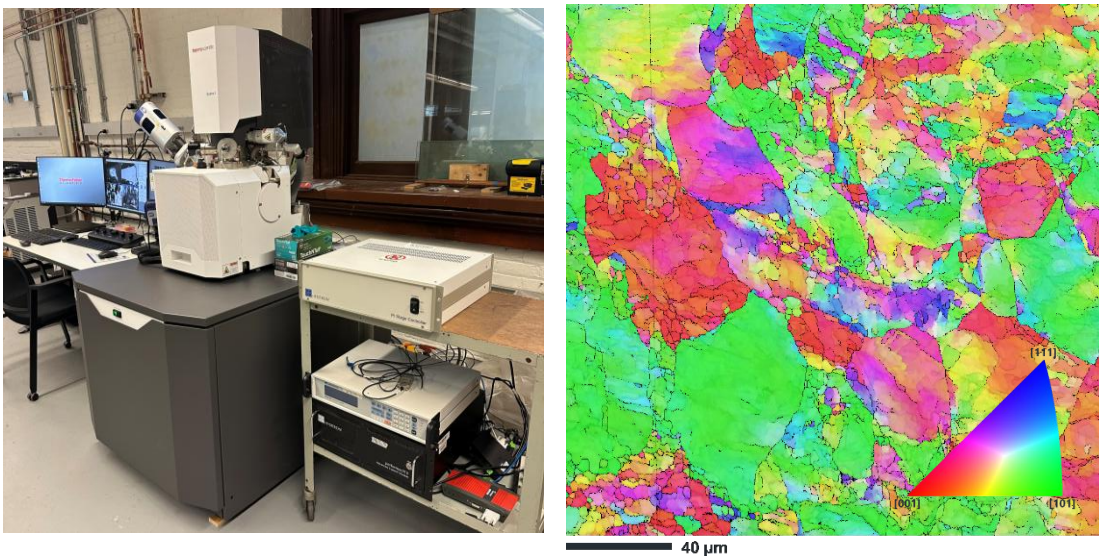

Figure 37. ThermoFisher SEM system with Oxford EBSD detector with example EBSD IPFZ map collected on pure Tungsten

3.1.4 Heat Treatment

Heat treatments for this dissertation to precipitate carbides from the metastable quenched F82H martensite were done using a ThermoScientific Lindberg Blue M tube furnace shown in Figure 38. The tube furnace was modified using an alumina tube connected to a roughing and turbo vacuum pump in order to perform heat treatments in an oxygen deprived environment. For large samples oxidation usually does not play a significant role in experiments where micro-scale oxide layers will not heavily contribute to measured data. However, oxidation of micro-scale structures would greatly affect the mechanical response of the samples, so it was mitigated through using a vacuum environment.

Figure 38. ThermoScientific vacuum tube furnace used for heat treatment

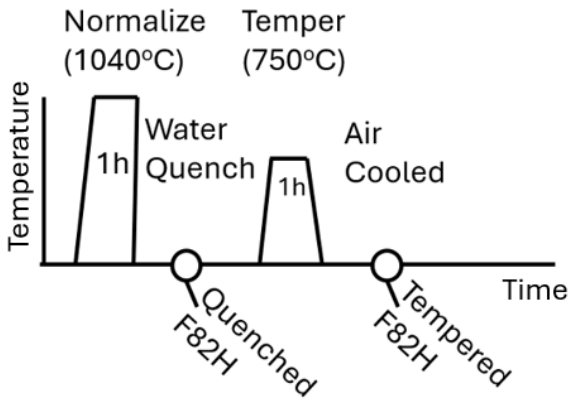

Figure 39. Heat treatments targeted for F82H quenched and tempered conditions.

Figure 39 shows the heat treatments which were targeted to form the quenched and tempered martensitic conditions in F82H. Normalization was targeted for 1040°C for 1h and water quenched to form the quenched condition. This sample was subsequently tempered at 750°C for 1h followed by air cooling to form the tempered condition. The ThermoScientific Lindberg Blue M furnace was monitored by two separate K-type thermocouple systems to ensure the temperature was within ±10°C. These temperatures were chosen based on the original F82H recipe formulated by International Energy Agency (IEA) [60]. Additional studies have chosen to use this heat treatment method finding that carbide precipitation distribution and coarsening is ideal for this tempering condition [71].

3.2 Fabrication Methods

3.2.1 SEM and FIB

Scanning electron microscopes (SEM) are powerful tools which form many of the foundational techniques in modern day materials science. SEMs produce high-resolution images of a specimen's surface by scanning it with a focused beam of electrons. Electrons are emitted from electron sources like a tungsten filaments or field emission guns and accelerated through an electric potential. The beam is then focused and directed onto the sample surface by condenser and objective lenses. When the electron beam interacts with atoms in the specimen, a range of signals are generated through elastic and inelastic scattering events. Secondary electrons (SE) produced by inelastic collisions and backscattered electrons (BSE) produced by elastic scattering events are generated, detected, amplified, and turned into an image through rastering. Modern SEMs can reach electron energies up to 30kV allowing for extremely resolved images to be made of conductive surfaces. In addition to this, characteristic X-rays and BSEs can be utilized for energy dispersive spectroscopy (EDS) and electron backscatter diffraction to obtain elemental characterization and grain orientation information using the same SEM electron beam.

Focused ion beams (FIB) operate similarly to an SEM, but instead of an electron beam, energetic ions like Ga are used. The ions are generated from a liquid metal ion source (LMIS), where gallium is heated and extracted by applying an electric field. These ions are then accelerated through a potential and focused onto the sample surface by a series of electrostatic lenses. When

the high-energy ions interact with the specimen, they sputter away atoms of the sample. The ion beam is then rastered across the sample surface enabling both imaging and site-specific material milling. FIBs are usually used in conjunction with an SEM to create a powerful dual beam tool for precise material imaging and removal. In a dual-beam FIB–SEM configuration, the ion column and electron column are integrated within the same chamber, typically at an angle of 52°. This geometry allows simultaneous imaging, milling, and analysis with the SEM providing high-resolution imaging of the surface while the FIB precisely mills.

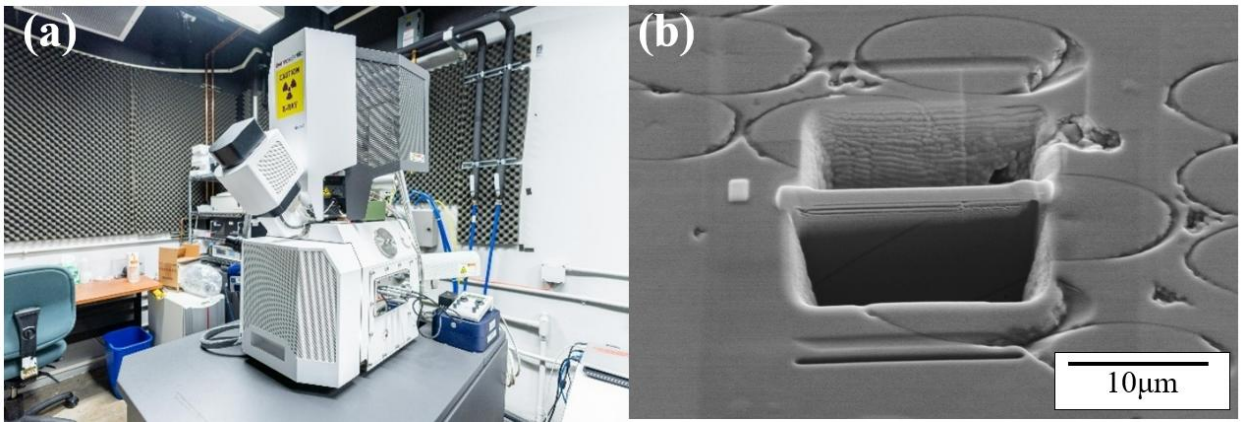

Figure 40. a) ThermoFisher Scios2 Dual Beam SEM/FIB equipped with EBSD, EDS, and BSE capabilities. b) SEM image a FIB trench on silicon carbide

While these capabilities are extraordinary, a limitation of modern dual beam SEM/FIB systems is the relatively slow material removal rates. Due to the reliance on sputtering interactions, this leads to timely and costly milling operations. Often micromechanical samples take hours of FIB time to produce highlighting a limitation of these systems.

3.2.2 Femtosecond Laser Machining

Femtosecond (fs) lasers are a relatively new technology which have seen a massive increase in popularity due to their decreasing costs. While femtosecond lasers have been used in many advanced characterization techniques, with a high enough energy density, their ablation interactions can be leveraged as a rapid machining tool. Fs-laser milling is a highly precise material removal process that relies on their ultrashort laser pulses to ablate material through rapid, non-thermal energy transfer. When a femtosecond laser pulse reaches the surface, the photons interact with the electrons of the material, leading to rapid excitation. If the absorbed energy density exceeds the material's binding energy, the bonds break and the atoms are rapidly ejected from the surface. Combining this with an optical camera which can be mounted in line with the laser and a movement stage, it creates a real-time observable milling tool capable of rapid ablation rates and precise control.

Figure 41. Femtosecond laser setup. Full system with interior view of laser chamber with optics exposed.

The laser ablation process is controlled by several key parameters, including the wavelength, repetition rate, pulse duration, laser power, energy density, spot size, scanning speed, and scanning pattern. Theoretically, laser ablation processes are governed by a threshold energy density needed for ablation which are highly dependent on optical and thermal properties. Once this minimum energy density is reached ablation is allowed to occur.

A key advantage to fs-laser milling is that the pulse duration is shorter than the time required for heat conduction into the bulk material by several orders of magnitude. In theory this makes the fs-lasers unable to create a heat-affected zone (HAZ). This is unlike conventional nanosecond or continuous-wave laser machining, where significant heat diffusion occurs during each pulse creating large HAZs. Compared to dual beam SEM/FIB systems fs-laser machining offers much higher ablation rates with a much cheaper price tag.

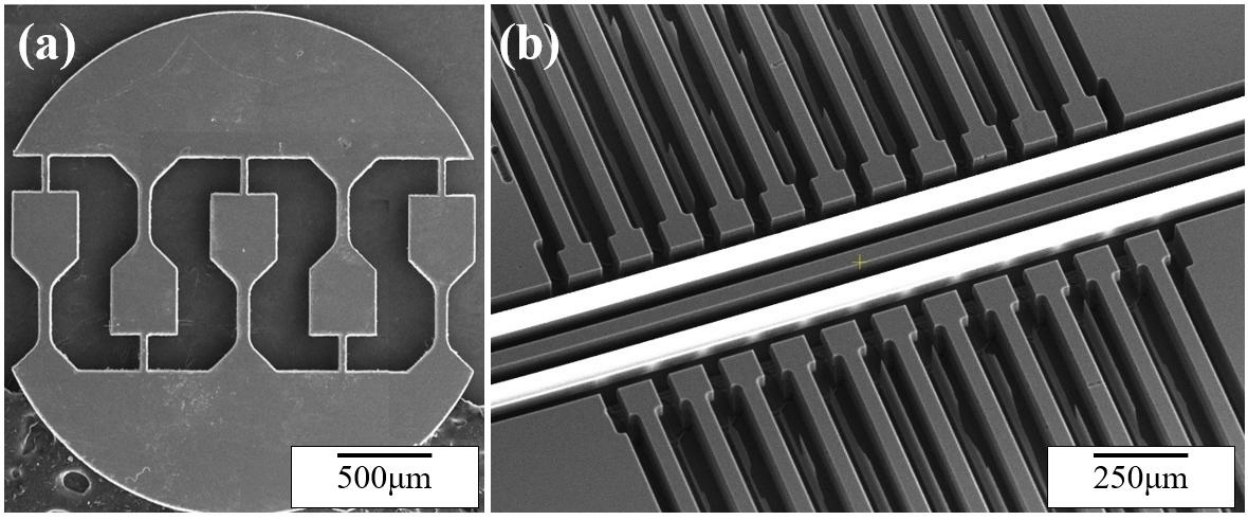

Figure 42. SEM images of femtosecond laser fabricated objects. a) Tensile bar array made from 3mm disc. b) Electrodes made for a quantum computing Paul ion trap

Chapter 4

Feasibility of fs-Laser Milling for F82H SSMT

4.1 Introduction

μMS and microtensile experiments are planned in order to investigate carbide interactions at grain boundaries in F82H. For this, microcantilevers and microtensile samples need to be fabricated. Traditionally, dual beam scanning electron microscope (SEM) and focused ion beam (FIB) systems have been used for the fabrication of micromechanics samples [92]. However, these systems have slow milling rates leading to time and cost intensive sample fabrication. In addition, Ga implantation due to extensive FIB operations may also have influence on the micromechanical behavior of tests [93–95]. Therefore, alternative methods were investigated to be able to rapidly produce SSMT specimen from F82H.

Micromechanics or small-scale mechanical testing (SSMT) aims to probe the mechanical behavior of materials on the micron scale typically when geometrical limitations apply. This technique is commonly used on thin films, where micron scale coatings cannot be tested mechanically in a bulk manner and nuclear materials where large radioactive samples cannot be handled due to safety concerns [33,75]. Micromechanics also enables the study of fundamental science where individual defect interactions can be measured and analyzed. Traditionally, dual beam scanning electron microscope (SEM) and focused ion beam (FIB) systems have been used for the fabrication of micromechanics samples [92]. However these systems have slow milling rates leading to time and cost intensive sample fabrication. In addition, Ga implantation due to extensive FIB operations may also have influence on the micromechanical behavior of tests [93–95].

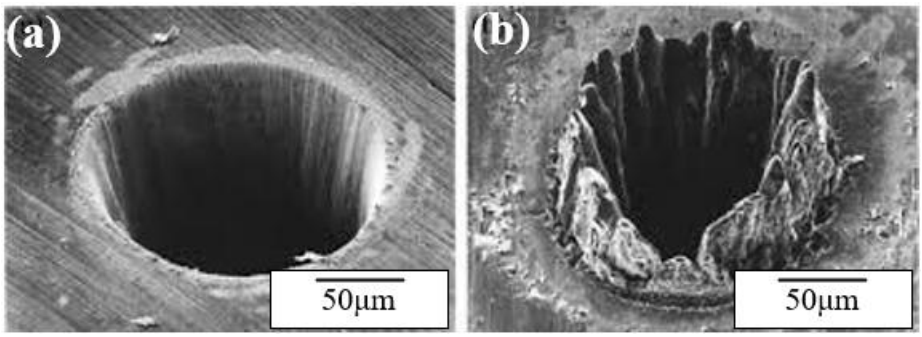

Figure 43. Comparison of: a) femtosecond laser pulse and b) nanosecond laser pulse on steel foil [96].

Compared to a traditional FIB system, femtosecond laser machining currently offers orders of magnitude higher ablation rates for an order of magnitude cheaper price tag [97]. This benefit in ablation rate has the promise of significantly reducing time spent on SEM/FIB systems and increasing research efficiency. A major manufacturer of SEM/FIB microscopes, has even developed an integrated femtosecond laser machining add-on for their systems [97]. However, questions on effects and scale of a heat affected zone (HAZ) and heat accumulation have limited the widespread usage of femtosecond lasers for micromechanical sample preparation. While it is true that a reduced HAZ is observed when compared to longer pulse length lasers like nanosecond lasers, research is ongoing to predict the size, formation, and effects of a HAZ and residual heat accumulation [98]. A comparison between a hole made from a femtosecond and nanosecond laser pulse are shown in Figure 43. Due to the mismatch in time scales of the femtosecond laser pulse with heat transfer from electron to the lattice, no HAZ is expected [98–101]. However, experiments have shown that HAZ can exist in processed materials. Le Harzic et al. estimates their fs-laser HAZ to be less than 2μm deep in Al, Hirayama et al. reports a 0.5-3.5μm HAZ in Cu, and Valette et al. estimates a 1.5μm HAZ for single crystal Al [102–105]. While these HAZ depths are dependent on many factors including laser fluence, repetition rate, pulse duration, and material, it calls into question whether fs-lasers can be used for micromechanic sample processing at the scale below 10um

The use of femtosecond lasers in micromechanics has been used in the past with some success. However, the issue of HAZ is often overlooked and samples are produced on the length scale of tens or hundreds of microns to overlook effects of a potential HAZ [106–108]. Choi et al. made cantilevers with Cu but focused on larger scale cantilevers to mitigate any effect of a HAZ [78]. Pfeifenberger et al. similarly makes large cantilevers >25μm thick to reduce HAZ effects [107]. While these tests are small, experiments like microtensile, micropillar, and microcantilever testing demand gauge lengths of <5μm meaning that HAZs cannot be overlooked.

In this work, a technique is developed to rapidly produce samples for micromechanics experiments using femtosecond laser machining combined together with subsequent with FIB cleaning. This technique is then used to make micromechanical test specimens from pure Ga. Ga is known to be extremely sensitive to heat with an incredibly low melting point of 29.76°C. If any large HAZ or residual heat accumulation were to form when produced and tested at ambient temperature, the specimen would immediately melt making it an ideal material for testing heat sensitivity of this process.

4.2 Methods

99.99% pure Ga was polished into a roughly 100μm thick foil using 1200 grit sandpaper. A wedge shape was formed by polishing at a 5° angle on one side to form a razor edge using 1200 grit sandpaper. Chilled water was used during grinding to prevent melting in the process. Subsequently, the Ga wedge was processed in a Spectra-Physics SpiritOne fs-laser cutting system which uses a Newport three axis stage to control movement. An average power of 0.01W, repetition rate of 20kHz, wavelength of 1040nm, pulse duration of 332fs, scan speed of 10μm/s, and a focused spot size of ~2μm using a 50x Mitutoyo optic were used during machining. The outline of both a microtensile bar and microcantilever were cut using the fs-laser at the razor edge of the

wedge taking around 1min per sample. A Thermo Fischer Scios 2 dual beam SEM/FIB was used to mill the Ga cantilevers and tensile bars into their final shape. The FIB was operated at 30kV and 3nA for the final cleaning and produced a total of 3 microcantilevers and 2 microtensile specimens taking approximately 30mins per sample. The cantilevers had approximate dimensions of 18x4x4μm while the microtensile bars had a gauge section dimension of approximately 4x2x2μm. Figure 44 shows a tensile bar and cantilever following fs-laser processing, FIB cleaning, and mechanical testing.

The FIB cleaned cantilevers and tensile bars were tested using a Hysitron PI-88 in-situ picoindenter system. The cantilevers were bent through compression at the cantilever tip using a 1μm wedge tip and a load-controlled rate of 5μN/s. The tensile bars were uniaxially pulled using custom made diamond shoulder grippers at a displacement-controlled rate of 5nm/s. Dimensions of the microcantilevers and tensile bars were imaged using SEM for later correlation. All preparation and testing of the cantilevers and tensile bars were performed at room temperature.

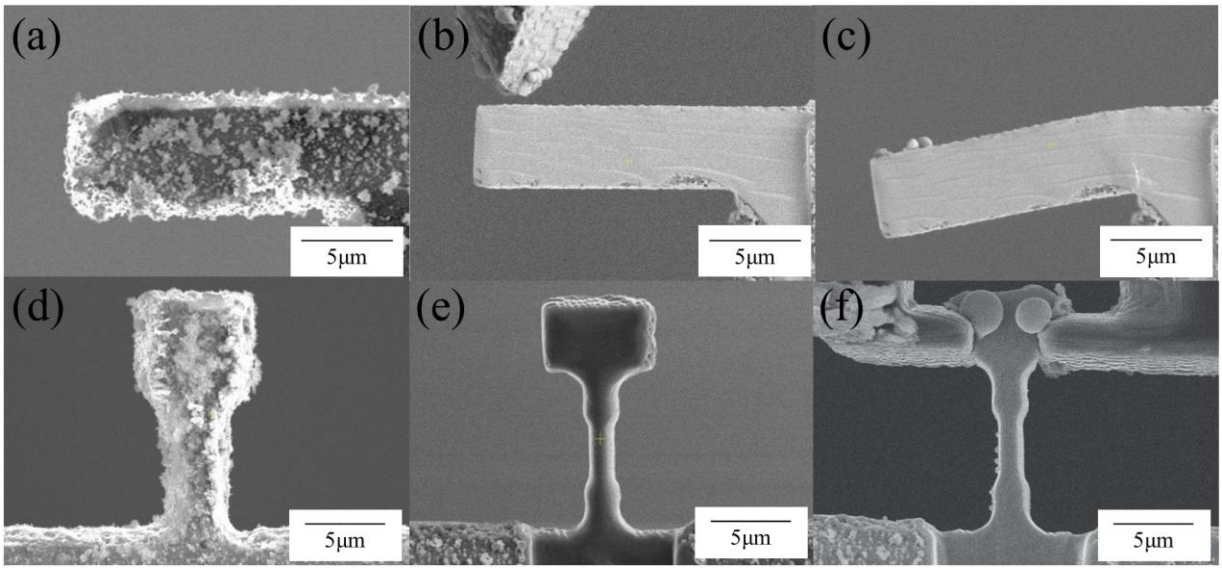

Figure 44. (a) Fs-laser processed gallium microcantilever and (d) tensile bar. (b) The same specimens after FIB cleaning of microcantilever and (e) tensile bar. (c) The same specimens after mechanical testing of microcantilever and (f) tensile bar.

4.3 Results & Discussion

Figure 44(f) shows a still SEM image of a Ga microtensile bar during uniaxial tensile testing. Upon contact with the gripper, melting at the shoulders of the tensile bar was observed. It is likely that the friction between the grippers and microtensile was enough to melt the Ga. Due to this, it is impossible to perform a tensile test on Ga using this approach however, a support coating or cooled stage would remedy this issue. Also, the fact that the Ga readily melted without any surface modification is an indication that no significant oxide scale formed during processing.

Figure 45(a) shows an SEM image of a Ga cantilever after failure following mechanical loading at the tip. Small droplets formed where the tip touched the sample likely due to the combined influence of plastic indentation deformation and melting from friction contact similar to what was observed on the tensile sample. However, the cantilever as a whole was able to deform. The compiled load-displacement curves for all tests are also shown in Figure 45. Melting due to the friction of contact between the cantilever and diamond tip contributed to the initial nonlinearity in the elastic region as well as the load decrease following maximum bending stress. Mechanical properties can be calculated using the conventional classical mechanical approach with a bending stress of $\sigma=PLy/I$, strain of $\varepsilon=3dy/L^2$ and elastic modulus of $E=\sigma/\varepsilon=PL^3/3dI$. Here, P is the applied load, L is the loading point distance, y is the distance to the neutral axis, I is the moment of inertia for a rectangular beam, and d is the recorded displacement.

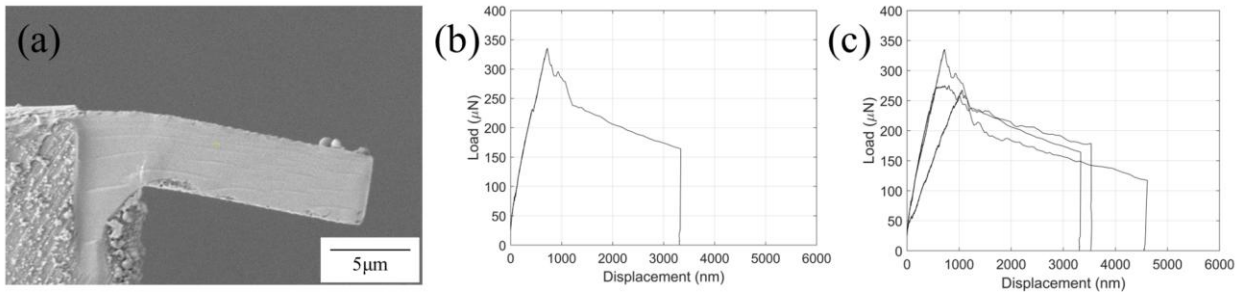

Figure 45. (a) SEM image of gallium cantilever failure. (b) Stress-strain curve of the cantilever in (a). (c) Compilation of all recorded cantilever stress-strain curves.

From the microcantilever testing, an elastic modulus of 9.67 ± 0.35GPa, maximum bending stress of 309.46 ± 35.76MPa, and maximum strain of 15.27 ± 1.16% can be extrapolated as an average for all cantilevers tested. Euler-Bernoulli beam theory states that cantilever beams under a point load have a gradient region of maximum tension on the top surface and maximum compression on the bottom surface. However, we can observe that the material does strain significantly in tension but forms a distinct crease in the compression region upon failure. Furthermore, the bending stress of >300MPa is unexpectedly high for Ga that melts just a few degrees above the test temperature. Wilson et al. finds the critical resolved shear stress of Ga is between 1-6MPa in single crystal tension testing [109]. Wang et al. further reports that Ga exhibits low tensile strength and high tensile ductility reaching yield strengths of 8-22MPa and total strains of over 55-110% depending on solidification method [110]. Even accounting for the length scale effects on mechanical property [75,111], the bending stress is higher than expected and a further exploration into the anisotropy of Ga is needed to explain this behavior.

One of anomalies in the present study pertains to the fracture behavior exhibited by the Ga microcantilevers. As clearly depicted in Figure 45(a), fracture initiation consistently occurred at the lower surface across all three tested specimens. This failure mode represents a stark departure from the conventional fracture mechanism typically observed in ductile metallic materials under flexural loading, wherein crack initiation commences at the top surface where maximum tensile stress is concentrated. We attribute this phenomenological deviation to the intrinsic thermophysical

properties of Ga, particularly its exceptionally low melting point of 29.76°C. The ambient temperature (~25°C) at which the experiments were conducted effectively places the material in a regime immediately proximate to its melting point, corresponding to a homologous temperature exceeding $0.97T_m$. This condition significantly surpasses the widely accepted threshold for activating high-temperature creep ($0.4–0.5T_m$), strongly suggesting that the operative deformation mechanism is not simple dislocation plasticity but rather diffusion-controlled viscoplastic flow.

Conceptually simplifying the cantilever bending test, the upper section experiences tensile stress while the lower section undergoes compressive stress. In this extreme high-temperature environment of $0.97T_m$, materials may exhibit behavior analogous to superplasticity. Under such superplastic deformation, stress concentrations associated with necking are suppressed; the material potentially deforms, accompanied by the formation and growth of defects, such as micro-voids, uniformly. Thus, tensile stress appears to be effectively released or relaxed via uniform changes in geometry.

Conversely, the material response under compressive stress is distinct. Compressive stress inherently tends to close defects such as micro-voids during deformation. Consequently, to accommodate strain while overcoming geometric constraints, the material enters an unstable deformation mode characterized by localized buckling or the formation of creases. Indeed, such distinct buckling is evident near the fracture site in Figure 45(a). This behavior can be understood by analogy to the wrinkling observed when viscoplastic materials, such as clay, are compressed. This localization of deformation constitutes stress concentration and serves as the principal mechanism driving fracture initiation at the cantilever's lower surface.

This asymmetric deformation behavior implies that the tensile portion behaves as 'weaker' (i.e., accommodates deformation more readily). To maintain mechanical equilibrium across the beam's cross-section, the neutral axis of flexural stress must migrate towards the compressive (lower) side, thereby increasing the area subjected to tensile stress. This migration fundamentally impacts the interpretation of the calculated stress values. The maximum bending stress reported herein (309.46 MPa) represents an 'apparent stress' derived from classical beam theory ($\sigma = My/I$), which implicitly assumes the neutral axis resides at the geometric centroid. (Here, I is the moment of inertia) However, owing to the actual downward shift of the neutral axis induced by the superplastic-like tensile deformation, the true distance from the neutral axis to the point of fracture initiation less than the distance (y) assumed in the calculation. Given that bending stress scales linearly with this distance, the actual flexural stress (M) at which the material failed must necessarily be lower than the calculated apparent stress of 309.46 MPa.

Consequently, the value of 309.46 MPa constitutes an overestimation of the material's true compressive strength or buckling limit under these conditions. In summary, the material reached its critical deformation state under an actual compressive stress lower than 309.46 MPa. Therefore, a rigorous elucidation of the intrinsic mechanical properties necessitates future investigations employing more sophisticated methodologies, such as finite element modeling (FEM) incorporating viscoplastic constitutive laws that explicitly account for this tension-compression asymmetry.

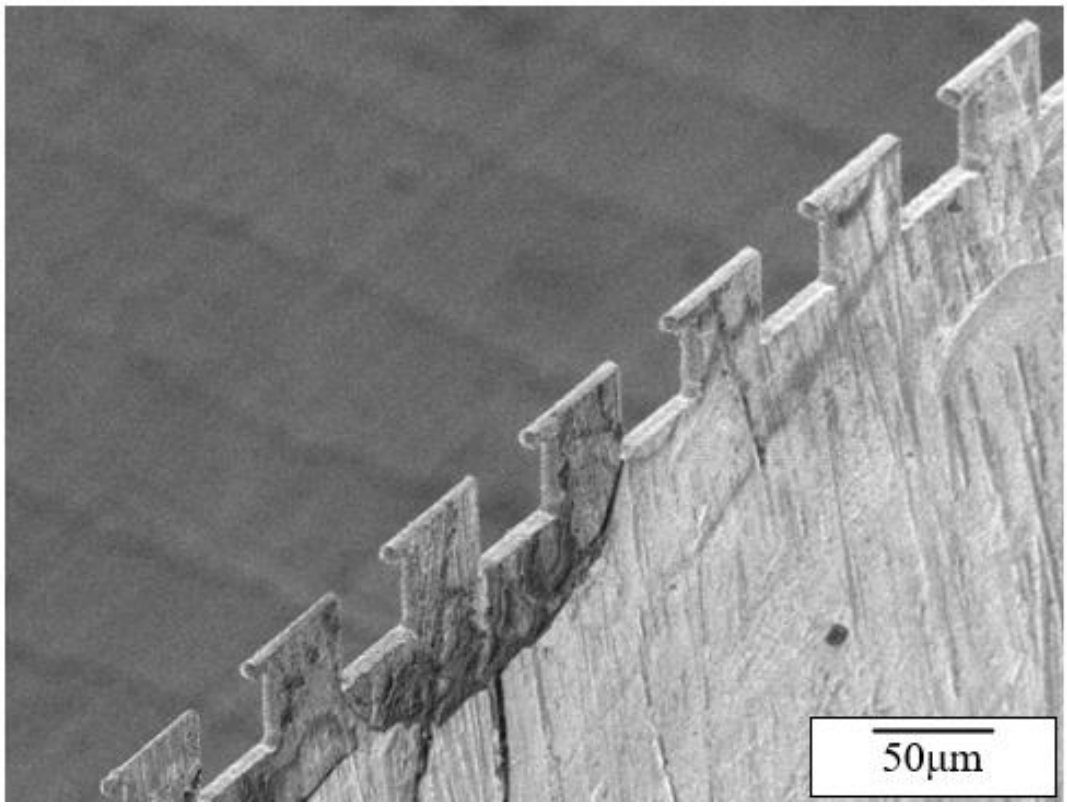

Figure 46. Lasered cantilever array on Ga showing speed and reproducibility of process

While the material properties of micron-scale Ga are interesting, the fact that any testable specimen at all were yielded from this process is the main finding of this study. If any part of this process resulted in a temperature increase of only ~4°C the entire sample would melt, and no testable specimen would have been machined. Particularly the fs-laser process, initially questioned for its potential for residual thermal affects, produced no observable HAZ or heat accumulation effects which exceeded the ~4°C temperature increase needed to melt the sample. Some areas show evidence of exceeding the melting point of Ga near the sharp corners of the cantilevers and corners of the microtensile bars, however these areas are very minimal and are easily FIB milled away before testing. The presence of pre-existing surface morphological features like grinding scratches bolster the fact that no melting occurred the samples. Multiple times during sample preparation, testing samples melted due to extended handling and FIB beam heating but not during fs-laser processing at the identified parameters. However, at larger powers, defocused working distances, and increased repetition rate, it was found that fs-laser melting could be observed. This result serves to bolster previous claims of the importance of fluence and repetition rate on HAZ formation when thermal dissipation is outpaced by heat accumulation due to laser irradiation [112,113].

4.4 Conclusions

This study gives an optimistic view of the use of femtosecond lasers in rapidly producing micromechanical test samples. A process for creating a wedge specimen, bulk machining using a

fs-laser, and final cleaning using a FIB was demonstrated on Ga. This serves to physically exhibit the “cold processing” capabilities of fs-laser machining even the micron-scale. While HAZ formation and heat accumulation can still occur in ultrafast laser systems, a well calibrated fs-laser with finely tuned parameters can mitigate this to a negligible point for use in micromechanics.

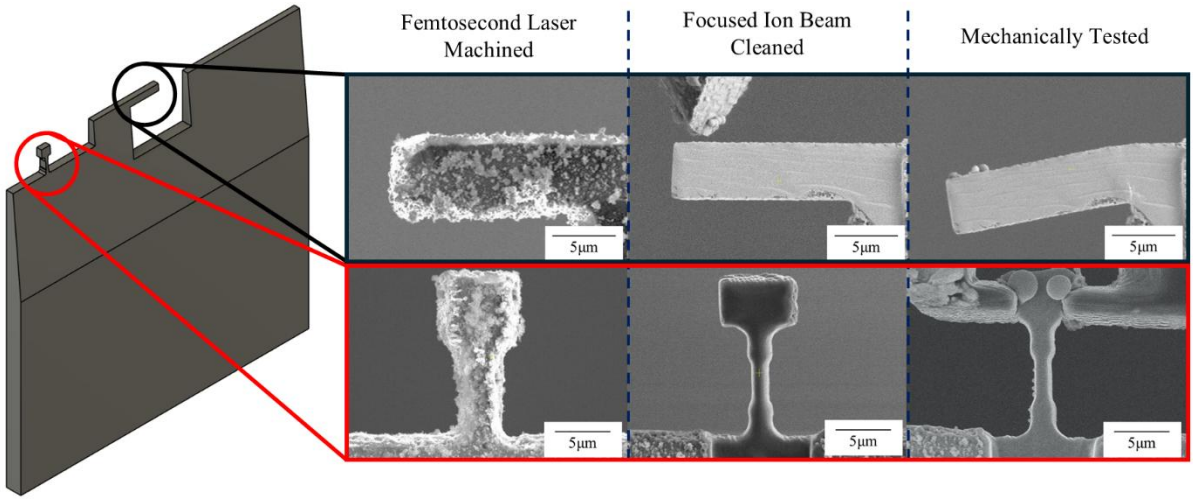

Figure 47. Summary of micromechanics sample preparation and testing on gallium

The process developed as a result of this study was used for the preparation of SSMT samples on F82H. The full procedure developed is shown in Figure 48 and Figure 48. The same laser system and laser parameters with an average power of 0.01W, repetition rate of 20kHz, wavelength of 1040nm, pulse duration of 332fs, scan speed of 10µm/s, and a focused spot size of ~2µm using a 50x Mitutoyo optic were used during machining. This was done to ensure the minimal heat impact during the machining process as was shown in this chapter.

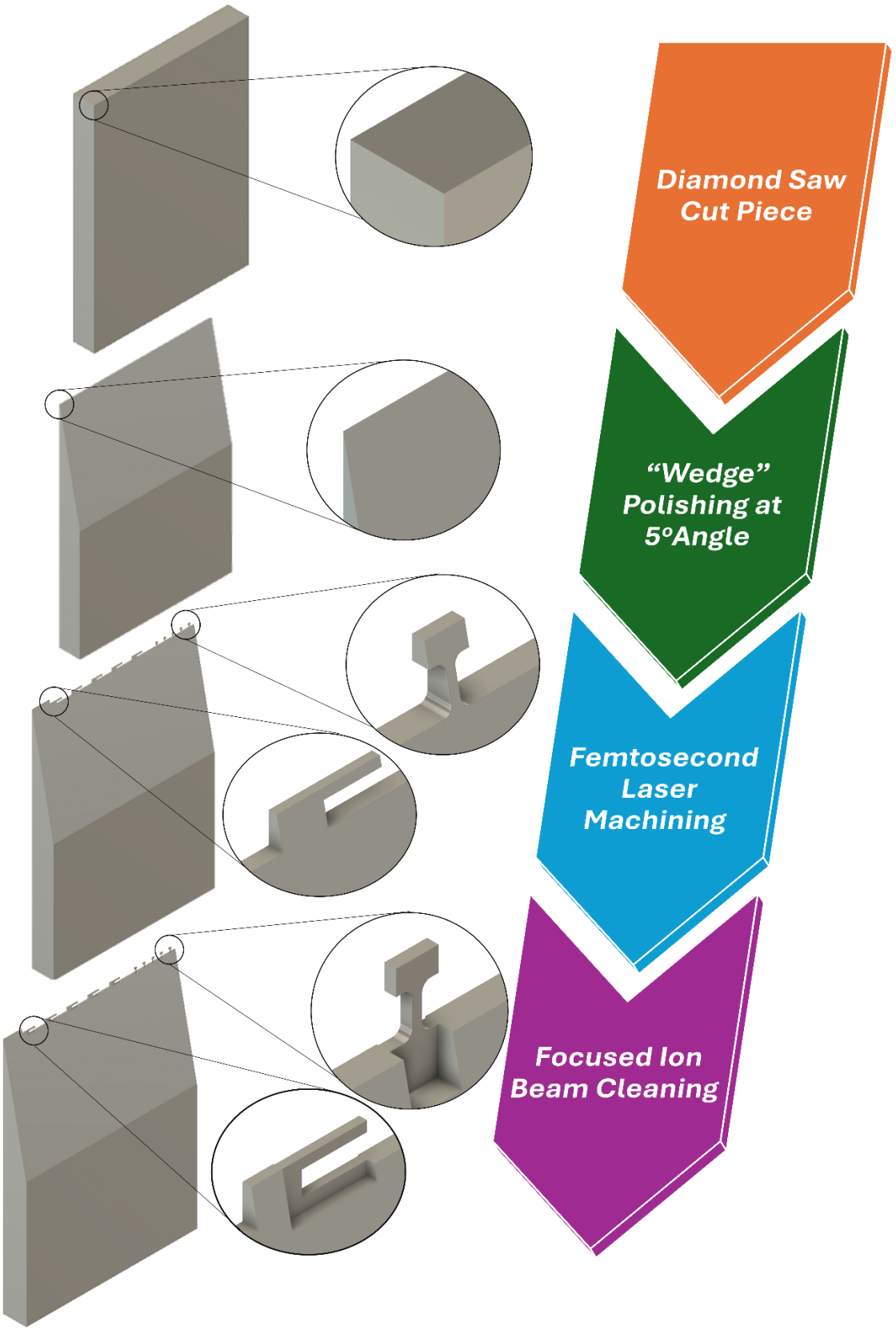

Figure 48. Joint fs-Laser and FIB sample preparation approach to making small scale mechanical testing specimen

Chapter 5

Bridging Length Scales: Micro to Macro Scale Correlations

5.1 Introduction

Chapter 4 focused on the feasibility of leveraging fs-lasering in the use of SSMT where a study on a temperature sensitive material established a technique for rapid undamaged SSMT sample manufacturing. However, SSMT still suffers the drawback of not being representative of bulk scale mechanical testing. Hosemann et al. explores this in depth, and it is commonly thought that the increasing number of defects sampled contributes heavily to the observed weakening effect at larger length scales shown in Figure 49. Discovering the length scale dependence of different material properties remains an active area of research as different mechanisms contribute to observed increasing or decreasing in material property when varying the size of test. While SSMT is planned for F82H to investigate carbide mechanical behavior at interfaces, extrapolating these trends to the bulk scale requires an understanding of mechanical property changes across length scales. In order to further investigate this trend, an experiment was conducted on a another material relevant to the nuclear industry, Zircaloy-4. While Zr alloys have a different crystal structure, the fine grain size and dislocation density of cold rolled Zircaloy-4 tubing serves as an adequate surrogate for the expected mechanical shifts due to length scale in F82H.

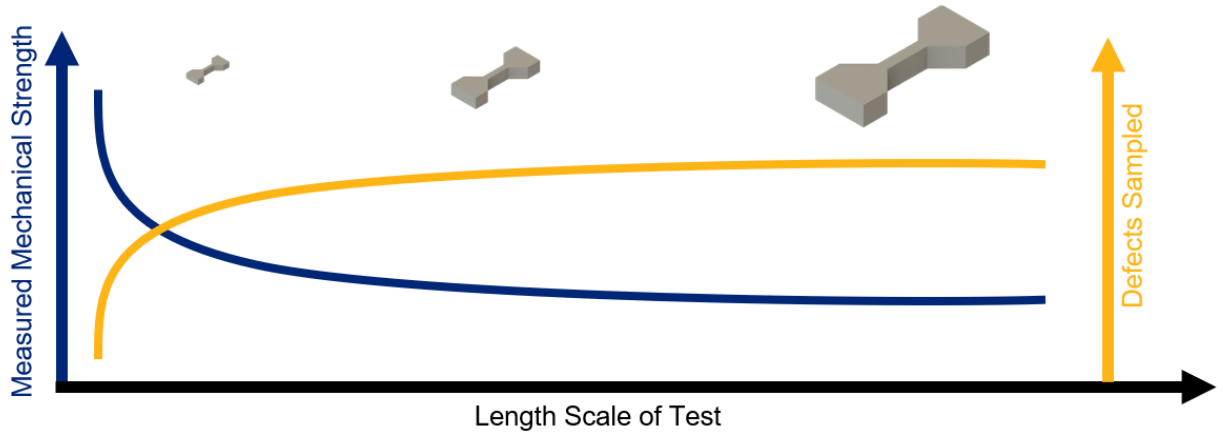

Figure 49. Length scale effects on measured mechanical strength adapted from Hosemann et al. [75].

Zircaloy-4 is one of the most common cladding materials for fuel rods in nuclear fission reactors due to its low neutron absorption cross-section, high strength, ductility, and corrosion resistance at elevated temperatures in light water reactor (LWR) environments. Typical pressurized water reactor (PWR) Zircaloy-4 tube geometries, which generally have outer diameters of 5-10mm

and wall thicknesses of 0.5mm, offer a unique challenge for standard mechanical testing techniques. An example Zircaloy tube with this geometry is shown in Figure 50. The tubes have a unique mechanical anisotropy introduced via preferential crystallographic texture of the hexagonal close-packed (HCP) structure and only material produced in a similar fashion delivers accurate tests. Variables such as wall thickness reduction ratio, forming, and heat treatment significantly alter the microstructure, so it is desirable to use realistic cladding tubes to measure mechanical properties. However, tube geometries present testing challenges compared to flat plates [114]. Common solutions such as the Axial Tube Tension (ATT) and Ring Hoop Tension (RHT) tests, have been used to reflect uniaxial components of in-service conditions [115,116]. While these tests were able to produce a bulk-like response in thin-walled tube materials, they fall short in accurately representing the state of in-service bi-axial stress conditions [115–117]. These drawbacks can be remedied by utilizing finite element models which can correlate the results to pressurized tube testing that more accurately simulates in-service conditions, as demonstrated by Kamerman *et al.* [118].

The Zircaloy-4 thin-walled tube geometry combined with radioactivity created from material neutron activation has created a need for bulk-like mechanical property evaluation using minute radioactive volumes. Macro-scale tensile testing following ASTM E8 guidelines for metallic materials is the industry standard for mechanical testing [119]. However, these geometries are often too large for radioactive materials which are both limited in volume due to reactor irradiation constraints and can exceed worker radiation dose limits. Furthermore a thin-walled tube does not allow such geometries as presented in ASTM E8 guidelines. One approach used to address this challenge is the extrapolation of small-scale mechanical testing (SSMT) results to the bulk scale.

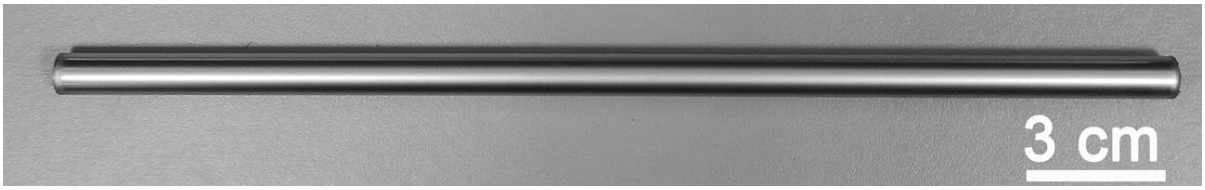

Figure 50. Zircaloy-4 tubing [120].

SSMT on the micro-scale has been employed to study fundamental mechanical behaviors for decades. With regard to nuclear materials, this length scale is essential due to the low volume and dosage restrictions. Typical ways to machine micro-scale geometries have included focused ion beam (FIB) milling, electron beam lithography (EBL), and other lithography techniques [121,122]. While fundamental insights into isolated material defects like grain boundaries and precipitates can be gained, extrapolating these results to the bulk-scale has proven to be challenging [75]. Changes in the deformation mechanism and microstructural effects depending on the length scale have to be considered for accurate correlations with bulk scale testing [75,76]. Plastic instabilities are especially sensitive to size effects like grain size, testing geometries, and strain rates [123].

While SSMT samples can be fabricated using FIB or lithography methods, producing samples at this length scale which capture multiple grains on a cladding tube geometry is simply

cost and time-prohibitive due to the large dimensions needed compared to the low removal rate of a FIB. Femtosecond laser machining offers a high-throughput method for machining tensile dogbone specimens for mechanical testing. High ablation rates combined with a <5μm heat affected zone (HAZ) create suitable conditions for machining defect free structures on the meso-scale, reducing radioactive exposure doses compared to bulk scale samples [99,124,125]. While an ASTM standard geometry has not been developed for this length scale, previous studies performed by Dong *et al.*, Harvey *et al.*, and Gigax *et al.* demonstrated that regionally selective bulk-like properties can be obtained on stainless steel alloys using fs-laser machined meso-scale tensile bars [76,77,126]. An image showing the size of these tensile bars is shown in Figure 51. However a common issue with this meso-scale mechanical testing is that microstructural features such as grain size and micro-texture significantly influence data fidelity and consistency highlighting a key drawback of this method.

In this study we correlate fs-laser machined meso-scale tensile testing with SSMT data on industrial Zircaloy-4 cladding. Despite the complicated, highly textured Zircaloy-4 cladding microstructure with variable grain sizes, we are able to generate useful bulk-like materials property values using micro- and meso-scale uniaxial tensile testing. This workflow outlines a path towards conducting similar machining and testing procedures on active irradiated samples without the need of large hot cell facilities.

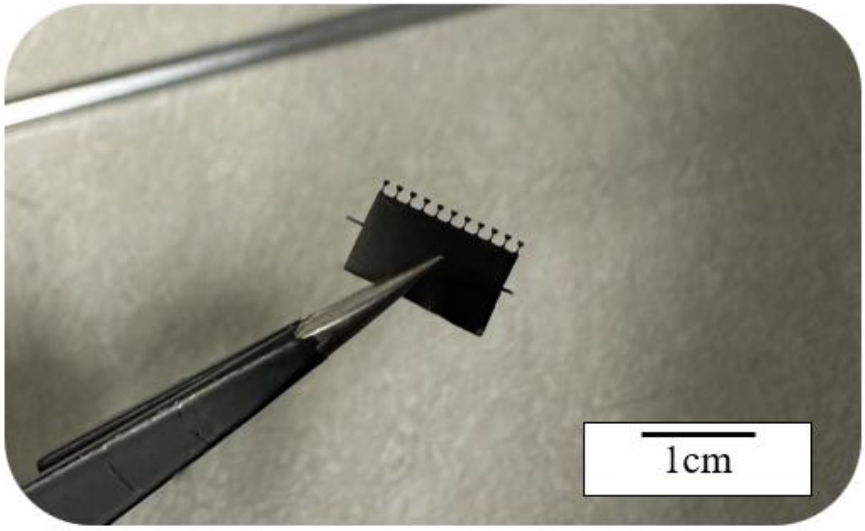

Figure 51. Femtosecond lasered mesoscale tensile bars

5.2 Methods

Commercial Zircaloy-4 tubes with a diameter of 9.5mm and wall thickness of 0.57mm were procured with a composition listed in Table 2. Three tensile geometries were chosen for this study and their dimensions are shown in Figure 52. These include two sizes of micro-scale tensile bars along with a meso-scale geometry. Henceforth, the smaller micro-scale geometry, the larger micro-scale geometry, and the meso-scale geometry will be labeled by their gauge widths: “2μm”, “7μm” and “80μm” respectively for simplicity. The 2μm, 7μm, and 80μm geometries had

approximately square gauge cross sections with thicknesses of 2µm, 7µm and 100µm respectively. The 2µm and 7µm geometries were prepared in the axial direction using a gallium ion FIB and plasma Xe FIB with two varying tensile geometries. A total of eight 2µm and eleven 7µm geometries were FIB produced. In addition to this, four 2µm and seven 7µm of the tensile bars were made from an irradiated tube of Zircaloy-4. This irradiated tube with an ID of "R-05" was part of the Accident Tolerant Fuels 2 (ATF-2) experiment and was irradiated at the Advanced Test Reactor (ATR) Loop 2A at Idaho National Laboratory (INL). The rod was loaded with UO_2 fuel and irradiated during the period of June 2018 to September 2019 with multiple pauses during testing. This rod was able to achieve a burnup of 9.27 GWd/tHM at temperatures ranging from 250°C to 280°C [115,127,128]. Kamerman et al. calculates this rod's fast fluence as 1.98×10^{25} n/m^2 using a coupled Monte Carlo N-Particle (MCNP) and ORIGEN methodology [129]. Rough milling of the SSMT tensile samples was conducted at 30kV and 60-2000nA while final cleaning used 30kV and 0.5-10nA. Both geometries were given a small curvature at the bottom and top of the gauge section to mitigate stress concentration at sharp edges. The final geometry was measured in an SEM to verify dimension and correct the stress measurement. These tensile dogbones were then tested *in-situ* with a Hysitron PI-88 SEM picoindenter equipped with custom FIB-milled tensile shoulder grippers to fit each tensile geometry. The testing was load-controlled at a rate of 10nm/s and videos of each tensile test were recorded. For the micro-scale geometries, the load-displacement data was converted to stress-strain using the final measured gauge dimensions, with no additional processing being performed.

	Zr	Sn	Fe	Cr	O	C	H
%	Bal.	1.22	0.19	0.11	0.13	0.020	0.0017

Table 2. Zircaloy-4 nominal composition in wt%

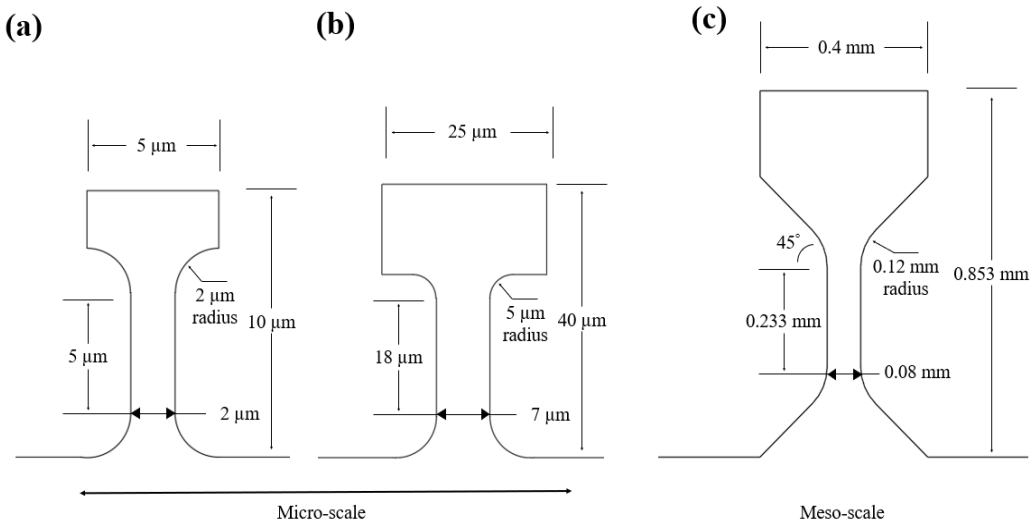

Figure 52. Schematic illustration of all tensile geometries. (a) 2µm geometry. (b) 7µm geometry. (c) 80µm geometry.

The meso-scale 80µm tensile specimens were prepared from a 100µm thick foil sample of Zircaloy-4 tubing which was sectioned using a high-speed diamond saw. The sample surface on both sides was polished from 600 grit sandpaper to a final solution of 1µm diamond suspension.

The foil was machined using an 8W Spirit One fs-laser combined with a Newport microfabrication workstation to control movement. The laser system was run at a power of 3W, a laser wavelength of 1040nm, a pulse duration of 332fs, and a repetition rate of 50kHz using a Mitutoyo NIR 10x objective lens which has a focused spot size of ~10μm. A compressed air gas flow was used to assist in removing ablation particles during cutting. The 80μm tensile geometry is shown in Figure 52 and the gauge section was machined parallel to the axial direction of the tube to mimic an ATT test. The tensile bars were given a 0.12mm radius curvature at the top and bottom of the gauge section in order to mitigate potential fracture sites at sharp corners. Following laser machining, the tensile bars were quickly immersed in a bath of ethanol in an ultrasonic cleaner to remove excess ablation particles on the surface. Six 80μm geometries were produced using the fs-laser and each took approximately 3 minutes to fabricate highlighting the rapid ablation rates that can be achieved with this process. A small taper of approximately 3° was observed on all the meso-scale tensile bars due to the lasering process creating a slightly trapezoidal cross-sectional shape which was corrected for in the reported stress. The effect of this taper on deviations in the uniaxial stress state of the tensile bar was mitigated by using laser-machined shoulder grippers which had the same tapering angle, meshing them together. The lasering process also created a small ripple-like texture on the surfaces parallel to the beam which is not expected to affect results and can be seen in Figure 54 [77]. These tensile dogbones were tested in a Kammrath-Weiss compression and tension module equipped with custom laser-machined shoulder grippers. The tensile tests were run in displacement control at a strain rate of 0.1%/s. For the meso-scale testing, direct image correlation (DIC) was used to correlate the strain and correct for machine compliance. Machine compliance was further corrected by using a material with a known elastic modulus and adjusting the measured strain values accordingly. A 3D visualization of all tensile geometries is shown in Figure 53 and SEM images are shown in Figure 54.

Microstructural examination was performed using a Thermo Fisher Scios 2 DualBeam SEM equipped with an Oxford Symmetry S3 electron backscatter diffraction (EBSD) detector . Prior to examination the surface was mechanically polished from 600 grit sandpaper to a 0.02μm colloidal silica solution and then cryo-electro polished at 0°C for one minute. Microstructure analysis and visualization were performed using the ATEX software package [130]. We define the normal direction (ND) as the radial axis, the transverse direction (TD) as the hoop axis, and the rolling direction (RD) as the axial axis. The EBSD inverse pole figure (IPF) map was acquired from the ND showing the RD-TD plane.

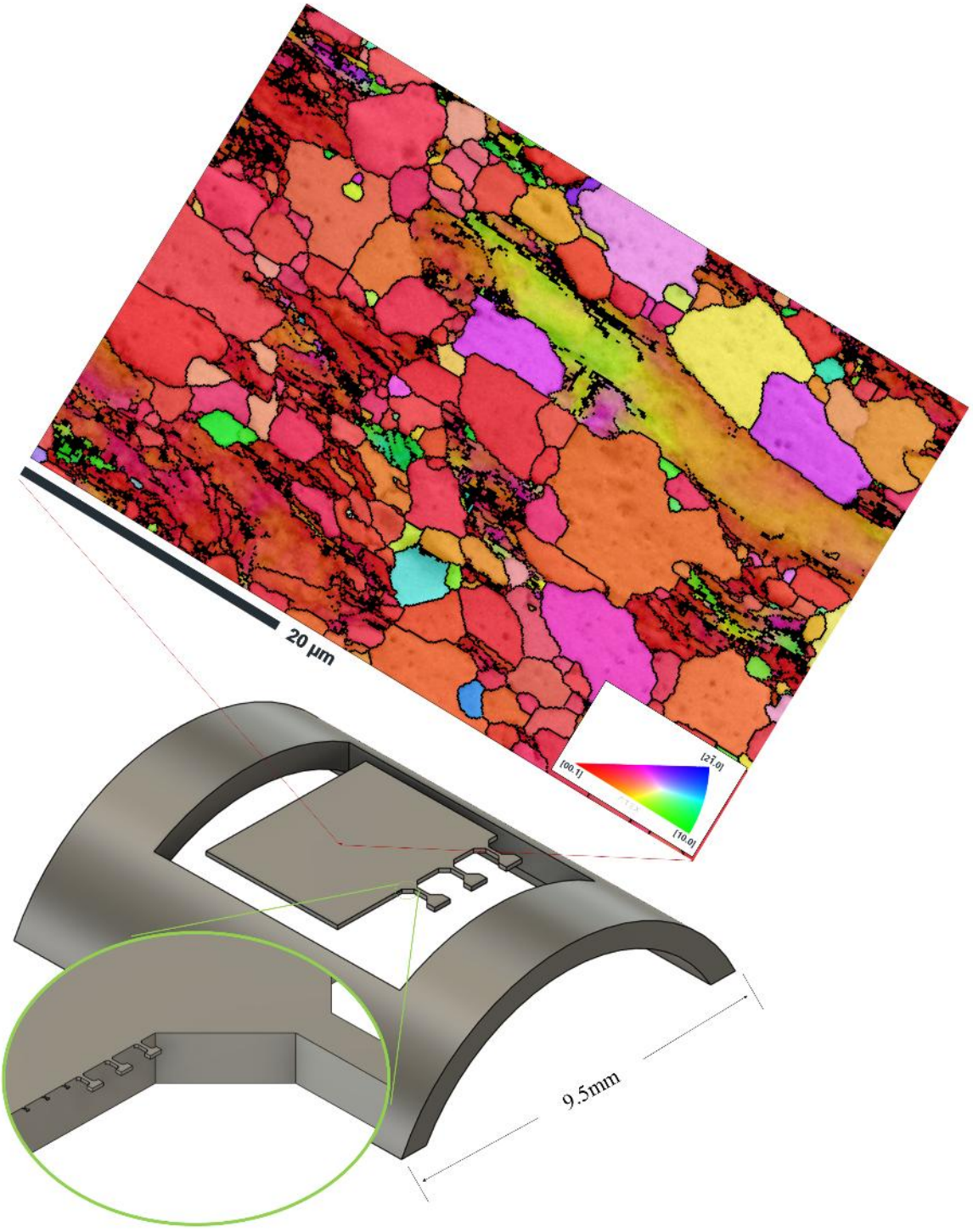

Figure 53. Section of Zircaloy-4 tubing with a scaled schematic illustration of all tensile geometries with EBSD IPF map. A legend color scheme key is presented in the form of a stereographic triangle in the bottom right corner of the EBSD orientation map [117].

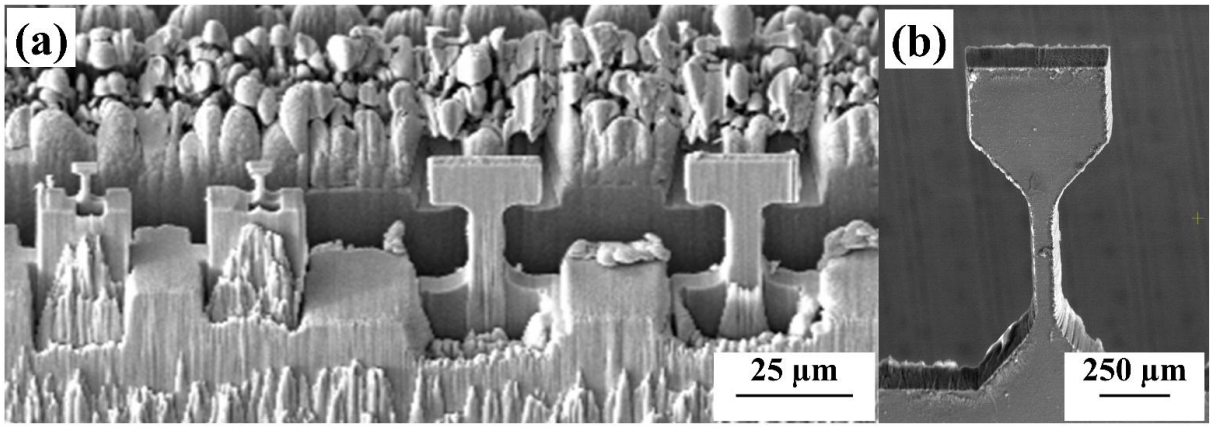

Figure 54. (a) FIB fabricated 2µm tensile bars (left) and 7µm tensile bars (right). (b) fs-Laser fabricated 80µm tensile bars

5.3 Results

The results of the EBSD scan are shown in Figure 53 using a ND-projection IPF visualizing the texture and grain morphology of the cladding. There is a strong texture in the grains of the tube with a general preference for the basal plane normal oriented parallel to the ND (radial) direction of the tubing. This texture is a result of the pilger processing used on the Zircaloy-4 tubes used to reduce the tube wall thickness. In the paper by Nelson *et al.* which analyzed the same Zircaloy-4 alloy batch it was found that the grain sizes of the tubing followed a bimodal distribution with many islands of fine nanometer scale grains forming within a matrix of larger grains [117,131]. The area-weighted average grain size is 4.83µm where grains within two standard deviations fall between 0.44-11.38µm. Using this approximation for average grain size, the 2µm, 7µm, and 80µm geometries contained approximately 0.2, 2.7, and 436.6 grains within the gauge area.

The raw load-displacement data for all the tensile testing was converted to stress-strain curves and is displayed in Figure 55. The strain-to-failure was found by visually inspecting the recordings of each tensile test and correlating where fracture initiated, which correlated to a large load drop. From this data, values for 0.2% offset yield stress, ultimate tensile strength (UTS), and strain-to-failure were calculated and are shown in Figure 56.

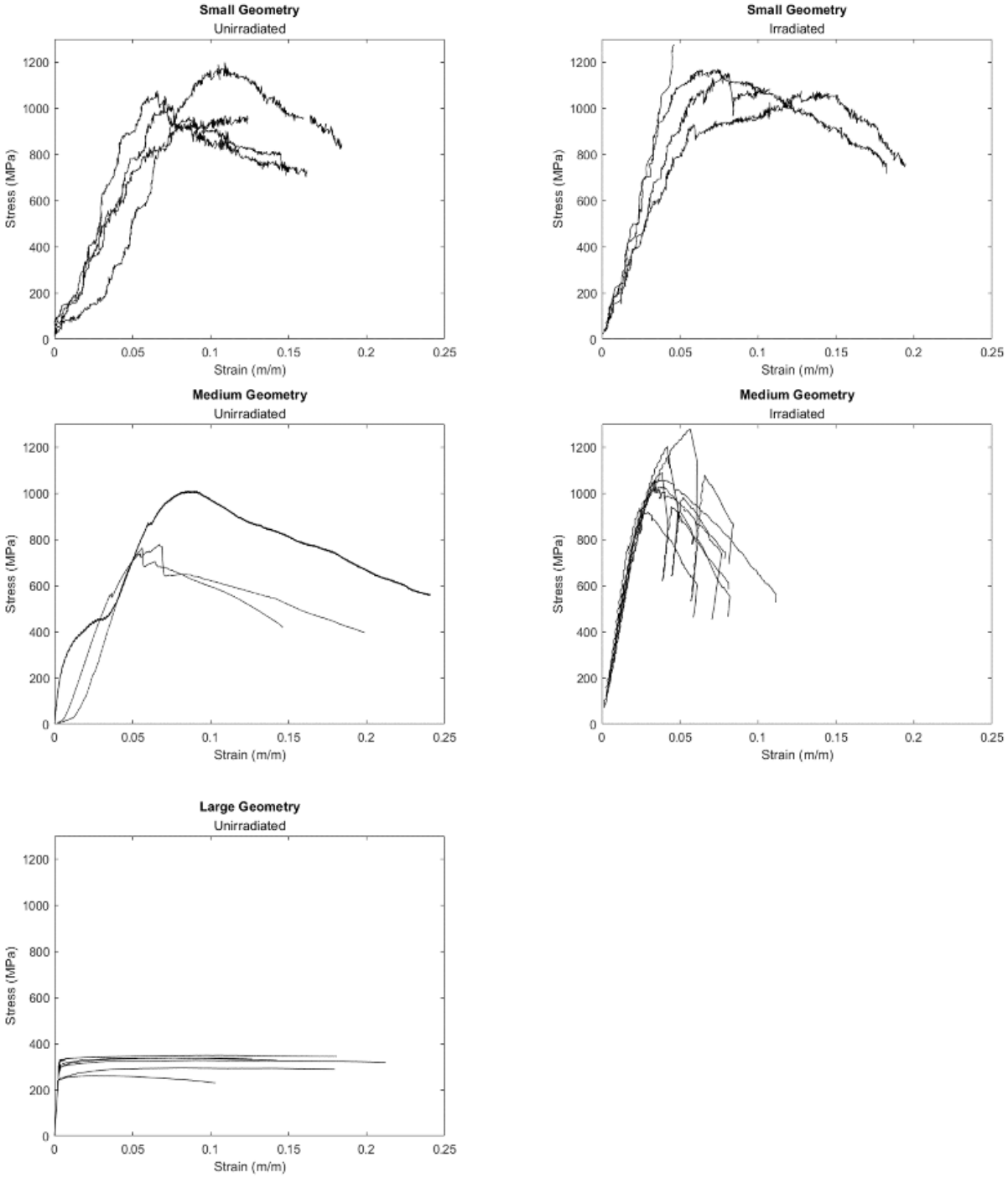

Figure 55. Compiled Zircaloy-4 stress-strain curves to failure for all tensile geometries

Tensile Bar	Length Scale	Gauge Width and Gauge Thickness (µm)	Gauge Length (µm)	Tensile Bars Tested	Yield Stress (MPa) ± STD	UTS (MPa) ± STD	Strain to Fracture (m/m) ± STD
2µm	Micro-	2	5	4	946.7 ± 161.2	1069.5 ± 98.2	0.154 ± 0.025
2µm Irradiated	Micro-	2	5	4	1106.6 ± 130.4	1167.9 ± 82.2	0.133 ± 0.069
7µm	Micro-	7	18	4	737.0 ± 138.8	851.4 ± 138.8	0.195 ± 0.047
7µm Irradiated	Micro-	7	18	7	877.7 ± 56.1	1081.9 ± 110.1	0.082 ± 0.015
80µm	Meso-	80	233	6	290.1 ± 33.0	318.0 ± 6.74	0.157 ± 0.040
Reference Bulk Scale (ATT) [2]	Bulk-	570	14500	1	262.5	416.74	0.138
Reference Bulk Scale (ATT) Irradiated [2]	Bulk	570	14500	1	764.5	854.0	0.066

Figure 56. Analyzed data for Zircaloy-4 stress-strain curves of all tensile geometries

5.4 Discussion

Both unirradiated and irradiated 2µm geometries deformed with similar strain-to-failures and yield stresses, however, some differences in the stress-strain curves can be attributed to irradiation. The yield stress of the irradiation condition is higher, however, both seemed to deform in a largely ductile manner as evidenced by the comparable strains. Macro-scale testing on Zircaloy-4 shows a considerable decrease in strain due to irradiation hardening and embrittlement effects however this trend is not as pronounced [115,132,133].

The deformation behavior of the unirradiated and irradiated 7µm tensile bars differed significantly. In general, for the irradiated condition, plastic deformation occurred in large, single slip steps seen in Figure 55 and Figure 58 with higher yield stress when compared to the unirradiated condition. This result correlates well with other mechanical testing on irradiated materials and can be attributed to typical irradiation hardening behavior [115,132,133]. Upon closer inspection of the irradiated 7µm tensile bars, two distinct behaviors were revealed. For four of the seven tensile bars we observe larger strain-to-failure and lower yield strengths while the remaining samples exhibited smaller strain-to-failures, higher yield strengths, and significant strain bursts compared to each other. This can again be explained through the grain size variance in Zircaloy-4. The former of the two behaviors could correlate to the tensile bars which had a finer grain size and were able to serve as effective sinks for radiation defects. The latter of the two behaviors would correlate to coarse-grained tensile bars which experience a loss of plasticity in the grain interior and subsequent large slip steps and strain bursts. In the irradiated material, the presence of a large density of dislocation loops impedes dislocation motion, causing dislocation pileup, and initiating large slip events that presented strain bursts in the irradiated material. In contrast, in the unirradiated condition, plastic deformation occurs through multiple slip steps resulting in a comparatively gradual decrease in load.

The 80μm tensile geometry stress-strain curves show a combination of ductile and brittle deformation with small amounts of necking before failure. The fracture surface shown in Figure 58 shows the mixed ductile-brittle fracture mode. The 80μm geometry's behavior correlates well with bulk scale ATT tests done by Kamerman *et al*. on the same batch of Zircaloy-4 as shown in Figure 7. However, the yield strength of both the 80μm geometry and bulk testing in Kamerman *et al*. are low when compared to estimates in other studies. With ATT testing of differing geometries, Chu *et al.* measures Zircaloy-4 yield strength to be around 750MPa and Bang *et al.* reported a value of around 550MPa, both with similar strain-to-failure values [134,135]. This difference in measured yield can be attributed to the differing strain rates of testing and processing conditions of the Zircaloy-4 tubes such as the cold work percentage. Another discrepancy in the meso-scale testing from the bulk scale testing done by Kamerman *et al.* is the lower flow stress measured on the meso-scale as evidenced by the lower UTS [115]. This low flow stress can be attributed to the differing strain rates used for testing, a lack of statistics on the bulk scale, and a dramatic decrease in grains sampled on the meso-scale. In particular, the low strain rate used in this testing is commonly correlated with low flow stresses [136].

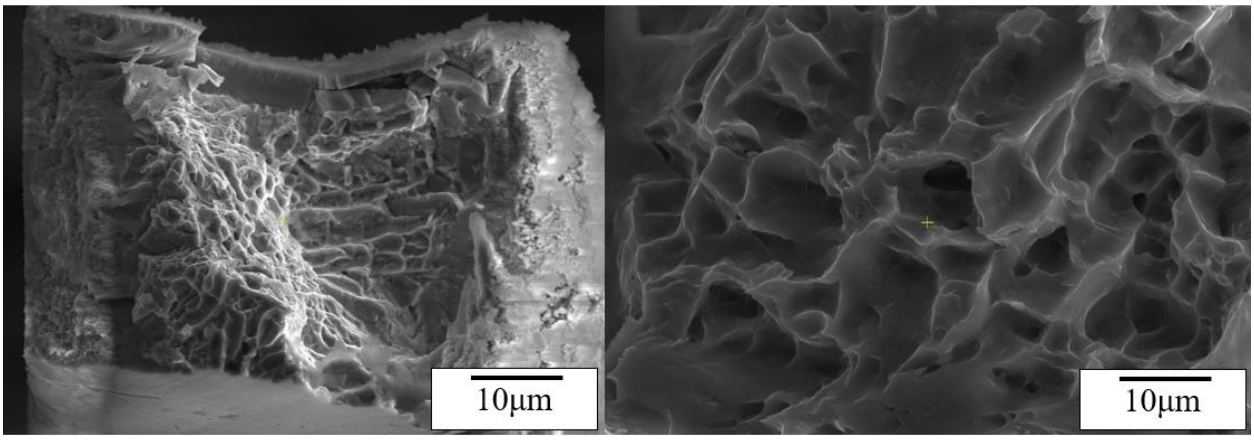

Figure 57. Mesoscale tensile test fracture surfaces showing mixed brittle-ductile failure

Lattice and slip system orientations also appear to affect the results. Figure 58(a) shows deformation occurring along a nearly ideal plane at 45° from the tension axis, while Figure 58(b) shows deformation occurring at many angles including normal to the tension axis where very little resolved shear stress is developed. Variations in slip system orientation could develop differences in yield and plastic behavior which is especially significant where one grain orientation provides a majority of the gauge section, such as small gauge sections. This effect is averaged over many grain orientations in larger gauge sections such as the 80μm gauge sections, and a more consistent yield is observed for the unirradiated 80μm samples compared to the 7μm and 2μm samples in Figure 55.

Comparing all the data, a distinct trend in the yield strength of each stress-strain curve when plotted against tensile bar size shown in Figure 59 is found. There is a clear decrease in the yield strength and UTS of the Zircaloy-4 when tested on a larger length scale which can be attributed to a mix of mechanisms. Dislocation motion governs plasticity in most materials and a reduction in volume of tested material decreases the number of potential sites for impeded dislocation motion and the accumulation of stress concentrators. Defect-free nanometer scale

structures exhibit near theoretical strengths due to the lack of these stress concentrators and the additional energy needed to nucleate dislocations to propagate through the material [75]. Primarily for this study, the amount of grain boundaries sampled changes drastically for the 2μm, 7μm, and 80μm tensile bars. The increase in stress concentrators at a larger length scale contributes heavily to the decrease in observed material strength. These results correlate well with the model proposed by Hosemann *et al.* on the yield strength correlation with length scale [33,75]. The strain-to-fracture found for each length scale was consistent with that of bulk scale testing but decreased significantly for the 7μm irradiated condition. This trend of a decreasing strain-to-failure further continues with irradiation on the bulk scale as shown by Kamerman et al. [115]. If the only difference between the length scales tested is the amount of grains sampled, this difference in strains suggests that the mechanisms which cause losses in ductility due to radiation damage are heavily influenced by grain boundaries [137].

While not expected to affect the mechanical data of the meso-scale testing significantly, the effects of some factors inherent to the femtosecond laser process have not been studied in depth. These factors primarily include the redeposition of ablation nanoparticles on the surface of the tensile bars, small ripples formed on the lasered surface, and the development of a small HAZ due to the laser interaction. It is also noted that the ratios of the gauge width to gauge thickness and gauge length to gauge thickness are slightly different between the micro- and meso-scale tensile bars. While this slightly affects the stress state of each tensile bar, it is not expected to greatly affect mechanical results [138].

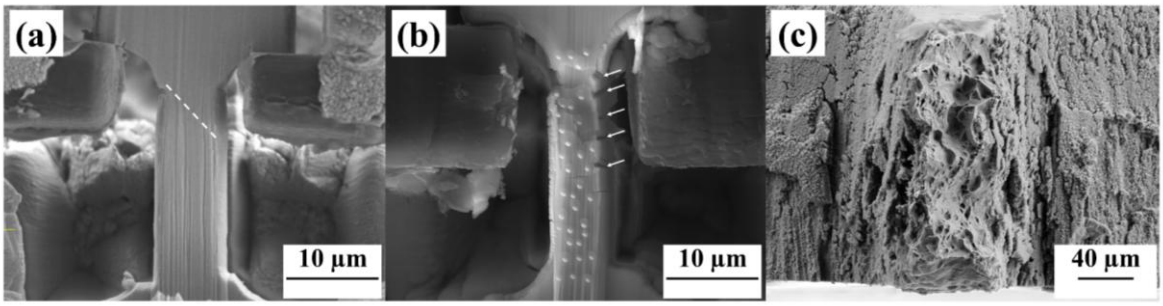

Figure 58. SEM images of tensile fracture. (a) Image of irradiated 7μm tensile bar showing large slip step. (b) Image of unirradiated 7 μm tensile bar showing multiple crack nucleation preferentially at surface. Dots indicate markings intended for Direct Image Correlation

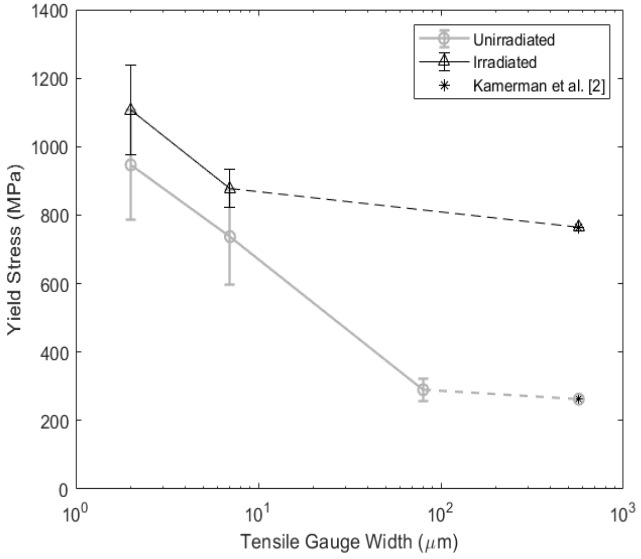

Figure 59. Final yield stress values for both control and irradiated Zircaloy-4 plotted against length scale tested with error bars showing standard deviations

5.5 Conclusions

Tensile testing was conducted on three different length scales and the mechanical properties were extracted. Irradiated and unirradiated micro-scale tensile specimens were compared to further observe length scale dependency on mechanical properties. Key findings of this study were:

- The yield strength of Zircaloy-4 differed when measured on differing length scales and showed a sharply decreasing trend from micro- to meso-scale. This decrease plateaued with meso-scale testing showing promise in obtaining bulk-like property values with a minimal sample volume. This would require understanding the microstructure of the material and manufacturing tensile bars that contain enough strength determining features to measure bulk properties.

- Irradiated Zircaloy-4 when tensile tested on the micro-scale shows similar trends to that of bulk-scale testing with an increase in yield strength and UTS following irradiation. However for testing the smallest, 2µm gauge width, tensile bars, no loss in ductility was found with a similar hardening effect.

The use of fs-laser machining of meso-scale tensile specimens serves as a unique middle ground to sampling bulk-like tensile properties while minimizing the volume of material needed for testing. By reducing the volume of radioactive material needed for testing, this would limit radiation worker dosages and facilitate sample handling. These findings are useful for the planning of post-irradiation experiments (PIE) which could sample bulk-scale properties without the need for large and costly hot-cell facilities.

For this dissertation, this study helps in identifying expected length scale trends in extrapolating micro-scale results to the bulk-scale as the same conclusions made here can be applied to F82H. As expected, with a decreasing length scale, a strengthening effect is seen as predicted by theory. Properties like UTS and yield strength in Zry-4 see a measured strength increase of 2-3x when comparing the micro-scale and the bulk-scale results. While this phenomenon obscures direct comparisons made between SSMT and commercial scale reactor components, it helps inform the expected trends when comparing the length scales. Since SSMT is one of the only techniques which can study the mechanical properties of radioactive or toxic materials, this information is crucial for informing materials decisions. Furthermore, this study highlights the fact that comparisons between conditions within the same length scale are useful. Comparison between the unirradiated and irradiated of Zry-4 yield the same trend within the same length scale showing the promise of identifying material changes due to different treatments. With this, it is expected that similar trends will arise in F82H however the magnitude and defect mechanisms responsible will need to be investigated further.

Chapter 6

The Influence Carbides on the Internal Friction of F82H

6.1 Introduction

Chapter 5 focused on correlations between small scale mechanical testing and macro-scale testing. The conclusions made help in understanding length scale effects on material property and give a more comprehensive understanding of material anisotropy. These findings can now be applied to a micro-scale testing on F82H to help in understanding the effect of carbides on the material and the different martensitic features they nucleate on.

Understanding the mechanical properties of the F82H martensitic structure and their changes while exposed to the harsh environment of a fusion reactor is crucial [29,60,139]. The repercussions of carbide precipitates on the different features of the martensitic microstructure has not been researched in depth and necessitates further study using resolved techniques. SSMT has been an integral part of nuclear materials since Hosemann et al. demonstrated that it could provide useful information on ion beam irradiated materials [140]. Using SSMT allows for precise features in the martensitic microstructure to be studied in depth.

Internal friction and damping measurements were popular topics championed in the 1960s and 70s by scientists like Snoek, Granato, Lücke, Kê, and Köster who found interesting frequency and temperature dependent amplitude peaks in the torsion of metal wires [86,141–144]. These peaks could be correlated directly to the movement of specific defects in the material. In the absence of advanced microscopy and other spectroscopy techniques, this was one of the few ways to gain an intricate view into the interactions of dislocations and interstitials with a relatively simple experimental setup [85,86,88,89]. While research in the area has steadily declined with more resolved characterization methods, internal friction still remains a foundational niche in studying defects. Most commonly, internal friction peaks are used to estimate carbon interstitial content in steels [89,145].

Using the formative work on internal friction as a basis, micromechanical spectroscopy (μMS) was developed in Alfreider et al. to probe changes in internal friction in cantilevers. This novel SSMT technique is used to measure resonance peak changes on focused ion beam (FIB) fabricated microscale cantilevers [83,146]. For this, a microcantilever is loaded into a picoindenter system with dynamic measurement capabilities and brought into contact with the indenter tip. Following contact, a frequency scan is used to probe the resonance peak whose shape and magnitude can be used to estimate damping, elastic properties, and internal friction. A key advantage to this technique is that it nondestructively gives quantitative values for damping which can be correlated to sources for internal friction. Due to the scale and the nondestructive nature of

this testing, the same cantilever can be tested before and after heat treatments to see how damped oscillations evolve within cantilevers encompassing different microstructural features. The combination of targeted microstructural examination and quantitative damping assessment make μMS a powerful technique for the fundamental study of defects.

Damping and internal friction are intrinsic material properties that describe the irreversible dissipation of mechanical energy, typically as heat, when a material is subjected to cyclic loading or deformation. Internal friction arises from a variety of microstructural mechanisms including dislocation movement, grain boundary sliding, and the reorientation of point defects or secondary phases that resist strain and convert vibrational energy into thermal energy. The activation of these mechanisms and the magnitude of their effect are strongly dependent on temperature, frequency, and material composition. In metals, dislocation damping dominates at moderate temperatures, while at higher temperatures, diffusion-assisted processes such as grain boundary relaxation become significant.

A schematic of a system with a damped oscillation is shown in Figure 60. In a dynamic vibration-based mechanical tests, the amplitude–frequency curve reveals how strongly a sample responds when it is excited across a range of frequencies. For a material with small damping, the resonance peak appears tall, narrow, and sharp. This occurs because very little vibrational energy is dissipated in every vibration cycle, allowing oscillations to measure a high amplitude as the driving frequency approaches a natural resonance frequency. On the other hand, a material with heavy damping exhibits a broad, flattened resonance peak with a reduced measured amplitude at the resonance frequency. Heavy damping indicates that the material dissipates energy efficiently, oscillations cannot grow to large amounts, even near resonance.

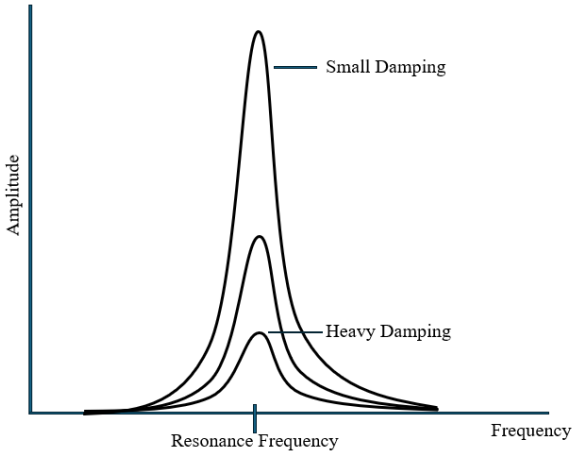

Figure 60. Damped Oscillation Schematic

The implications of damping and internal friction are crucial for structural applications where fatigue resistance, vibration mitigation, and shock absorption determine long-term performance and safety. High internal friction can be beneficial in reducing resonant vibrations and attenuating dynamic stresses, thus extending fatigue life in components subjected to cyclic loading in high wear applications. In high damping materials, mechanical energy can be dissipated

through heat or phonons, reducing stress amplitudes when dynamic forces are applied. Understanding and controlling internal friction mechanisms enables the of design materials that can endure the dynamic stress environments inherent to structural systems.

In this study, μMS is performed on 8 microcantilevers fabricated of fully heat treated (quenched and tempered) F82H made of differing grain structures. This was done to reveal the complex interactions between defects like grain boundaries, dislocations and carbides on energy dissipation mechanisms in F82H martensite.

6.2 Methods

A piece of F82H was quenched from a holding temperature of 1040°C at 1h in a vacuum furnace using water. This piece was polished using 2500 grit SiC sandpaper into a wedge shape to prepare for cantilever fabrication. A femtosecond laser system at the University of California, Berkeley was used to mill into the edge of the wedge the rough shape of the cantilevers. An average laser power of 0.09W, repetition rate of 20kHz, wavelength of 1040nm, pulse duration of 332fs, scan speed of 10μm/s, and a focused spot size of ~2μm using a 50x Mitutoyo optic were used during the lasering. The lasered cantilevers were then milled using a FIB operating at 30kV and 1nA to clean the cantilevers into their final shape. The laser-material interaction is not expected to affect mechanical data through excess heat deposition due to the short femtosecond pulse duration [99,124,147]. The approximate dimensions of each cantilever were 3x3x15μm and were SEM imaged for accurate length L, width W, and height H measurements for all calculations. SEM images of a cantilever following fs-laser machining and following FIB cleaning are shown in Figure 61

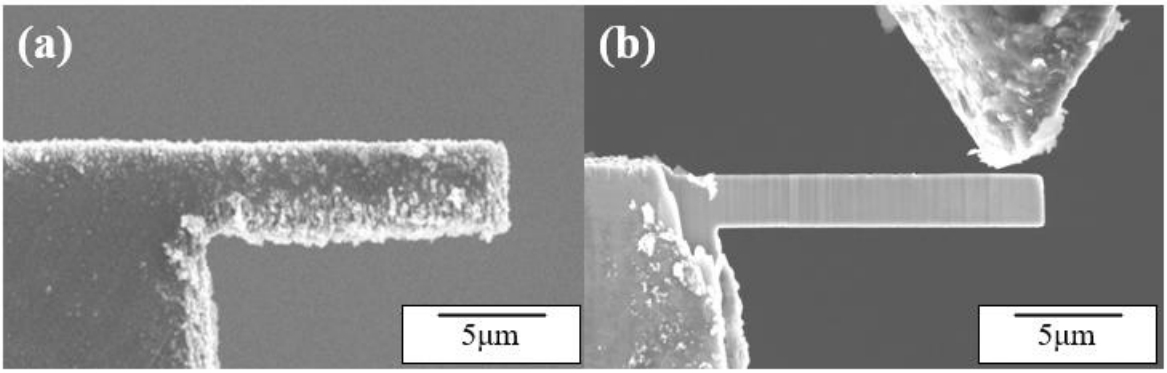

Figure 61. a) Cantilever following fs-laser machining. b) Same cantilever cleaned from FIB before uMS testing

Prior to μMS testing and heat treatment, the grain orientations of each cantilever were imaged using electron backscatter diffraction (EBSD) at a voltage of 30kV and with a step size of 0.1μm. Subsequent analyses were done using the Oxford AZtecCrystal software.

To perform the μMS experiment, the cantilevers were placed into a Hysitron PI-88 picoindenter system with nano-dynamic mechanical analysis (nanoDMA) capabilities. The system was equipped with a 1μm diamond wedge tip and was inserted in an SEM. The wedge tip was

brought in contact with the cantilever using a 300μN contact force where a frequency sweep test ranging from 200 to 300Hz using a 3μN load amplitude was used to probe the resonance peak. Three frequency sweeps were performed each at two different points along the length of the cantilever for better statistics. The resonance peak was captured as a function of dynamic compliance and frequency.

Following μMS, the cantilevers were tempered at 750°C for 1h in a vacuum furnace. The full temperature history of the cantilevers is shown in Figure 39 and repeated in Figure 62. The same μMS procedure was performed following tempering on the cantilevers to probe the resonance peak changes. The forces used in both μMS experiments were small enough to only elastically load the cantilever and no evidence of plastic deformation was found after testing. More information about the exact μMS procedure and data analysis can be found in the seminal work on the subject by Alfreider et al [83,146].

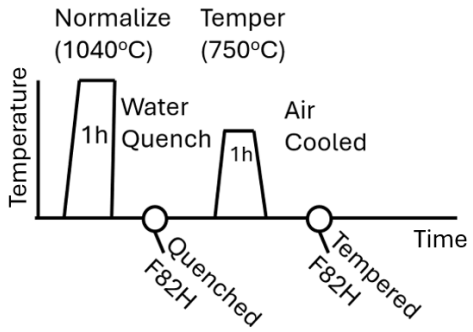

Figure 62. Heat treatments targeted for F82H quenched and tempered conditions.

6.3 Results

Figure 63 and Figure 64 show all the tested cantilevers with their associated IPF-Z and IPF-X EBSD maps overlaid on SEM images. Usage of both IPF maps is important since one IPF map does not give the full picture of the crystal orientation. Since IPF maps only correlate the direction of the defined axes with the direction of the crystal, one map is not enough to accurately know a crystals orientation since the crystal can be rotated any direction within the plane.

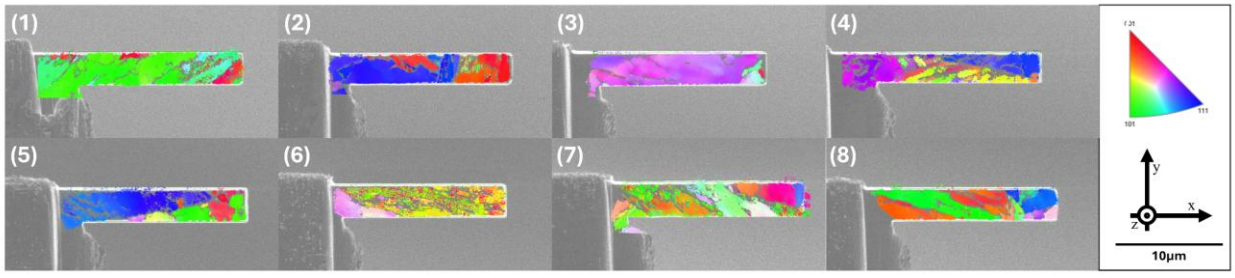

Figure 63. All numbered F82H cantilevers (before tempering) with EBSD IPF-Z map overlaid, normal directions and scale bar

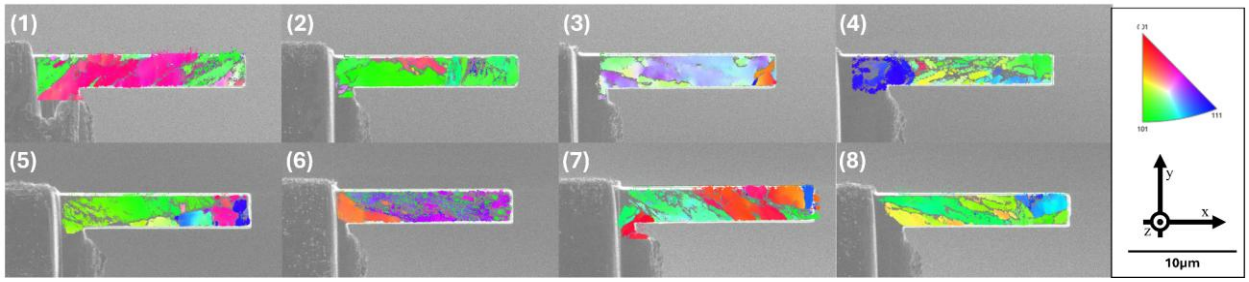

Figure 64. All numbered F82H cantilevers (before tempering) with EBSD IPF-X map overlaid, normal directions and scale bar

µMS was performed on all 8 cantilevers in their quenched state and tempered state. Figure 65 shows tempered Cantilever 6 during testing with the tip in contact with the cantilever. Additionally, a simple finite element model of a beam bending is shown to highlight the tension and compression stress distribution within the cantilever. A video of the µMS experiment was recorded and rapid oscillations resulting from resonance can be seen during the experiment.

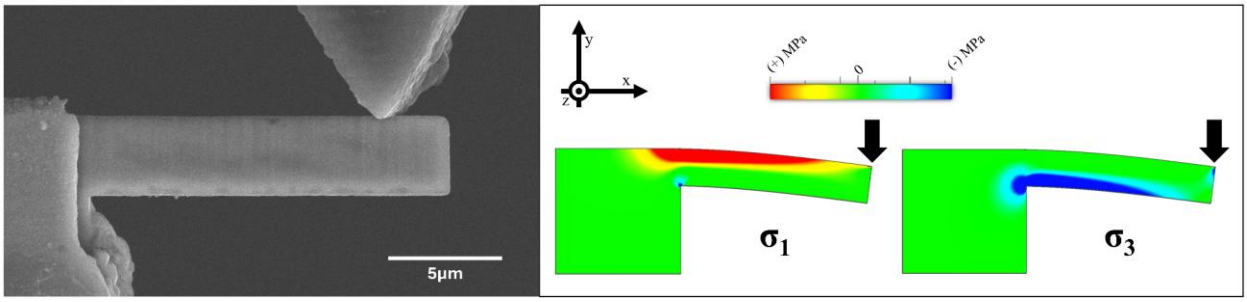

Figure 65. (left) Cantilever 6 during µMS testing with wedge tip in contact. (right) FEM model showing first (tension) and third (compression) principal stresses on bent cantilever.

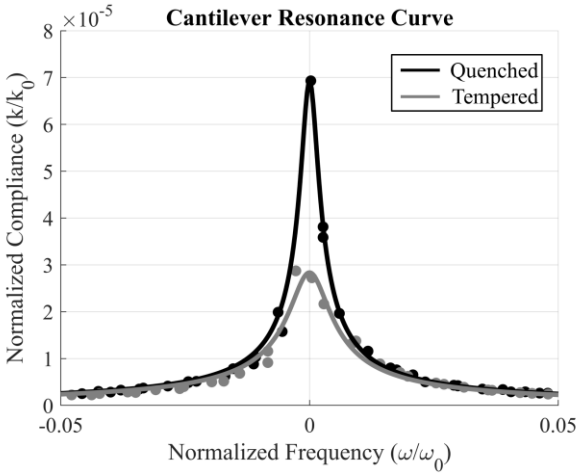

Figure 66. Normalized compliance vs normalized frequency measured from the µMS experiment on Cantilever 4 showing measured resonance peak. Analyzed trendline shown with raw data points.

The µMS experiment measured the dynamic compliance of the indenter tip as a function of the frequency. Figure 66 shows the peak of the compliance measurement giving the resonance

curve from Cantilever 4 in both the quenched and tempered state. To eliminate effects from minor differences in cantilever geometry, the frequency has been normalized by the resonance frequency and the compliance has been normalized by the total compliance. The experimental system can be simplified to a single degree of freedom (SDOF) oscillator model. The SDOF model is composed of stiffness contributions from the indenter, tip contact, and cantilever plus damping contributions from the indenter and cantilever. In this model, the total damping and stiffness can be extracted from the compliance and frequency data using accurate fitting to the underlying SDOF model using the lmfit Python 3.8 package. These extracted values can be then used to calculate Q^{-1}. Additionally basic Euler-Bernoulli theory of a simple loaded beam can be used to estimate the elastic modulus of each cantilever. A more detailed explanation of this SDOF model and the mathematical framework can be found in Alfreider et al [83,146]. The calculated values for elastic modulus and Q^{-1} are tabulated in Table 3.

Cantilever	Elastic Modulus (GPa)		Q^{-1}	
	Quenched	Tempered	Quenched	Tempered
1	129.20	149.44	4.03×10^{-3}	8.81×10^{-3}
2	154.32	161.56	3.84×10^{-3}	10.09×10^{-3}
3	141.80	160.24	3.71×10^{-3}	7.58×10^{-3}
4	160.23	156.69	4.71×10^{-3}	6.14×10^{-3}
5	142.13	154.57	3.24×10^{-3}	6.51×10^{-3}
6	151.22	158.00	3.89×10^{-3}	6.62×10^{-3}
7	147.86	157.08	3.71×10^{-3}	7.73×10^{-3}
8	144.44	149.18	3.21×10^{-3}	7.28×10^{-3}
Average	146.40	155.84	3.79×10^{-3}	7.60×10^{-3}

Table 3. Calculated elastic modulus and Q-1 for each tested cantilever measured from the uMS experiment

In order to see if the tempering had any inhomogeneous effects on the composition of the cantilevers, a energy dispersive spectroscopy (EDS) scan was taken of Cantilever 4. The result of this scan is shown in Figure 68. It can be seen here that no specific elemental desegregation occurred on the cantilevers. A small Cr, Mn, and O rich cluster was found on the bottom of the cantilever but this is attributed to femtosecond laser debris which is not expected to effect results. In particular, a concern was the potential segregation of carbides to a free surfaces like the edges of the cantilever but the EDS scan shows that this did not occur in measurable levels. Furthermore EBSD revealed a fully BCC microstructure following tempering shown in Figure 67.

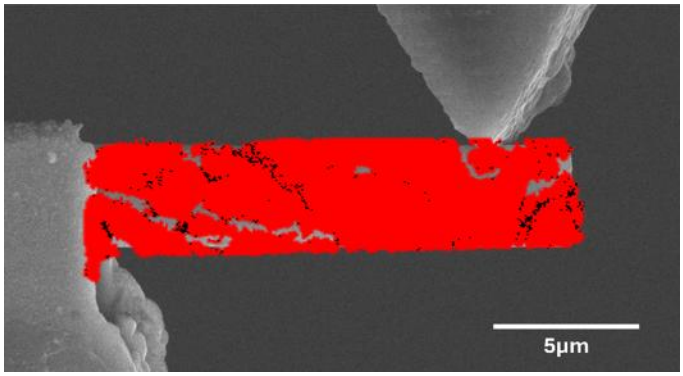

Figure 67. Cantilever 3 tempered EBSD phase map with red denoting indexing of the BCC crystal structure

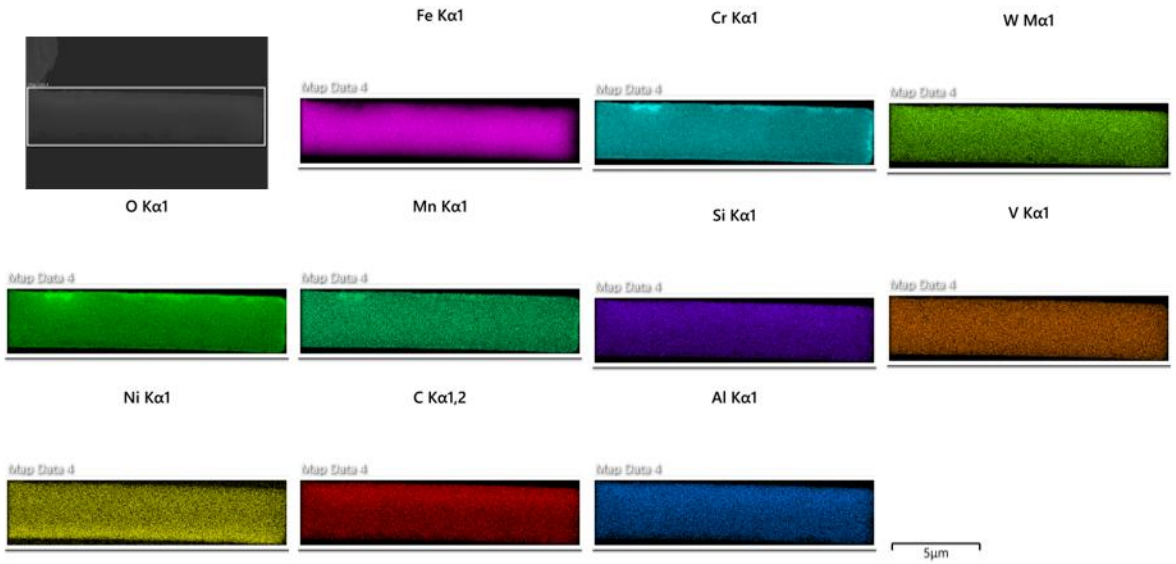

Figure 68. Energy dispersive spectroscopy (EDS) scan of Cantilever 4 following tempering showing no elemental segregation.

6.4 Discussion

Damping and Internal Friction

Across all cantilevers tested, the damping increased following tempering with an average of $Q^{-1}_{Quenched}=3.79x10^{-3}$ to $Q^{-1}_{Tempered}=7.60x10^{-3}$. While it is straightforward to extract empirical damping values from the resonance peak through classical beam theory, analysis of the origin of changes in damping is more complex. Damping describes a material's ability to dissipate mechanical energy typically through heat or other forms of energy and can be classified into two broad groups, internal sources and external sources. Damping driven by internal sources is desired as they describe the material's microstructural features which influence damping. External sources of damping are sources other than the material.

External sources for damping were minimized within the experimental setup and were not assumed to significantly influence the measured data. Air damping was mitigated through conducting the experiment in-situ in a SEM with a high vacuum of 10^{-5}-10^{-6} mbar also minimizing the effects of oxidation. Also, sources of damping related to mechanical coupling were eliminated through making the cantilever and base out of the same material. Other sources of external damping like electromagnetic damping and fluidic damping do not apply to our system.

Internal sources for damping are complex and can be explained through the relaxation of certain defects within the material. Broadly, the sources of internal damping can be separated by their defect dimension and the mechanism which produces damping effects.

Point defect based damping mechanisms are suspected to be influential when comparing the differences in damping of the quenched and tempered state. Snoek relaxation describes the anelastic relaxation of interstitial atoms when subjected to an oscillating stress. Interstitials like carbon sitting in the BCC octahedral sites will reorder positions, jumping between point defects creating a damping effect [85,86]. Quenched martensite holds a supersaturated amount of carbon in interstitial sites within the ferrite lattice due to the forced diffusionless martensitic transformation. Upon tempering, diffusion allows for this excess supersaturated carbon to form carbide precipitates typically with Cr [148] which should lead to a reduced damping. The increased interstitial carbon content of the quenched state predicts that Snoek relaxation should have a strong effect for the quenched state. In fact, the differences in Q^{-1} of cantilevers within the quenched condition ($Q^{-1}_{Quenched}$) can be clarified using the Snoek relaxation mechanism. Supersaturated carbon preferentially sits in BCC octahedral sites, this creates a maximum damping for normal stresses oriented parallel to the <100> direction and a minimum for the <111> direction [145,149]. Among the quenched cantilevers, Cantilevers 1 and 6 exhibits the high $Q^{-1}_{Quenched}$ and can be attributed to its structure predominantly composed of a grain whose (100) plane is oriented normal to the bending direction, maximizing Snoek relaxation. Other cantilevers which exhibit low values for $Q^{-1}_{Quenched}$ like Cantilevers 5 and 8 have large grains oriented with the (101) plane parallel to the cantilever, showing reduced effects from this Snoek relaxation. Of course, the fact that different cantilevers have different lath structures leads to a more complicated reality, the trend seems to indicate the effects of orientation on the Snoek relaxation. However, this mechanism cannot comprehensively explain the measured increase in Q^{-1} of the cantilevers following tempering ($Q^{-1}_{Tempered}$). Due to the redistribution of carbon during tempering and the reduction in interstitial carbon content, Snoek relaxation predicts that $Q^{-1}_{Tempered} < Q^{-1}_{Quenched}$. Figure 4 shows a consistent trend of an increase in Q^{-1} from the quenched to the tempered state meaning that another mechanism has a greater influence.

Dislocation based damping mechanisms where the movement and nucleation of dislocations can create energy dissipation needs to be considered. One primary theory giving rise to Bordoni internal friction peaks is the formation of double kink bands between two sets of dislocations. This phenomena is prevalent in materials with high Peierls barrier lattices like BCC or BCT martensite. Due to the high Peierls barrier, two parallel dislocation lines can form kinks which inelastically move apart when subject to an external stress. Another theory, proposed by Granato and Lücke (GL) holds that dislocations act as elastically vibrating strings, pinned by lattice defects. At small stresses and before plastic deformation, dislocation lines can bow outwards until a critical breakaway stress is reached where the dislocation separates from the pinning defect. The phase lag between the oscillating stress and cantilever displacement in addition to the elastic collapse of dislocation lines after bowing create a damping effect. The GL model is not expected to be as influential as the kink pair model due to the high Peierls dislocation barrier energy of BCC lattices. However in both models, the reduction in dislocation density following tempering predicts that dislocation damping would decrease however this is not found.

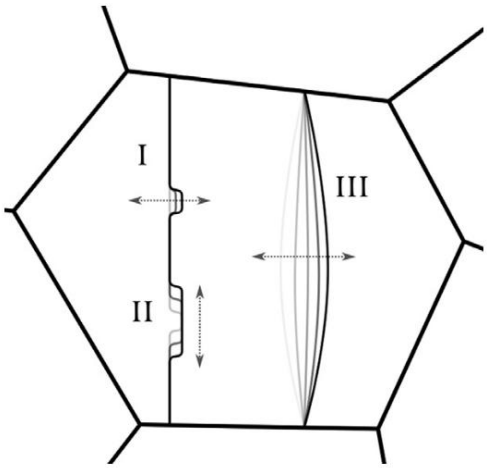

Figure 69. Visual representation of dislocation damping mechanisms showing kink pairs (I, II) and Granato Lucke based vibration string dislocations pinned by grain boundaries (III) [84].

In the GL model, a distinction is made between weak and strong pinning defects. Interstitials only weakly pin dislocation lines while more incoherent defects like precipitates can strongly pin defects. This changes the vibrating string mechanism to where an increase in weak pinning defects inhibits dislocation motion, decreasing damping while an increase in strong pinning defects creates more vibrating dislocation strings, increasing damping. This mechanism is commonly used to explain the damping during precipitate evolution in fcc Al alloys [150]. It is suspected that interaction of strong pinning precipitates nucleated from tempering and dislocations contribute strongly to the increase in damping. Cantilever 2 bolsters this theory since it is composed of a grain whose (110) close packed plane is oriented parallel to the direction of tension and compression. Cantilever 2 also experiences the highest increase in damping capacity following tempering, hinting at dislocation motion being influential. Cantilever 1 which also experiences a high increase in damping capacity and encapsulates a grain with a (100) orientation parallel to the direction of tension and compression favorable to dislocation motion.

Grain boundary based damping mechanisms are not thought to be a significant influence. This is due to the fact that many of the mechanisms which cause grain boundary movement only activate at high temperatures or stresses not present within this experiment. In fact, this can be seen when comparing the grain misorientation angles and the damping between cantilevers within heat conditions, which yields no significant trend. Interestingly, this can help explain the weak increase in damping following tempering in Cantilever 4. In F82H, carbides are known to precipitate to grain boundaries with preference for incoherent high angle grain boundaries (HAGBs) in martensite [71,72]. It is suspected that Cantilever 4 which has the highest density of HAGBs was able to precipitate a large portion of the carbides to these interfaces, away from the grain interior. In effect, this is able to precipitate carbides away from areas where they could pin dislocations to increase damping, constraining them to immobile grain boundaries which only weakly contribute to damping. This mechanism also comes to the conclusion that precipitates nucleated in the grain interior contribute more to damping which can be seen in Cantilever 1 and Cantilever 2 which have the highest increases in damping and also the large single grains.

Another mechanism considered is described by Schoek where the interface between precipitates and the matrix material relaxes under stress causing a damping effect [151]. This effect increases with greater incoherence of the precipitate and matrix. It is expected that this mechanism contributes to the results however it is hard to deconvolute this effect with the GL dislocation pinning damping mechanism since both come to the same conclusion. Further detailed study would be needed to disentangle which mechanism has a stronger effect. However, the general trend of higher increases in damping in cantilevers whose grains are oriented with close packed planes parallel to tension and compression suggests that dislocation motion plays a significant role.

In summary, the measured data from the μMS experiment found that $Q^{-1}_{Tempered} > Q^{-1}_{Quenched}$. An analysis of damping mechanisms was able to suggest that this damping increase was likely due to GL precipitate pinning mechanism and the Schoek precipitate interface mechanism. While more detailed TEM investigation would be needed to make definitive conclusions, current literature suggests similar results. Li et al. found that in high alloyed martensite, three internal friction temperature dependent peaks form from carbon-dislocation, carbide, and carbide-dislocation interactions, with the latter being the most prominent [152]. Kim et al. correlates this trend by finding that the internal friction of ferrite is greater than that of martensite [153].

Elastic Modulus

F82H tested in a bulk form typically exhibits a room temperature elastic modulus of 218.8GPa [154]. The elastic modulus measured during this experiment on average was 146.40GPa in the quenched state and 155.84GPa in the tempered state, showing a 40.4% discrepancy from the bulk literature value. Elastic anisotropy in bcc martensite is expected to contribute to differences between testing across different crystallographic grain orientations. Li et al. reports the single crystal elastic constants of F82H which can be extrapolated to find an estimated room temperature C_{11}, C_{12}, and C_{44} to be 187GPa, 133GPa and 126GPa respectively [155]. Using this, the predicted variation in elastic modulus should only vary from 76.44 GPa when stressed in the <100> direction and 295.74GPa when stressed in the <111> direction [156,157]. This crystal elastic anisotropy appears to heavily affect the measured elastic modulus and helps explain trends in the data. Using the euler angles of the individual grains extracted from EBSD a predicted elastic modulus can be calculated for each cantilever [158]. The equation used is:

$$\frac{1}{E_{uvw}} = \frac{c_{11}+c_{12}}{(c_{11}-c_{12})(c_{11}+2c_{12})} - 2\left[\frac{1}{c_{11}-c_{12}} - \frac{1}{2c_{44}}\right](u^2v^2 + v^2w^2 + w^2u^2)$$

Here, u,v, and w represent the direction cosines of each of the Euler angles and c represents the single crystal elastic constants from theory. Using this methodology, the experimental data aligns well with theory. Table 4 calculates the expected elastic modulus values for cantilevers with large grains which can be approximated using this approach.

Cantilever	Euler Angle of Largest Grain			Theoretical Elastic Modulus	Measured Elastic Modulus	
	φ_1	φ_2	φ_3	Tempered	Quenched	Tempered
1	201.28	39.52	86.5	96.908	129.20	149.44
2	59.33	47.23	41.39	163.801	154.32	161.56
3	285.65	32.01	54.63	160.772	141.80	160.24
4		No Large Grain		-	160.23	156.69
5	127.31	34.5	74.82	190.084	142.13	154.57
6	1.86	47.65	51.64	157.832	151.22	158.00
7		No Large Grain		-	147.86	157.08
8		No Large Grain		-	144.44	149.18
Average				153.87	146.40	155.84

Table 4. Theoretical values for elastic modulus compared with measured elastic modulus

While these values differ slightly from the experimental mechanical data in some cantilevers, these small differences can be attributed to influences from other grains within the cantilever aside from the largest grain. In addition, uncertainties in machine compliance and stiffnesses of the picoindenter setup, while mitigated, can contribute to discrepancies in data.

A general increasing trend in elastic modulus can be found following tempering the quenched F82H similar to other studies [159]. On average the elastic modulus of the cantilevers increased by 6.4% following tempering. This is expected as the dislocation density, interstitial carbon concentration, and internal stresses are expected to decrease as a result of tempering, contributing to an increase in elastic modulus. Cantilevers 1, 3, and 5 exhibited the largest increase in elastic modulus following tempering and also encapsulate large grains within its structure. While the cantilevers with finer grain structures and greater degrees of HAGBs like Cantilevers 4, 6, and 8 demonstrated the lowest gains in elastic modulus. It is suspected that carbide precipitates at the HAGBs increase the incoherent grain boundary area, causing a less pronounced increase in elastic modulus. In addition to this, the elastic modulus of ferrite is slightly higher than that of martensite contributing to the observed increase [156].

6.5 Conclusions

In summary, 8 micro-cantilevers of F82H were tested using the novel μMS technique to probe changes in carbide evolution between quenched and tempered martensite. Using the resonance peak of the cantilevers measured by a picoindenter setup, quantitative values for damping and elastic modulus were extracted. The damping of the F82H increased by a factor of 2 following tempering and is primarily thought to be a result of the nucleation of carbides strongly pinning dislocation lines. The grain structure of the individual cantilevers contributed heavily to the measured differences in damping, with grains oriented with CPPs in line with applied stresses experiencing the largest increases in damping. The elastic modulus of F82H increased by 6.4% following tempering with greater increases being recorded for larger grained samples. A graphical summary is shown in Table 5 and reviews all mechanisms and expected results.

Intrinsic Damping Mechanism	Defect Responsible	Origin of Damping Explanation	Expected Damping Contribution – From Mechanism		Expected Damping Change from Tempering the Quenched Martensite - From Mechanism	Experimental Measurement – Tempering the Quenched Martensite	Suspected Damping Contribution
			Quenched	*Tempered*			
Snoek Relaxation	Point Defects – Interstitials	Interstitial positional site reordering, "jumping" between point defects	High interstitial concentration → **High Damping**	Low interstitial concentration → **Low Damping**	Decrease in interstitial carbon content → **Decrease in damping**	**Increase in Damping** $Q^{-1}_{Quenched}=3.79\times10^{-3}$ → $Q^{-1}_{Tempered}=7.60\times10^{-3}$	**Low Influence**
Dislocation Damping	Dislocations	Granato Lucke – Pinned dislocation lines vibration like strings	Low pinning defect concentration → **Low Damping**	High pinning defect concentration → **High Damping**	Increase in strong pinning defects (precipitates) → **Increase in damping**		**High Influence**
		Double Kink Bands – Two dislocation lines inelastically propagate kinks between lines	High dislocation density → **High Damping**	Low dislocation density → **Low Damping**	Decrease in dislocation density → **Decrease in damping**		**Low Influence**
Grain Boundary Damping	Grain Boundaries	Grain boundaries slide against each other	Grain boundaries immobile at low temperatures → **No Effect**	Grain boundaries immobile at low temperatures → **No Effect**	Grain boundaries immobile at low temperatures → **No Effect**		**No Effect**
Schoek Damping	Precipitates	Incoherent interface between precipitate and lattice relaxation	Low precipitate concentration → **Low Damping**	High precipitate concentration → **High Damping**	Increase in precipitate density → **Increase in Damping**		**Medium Influence**

Table 5. Summary of damping mechanisms and their suspected influence on the damping change from quenched to tempered F82H martensite

Chapter 7

The Influence of Carbides on the Tensile Deformation of F82H

6.1 Introduction

Chapter 6 focused on the effect of carbides on dynamic loading conditions in F82H. In particular, internal friction was investigated and carbide segregation to the different martensitic features played a large role on the dynamic mechanical behavior of F82H. Although dynamic loading conditions provide valuable insight into transient mechanical behavior, static loading conditions are equally important and form the foundation of most mechanical analysis. Therefore, it is equally critical to study the mechanical behavior carbides impart on F82H when subject to static forces.

The mechanical performance of F82H is intrinsically linked to its tempered martensitic microstructure. However the combination of inhomogeneous nucleation of carbide preferentially to certain martensitic morphological features and the effects on the micromechanical behavior has not been studied in depth. Doing this will enable a deeper understanding of the fundamentals of martensitic strengthening from tempering. Microtensile testing is a SSMT technique which destructively probes the mechanical behavior of micron scale volumes of material. Chapter 5 investigated and validated this form of testing on irradiated and unirradiated microtensile bars made from Zry-4. SSMT techniques have been important in fusion and fission materials development due to the volumetric limitations of working with radioactive materials. Beyond this, SSMT provides a unique means to isolate and quantify localized deformation and defect interactions, offering insight into the evolution of mechanical properties under extreme environments.

Microtensile testing has been performed on F82H in the past. Miura et al. tested F82H microtensile bars in the irradiated (He/Fe) and unirradiated state. It was concluded that length scale effects were not prevalent in F82H compared to bulk testing when comparing strength however irradiation hardening was still found. Miura also found that a reduced strain was found on the microscale when testing both unirradiated and irradiated conditions, with most samples failing before a strain of 0.03 [160]. Ando et al. on the other hand did not find this strain reduction effect in F82H microtensile bars and found similar irradiation hardening behavior. An interesting finding of all previous works on microtensile testing on F82H finds that microscale results are similar to that of bulk scale results, conflicting with commonly known length scale trends. While all the previous studies have focused on the irradiation effects on the microtensile behavior of F82H, none have focused on the effects of quenching and tempering. To investigate the effect of carbides at grain boundaries in martensite, SSMT was used to probe specific interfaces within samples of

tempered and quenched F82H. Microtensile testing was performed on quenched and tempered F82H to assess how heat treatment induced microstructural changes and carbide precipitation influences mechanical behavior at small scales. By correlating stress-strain behavior with SEM and EBSD characterization of the tensile bar structure and carbide distribution, the extent that tempering alters yield strength and failure behavior is quantified. These mechanisms provide insight into the deformation mechanisms that control the performance of F82H on the macroscale and offer guidance for optimizing heat treatments to achieve desired mechanical properties in fusion relevant conditions.

6.2 Methods

The sample preparation technique used to prepare the microtensile bars was similar to the microcantilever samples used for the μMS experiment. Two pieces of F82H were sectioned into a thin foil using a Stuers Accutome diamond precision saw. One of the F82H pieces was quenched from a holding temperature of 1040°C at 1h in a vacuum furnace using water to form quenched martensite. The other piece was quenched in the same procedure but was subsequently tempered at 750°C for 1h in the same vacuum furnace to form tempered martensite. During both heat treatments a vacuum pressure of 10^{-5} mbar was used, drastically reducing the effects of oxidation. A history graph of the heat treatments are shown in Figure 39 and repeated in Figure 70. Both foil pieces were polished at a 5° angle to form a razor edge at one side of the foil. The razor edges of both F82H pieces were then machined using a SpectraPhysics SpiritOne femtosecond laser system equipped with a Newport XPS stage to precisely control movement. Using this setup, the rough outlines of microtensile bars were directly machined onto the razor edge of both F82H pieces. The laser was run at an average laser power of 0.09W, a repetition rate of 20kHz, a wavelength of 1040nm, a pulse duration of 332fs, a scan speed of 10μm/s, and a focused spot size of ~2μm using a 50x Mitutoyo optic. Following the laser machining, the microtensile bars were further cleaned using a ThermoFisher Scios2 dual beam SEM/FIB with the Ga ion FIB operating at 30kV and 1nA to clean the microtensile bars to their final shape. It was found that a small inset taper region on the tensile bars greatly promoted uniform tension within the tensile bars. The images during this process are shown in Figure 71 showing the machining process from the as-lasered state to the final FIB cleaned state. This method developed follows the procedure developed in Chapter 4 which produced this streamlined technique while also proving the minimal heat impact of this method.

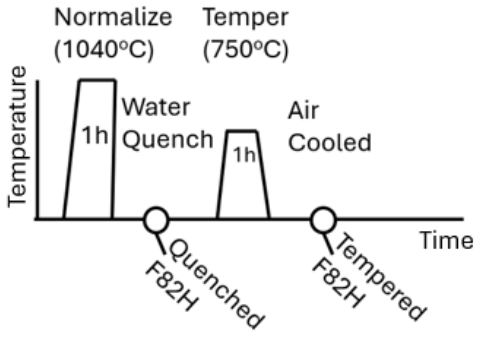

Figure 70. Heat treatment history for the quenched and tempered F82H conditions

Following sample preparation, all tensile bars were imaged using electron backscatter diffraction (EBSD) at a voltage of 30kV and a step size of 0.1µm using an Oxford symmetry s3 detector. The Oxford AztecCrystal software was used for subsequent analyses.

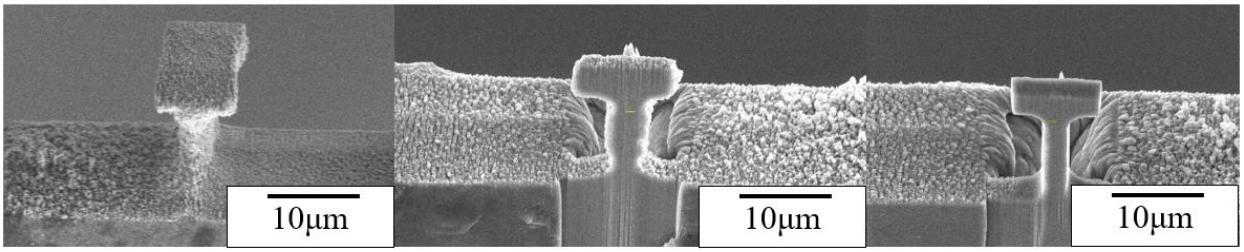

Figure 71. (left) Post fs-laser processed tensile bar, reverse side. (middle) Tensile bar following first FIB cleaning. (right) Tensile bar following final FIB cleaning

A total of 26 tensile bars, 15 quenched and 11 tempered, were fabricated using the joint fs-laser and FIB method highlighting the rapid processing capabilities of this method. The fs-laser process took around 5 mins of laser time for each sample and 30 mins of FIB time, showing a drastic improvement in time from a purely FIB based approach. The final FIB cleaned tensile bars were tested using a Hysitron PI-88 picoindenter system equipped with custom shoulder grippers both pictured in Figure 72. The shoulder grippers were fit around the each tensile bar then pulled at a speed of 5nm/s, approximately a strain rate of 10^{-3}/s. The resulting load-displacement curves obtained from the experiment were correlated to stress-strain measurements using accurate gauge dimension measurement in the SEM.

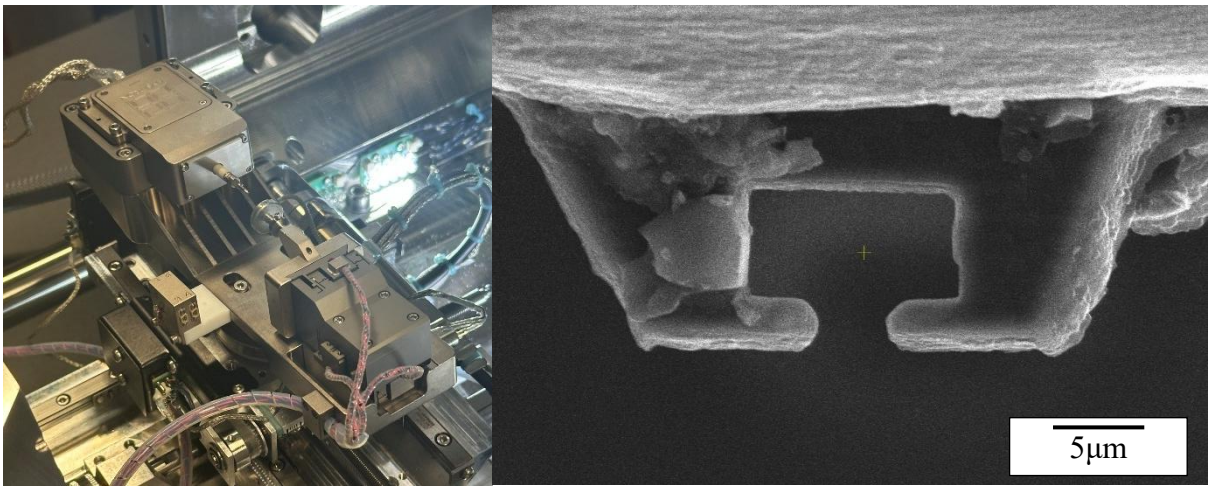

Figure 72. Hysitron PI-88 system being loaded in-situ into SEM with custom machined microtensile shoulder grippers.

6.3 Results

Figure 73 and Figure 74 show all the fabricated tensile bars in both the quenched and tempered condition numbered for later reference. Quenched samples are labelled beginning with

a “Q” and tempered samples are labelled with a “T”. In addition, the EBSD-IPFZ maps are overlaid onto the tested gauge section of each tensile bar. Some tested tensile bars like Q4 and T6 are partially missing EBSD data toward the bottom of the gauge section due to EBSD signal blockage from unmilled pieces of the sample.

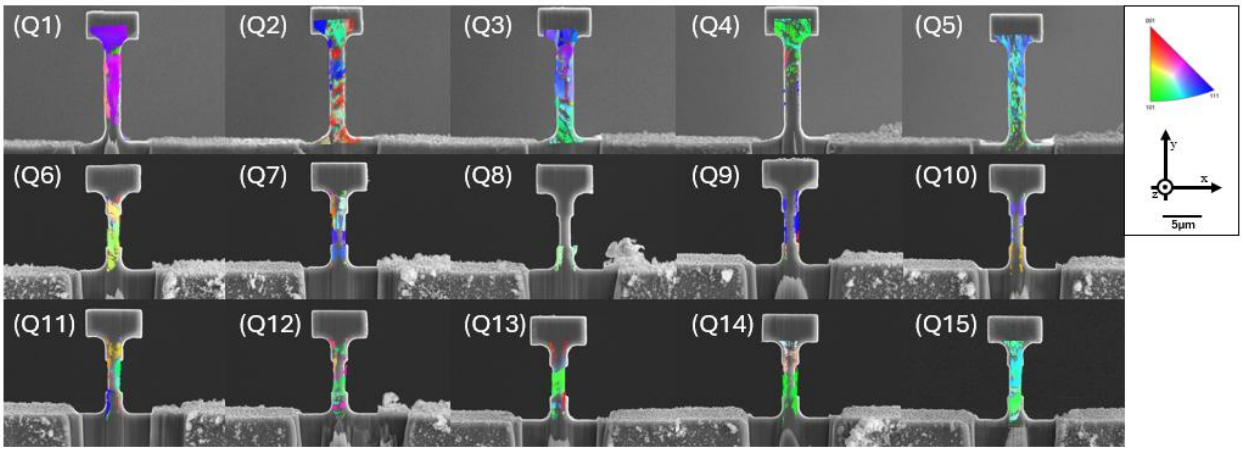

Figure 73. SEM images of all quenched condition microtensile bars with EBSD IPF-Z maps overlaid, normal directions and scale bar.

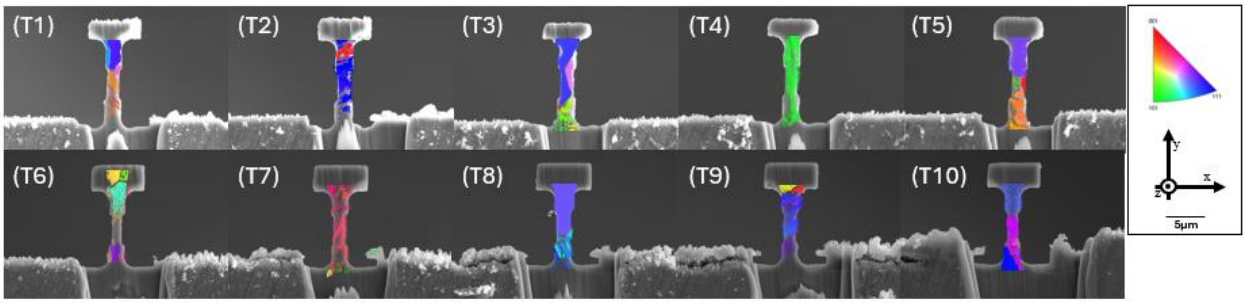

Figure 74. SEM images of all tempered condition microtensile bars with EBSD IPF-Z maps overlaid, normal directions and scale bar.

For each test, the tensile bars failed in varying locations suggesting that unneccesary stress concentrators due to machining artifacts did not heavily contribute to the data. The stress-strain data is plotted in Figure 75 for all the microtensile bars tested. The raw load-displacment data was converted to stress strain using the gauge dimensions for each of the tensile bars which were accurately measured in an SEM. These plots can be individually analyzed to find Table 6. Yield strength was calculated using the typical 0.2% offset method, using a line proportional and parallel to the elastic modulus. The uniform elongation was calculated as the strain at the UTS.

	Microtensile Sample ID	Mechanical Property from Stress Strain Curve			
		Yield Strength (MPa)	Ultimate Tensile Strength (MPa)	Uniform Elongation	Total Strain
Quenched	Q1	667.82	868.04	0.079	0.083
	Q2	645.89	941.95	0.069	0.076
	Q3	561.73	841.89	0.056	0.150
	Q4	686.02	998.79	0.100	0.204
	Q5	621.70	914.26	0.064	0.179
	Q6	738.42	745.69	0.055	0.133
	Q7	869.54	889.62	0.099	0.198
	Q8	1071.90	1095.00	0.084	0.186
	Q9	876.01	878.79	0.099	0.173
	Q10	872.11	903.58	0.091	0.194
	Q11	707.67	727.44	0.102	0.180
	Q12	700.18	710.59	0.109	0.146
	Q13	835.62	1015.70	0.113	0.393
	Q14	909.88	965.86	0.079	0.131
	Q15	760.25	783.75	0.074	0.198
	Quenched Average ± STD	768.32 ± 130.30	885.40 ± 107.15	0.085 ± 0.02	0.175 ± 0.07
Tempered	T1	362.96	363.58	0.103	0.341
	T2	592.37	609.62	0.128	0.433
	T3	307.30	318.84	0.067	0.562
	T4	446.86	523.57	0.068	0.297
	T5	438.01	497.15	0.085	0.267
	T6	546.90	547.60	0.054	0.054
	T7	437.12	512.89	0.060	0.419
	T8	246.67	323.45	0.094	0.261
	T9	387.79	448.48	0.054	0.697
	T10	425.07	482.06	0.063	0.361
	Tempered Average ± STD	419.11 ± 97.06	462.72 ± 93.11	0.077 ± 0.02	0.369 ± 0.17

Table 6. Table of analyzed mechanical properties for each F82H microtensile bar

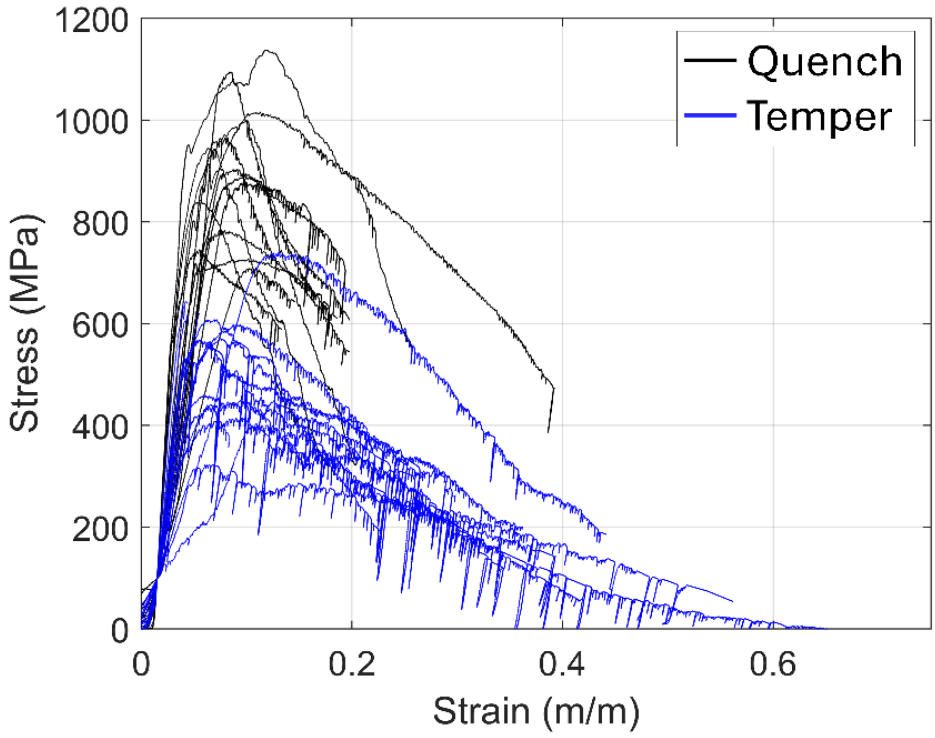

Figure 75. Stress-strain curves for all tested microtensile bars.

6.4 Discussion

Due to the size of the samples and the vastly differing material defects analyzed it is not optimal to look at the statistical trends in micromechanical data. Material anisotropy and defect differences create large scatter in mechanical property when measured on samples on the micron length scale [33,111,161]. Table 6 highlights this by the large scatter in calculated strength and strain values exceeding the nominal <10% standard deviation metric commonly used for experiments. However, statistically comparing the quenched and the tempered state finds that the quenching has the effect while this is increasing both yield strength and UTS by ~2x while reducing total strain by ~2x. These averages ignore the individual grain orientations, grain boundaries and individual defects samples within each microtensile bar, which have a very pronounced effect on the mechanical data, it is encouraging to see trends similar to what is expected on the bulk scale. Analysis of the individual microtensile tests individually leads to the most interesting results, allowing for the correlation of microstructure to mechanical response.

Single Crystal Samples

A total of 7 samples which were tested with only a single crystal within the gauge section of the microtensile bar. These were Q9, Q13, Q14, T2, T4, T7 and T9. On the bulk scale, many mechanisms can be attributed to plasticity in materials including twinning, grain boundary sliding, slip, cross slip, and phase transformation among many more [162]. However for single crystals, motion can be directly tied to dislocation movement for which there are two main types: glide and

climb. Glide happens when dislocations move along certain close packed planes within the material gliding sideways. Climb happens when dislocation move perpendicular to these planes upwards or downwards, shifting the dislocation to another layer of close packed atoms. A large glide movement of many dislocations at once is called slip in a crystal and is thought to be a dominant plasticity mechanism of single BCC F82H crystals. Slip in crystals prefer to occur within specific close packed lattice planes and directions within the planes typically called a slip system. The slip system, slip direction, and stress needed to activate slip are highly dependent on the orientation of the crystal tested [162,163]. However combining the EBSD analysis, SEM images of failure, and the mechanical data together finds important microstructural findings on the critical stresses to activate crystal slip.

When an external load is applied, only a portion of the total stress acts to drive slip. This component, known as the resolved shear stress (RSS), represents the shear stress resolved onto a particular slip system based on the crystal's orientation relative to the applied load. The Schmid factor quantifies this geometric relationship, defining how effectively an external stress is converted into shear stress on the slip plane and depends on the angles between the loading axis, slip plane normal, and slip direction. Plastic deformation begins when the resolved shear stress reaches a critical threshold value called the critical resolved shear stress (CRSS). The CRSS represents the minimum shear stress required to initiate dislocation movement within a slip system helping to quantify material resistance to plasticity at the microscopic scale. While the RSS just describes the force acting on the crystal's slip plane, the CRSS is just the RSS when the crystal begins to slip, quantified by the yield stress [64].

$$\tau_{RSS} = \frac{F\cos\lambda}{A/\cos\phi} = \frac{F}{A}\cos\phi\cos\lambda$$

$$\tau_{CRSS} = \frac{F_{Failure}}{A}\cos\phi\cos\lambda = \sigma_y\cos\phi\cos\lambda$$

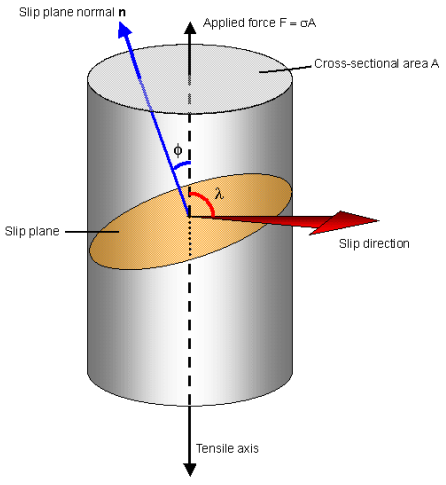

Figure 76. Components for calculating the critical resolved shear stress of a single crystal [164]

In order to calculate the CRSS for each of the single crystal samples, the slip plane, slip direction, and yield stress need to be known. Accurate determination of the slip plane and slip direction is difficult but can be aided with a joint approach of EBSD and SEM imaging. Gibson et al. outlines a method for using SEM images of slip correlated with the orientation of the crystal to determine the slip plane and direction [165]. Du et al, uses a similar methodology to determine slip system activation and CRSS on ferrite [163]. With this, the slip direction and slip plane of the F82H samples can be determined. BCC crystals have three potential slip systems: {110}<111>, {112}<111>, and {123}<111> labelled in Figure 77. However the {123}<111> slip system is not expected to be dominant at room temperature and is typically thermally activated at high temperatures in ferrite [163]. Therefore determination of whether the {110}<111> or the {112}<111> system is present is necessary. The EBSD analysis yielded precise data on the grain orientation of the crystal in the gauge section. Using the ATEX and AZtecCrystal software to analyze the EBSD data, a rotated cube representing the grain's lattice orientation can be found. This can be combined with the SEM images taken during the experiment right as the slip occurred and angle measurements of the slip plane to give an accurate estimation of the slip plane suspected to have been activated. Figure 78 shows an analysis of the microtensile bars with the associated slip system and direction associated with their failure.

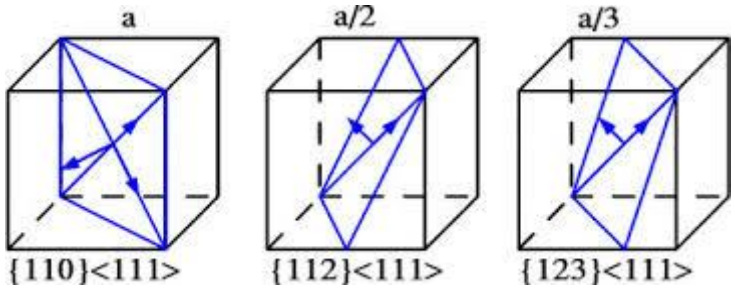

Figure 77. Possible slip systems and directions in BCC crystals [166].

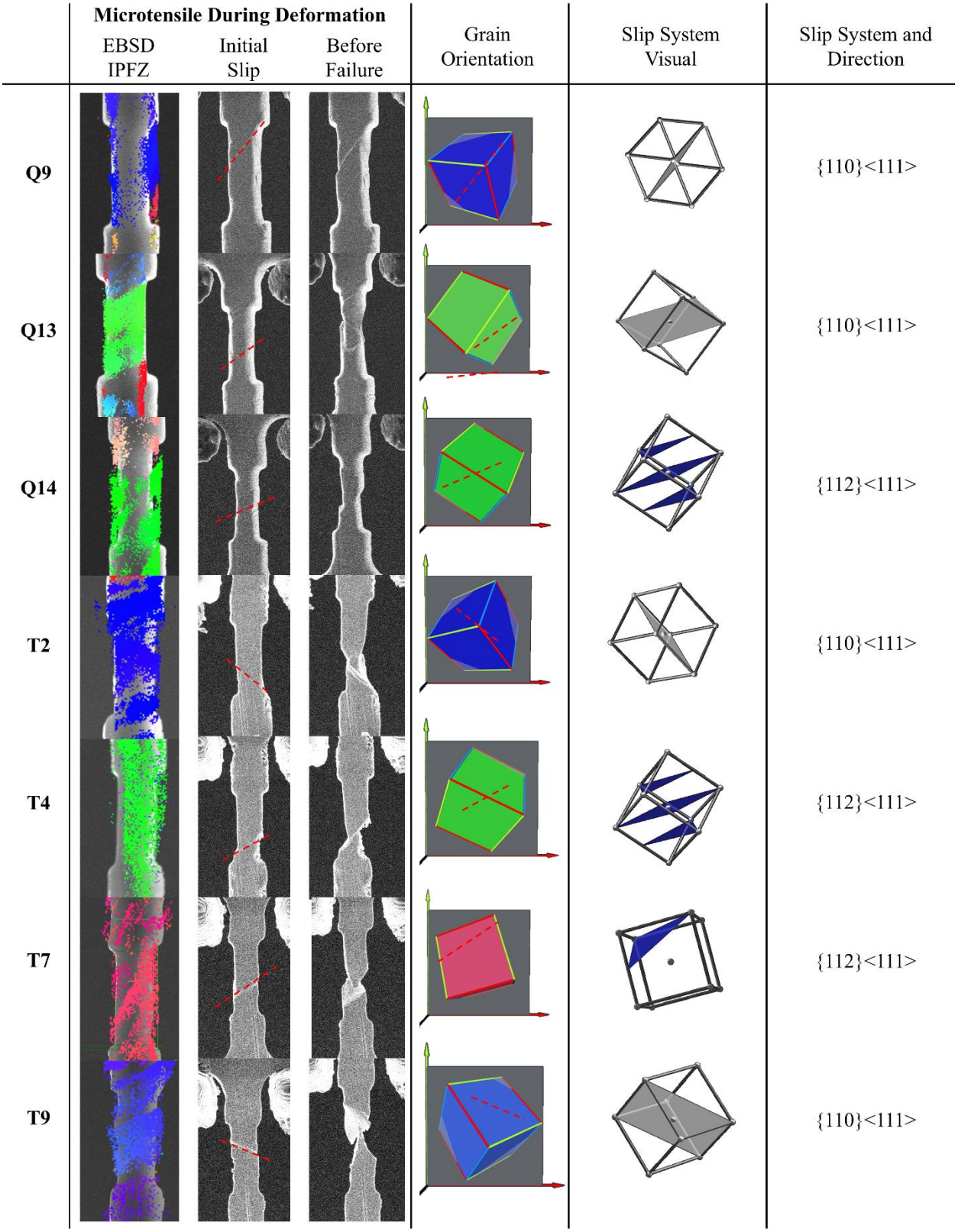

Figure 78. Analysis of slip system activated for single crystal F82H microtensile bars

The EBSD data maps the orientation of the crystal lattice as a function of space on the sample surface. Euler angles are part of this data set and explain the crystals rotation along each axis. These angles can be converted to normal directions in the lattice using the Bunge rotation matrix. Knowing that the loading direction is in the y-axis representing a direction of [010], the loading direction can be calculated from the Euler angles and normalized. Combining the loading direction with the slip system quantification and calculating the angles between both allows for the calculation of the CRSS. Table 7 shows the calculated CRSS which resulted from the analysis.

	Microtensile Sample ID	**Critical Resolved Shear Stress Determination**				
		Yield Strength (MPa)	Slip System	Loading Direction	Schmid Factor	Critical Resolved Shear Stress (MPa)
Quenched	Q9	876.01	{110}<111>	$[\bar{1}\ 10\ \bar{7}]$	0.479	417.68
	Q13	835.62	{110}<111>	$[\bar{2}\ \bar{1}\ 1]$	0.406	338.90
	Q14	909.88	{112}<111>	$[\bar{1}\ \bar{1}\ 1]$	0.363	330.67
Tempered	T2	592.37	{110}<111>	$[1\ 4\ \bar{4}]$	0.462	309.01
	T4	446.86	{112}<111>	$[2\ 1\ \bar{1}]$	0.429	222.83
	T7	437.12	{112}<111>	$[\bar{4}\ 2\ 1]$	0.448	187.85
	T9	387.79	{110}<111>	$[\bar{1}\ \bar{3}\ 2]$	0.451	198.86

Table 7. Critical resolved shear stress of single crystal F82H microtensile bars and parameters used for quantification

The CRSS quantifies what resolved shear stress a given crystallographic slip system will activate. CRSS analysis of BCC crystals like ferrite or tempered martensite is more complex than FCC crystals due to intricacies in slip and deformation mechanisms. While FCC crystals have only one dominant slip system on the close packed plane (CPP) and direction of {111}<110> giving combination of 12 independent slip systems. BCC crystals potentially have 48 different independent slip systems depending on the temperature, atom, and defects in the lattice. Due to there being no true CPP in BCC crystals, this creates a wide variety of behaviors in BCC crystals. Brittle tungsten and ductile ferrite exist in the BCC structure category showcasing the variety in property of this crystal structure. As a result of this complexity, BCC plastic deformation remains a widely studied topic with many intricacies. CRSS is an intrinsic material property but is dependent on the material, slip system activated, and defects present. While CRSS is ideally an intrinsic property of crystals, and the same for two single crystals of random orientations, activating th e same slip type, in practice, local anisotropy and dislocation movement can cause varying CRSS measurements.

Assessing the data, the quenched samples (Q9, Q13, Q14) show significantly higher yield strengths of 835–910 MPa when compared to the tempered samples (T2, T4, T7, T9) which exhibit

yield strengths in the 388–592 MPa range. This behavior is similar to what is shown on the bulk scale with quenched martensite showing an increased strength and reduced ductility. The empirical values for strength are extremely similar to what is expected for tempered martensite on the bulk scale. Shiba et al. reports a 490MPa yield strength for bulk F82H, Rowcliffe et al. finds a 573MPa yield strength, and Ando et al. reports a 534MPa yield strength [167–169]. While this is not expected due to size effects on mechanical property, this behavior is explained by looking at the defects sampled. Ando et al. theorizes that the carbide nucleation on grain boundaries provides a strengthening effect not seen on microscale samples [168]. While length scale effects predict that a much greater strength should be observed on the micro-scale, this lack of carbide grain boundary strengthening provides a possible explanation for why similar strengths are seen on both the bulk and micro-scale.

For the tempered condition the CRSS varies between 331–418 MPa compared to the quenched condition whose CRSS varies between 188–309 MPa. For both the quenched and tempered condition, both {110} and {112} systems are active, with similar CRSS magnitudes between the two slip systems. Du et al. shows a similar result with the CRSS of both {110} and {112} slip systems being approximately the same at room temperature. However when comparing the quenched and tempered state, it is found that the CRSS decreases across both slip systems upon tempering. Comparing Q14 with T4 and T7 which all activate the {112}<111> slip system, a decrease from 331MPa to 223-188MPa is found. This is similar when examining samples that activate the {110}<111> slip system like Q9 and Q13 with T2 and T9 where a similar decrease from 418-339MPa to 319-199MPa is measured following tempering. The CRSS is intrinsically tied to slip which occurs through the gliding of dislocations on slip planes. Therefore, any mechanism which impedes dislocation motion serves to increase the CRSS of a crystal. The features of quenched martensite which would contribute to dislocation motion are the effects of interstitial carbon, high dislocation density, and internal residual stresses that arise during quenching. The interstitial carbon atoms create local lattice strains that impede dislocation motion. High dislocation densities also serve to pin and impede further dislocation motion due to effects like forest hardening. Dislocations must overcome these pinning effects to glide, which raises the stress required for slip activation and in turn the CRSS.

Polycrystalline Samples

A comparison between the polycrystalline samples and the single crystal samples finds interesting conclusions. Table 8 shows a comparison between the microtensile bars which were fabricated with multiple crystals within the gauge section versus those with only a single crystal.

	Grain Boundaries Sampled	Mechanical Property from Stress Strain Curve			
		Yield Strength (MPa)	Ultimate Tensile Strength (MPa)	Uniform Elongation	Total Strain
Quenched	Single Crystal	873.84 ± 30.36	953.45 ± 56.58	0.097 ± 0.01	0.232 ± 0.115
	Polycrystalline	741.94 ± 132.33	868.38 ± 110.02	0.082 ± 0.02	0.161 ± 0.04
Tempered	Single Crystal	466.04 ± 76.30	523.64 ± 57.35	0.077 ± 0.03	0.462 ± 0.146
	Polycrystalline	387.82 ± 96.81	422.11 ± 90.18	0.077 ± 0.02	0.308 ± 0.15

Table 8. Comparison between F82H microtensile mechanical property between samples encompassing single and multiple crystals

One of the most interesting findings is that the strengths for the single crystal samples are higher than that of the polycrystalline samples for both conditions in both yield and UTS. This result suggests that the carbide grain boundary strengthening effect used to previously explain the lack of size effect in these F82H is not correct. If grain boundaries were to strengthen the structure, the introduction grain boundaries while keeping length scale the same, should have a strengthening effect however this was not measured, meaning that another mechanism governs size effect strength measurements in F82H. However the yield stress decrease between the single crystal to polycrystalline for the quenched condition can be calculated as 132MPa while for the tempered condition is only 78MPa. This shows that despite the introduction of grain boundaries which serve to weaken the yield stress, tempering has the effect of reducing this drop in yield stress. This helps support the idea that tempering serves to stabilize grain boundaries through the nucleation of carbides. The smaller relative scatter on the single crystal samples strength data compared to the polycrystalline samples suggests that strength effects due to crystal mechanical anisotropy is low.

The analysis of individual polycrystalline tensile bars also yields interesting findings. Typically in microtensile samples, large strain bursts can be found due to dislocation avalanches which reduce strain hardening behavior on the microscale. A visual analysis of the stress strain curves in the tempered and quenched conditions find that the quantity and magnitude of these strain bursts is reduced in the quenched state. These strain bursts can occur from slip events across the grain and as the lattice suddenly shifts, temporarily reconnects bonds when an obstacle is hit, until slip occurs again causing this sawtooth serrated shaped stress strain response. The presence of these strain bursts are further evidence on top of the lower CRSS measured that crystal slip is easier in the tempered samples. In contrast in the quenched state, it is suspected that dislocation pileup at boundaries and impeded dislocation motion from the high dislocation density suppresses strain bursts causing more stable plastic flow [81,170]. However, a consequence of this lack crystal slip, is that when dislocation pileup reaches a critical limit fracture across boundaries or other stress concentrators causes sudden failure evidenced by the lower total strains that the quenched microtensile tests experienced. Figure 79 shows Q6 immediately before fracture. While mostly encapsulating a single grain, a small LAGB is found in the middle of the gauge section which

failure initiates on. Despite, being mostly made of a single grain, this small LAGB inclusion within the tensile bar is able to cause yielding and fracture below the average.

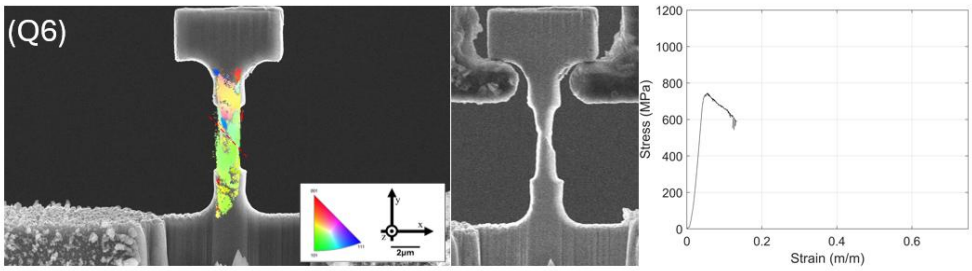

Figure 79. F82H microtensile bar Q6 right before fracture with associated stress strain curve and SEM image before testing with EBSD IPFZ map overlaid

Figure 80 shows microtensile bar Q7 during deformation with its associated stress strain curve. Q7 includes a HAGB within the gauge section which initially deforms under load as shown in the first SEM image. Despite the first plasticity event occurring at the grain boundary, a strain hardening effect is observed as the grain boundary begins to deform. This strain hardening effect is large enough to pass the critical resolved shear stress of the bottom grain causing single crystal slip in the lower grain of the tensile gauge section.

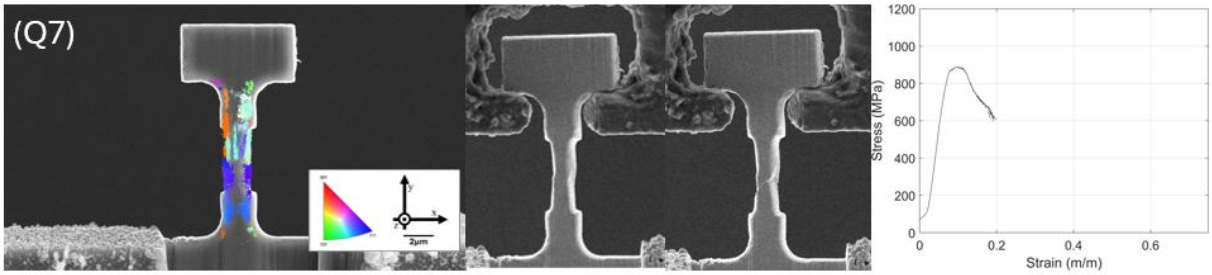

Figure 80. F82H microtensile bar Q7 during tensile test with associated stress strain curve and SEM image before testing with EBSD IPFZ map overlaid

Figure 81 displays microtensile Q5 during the tensile test with its associated stress strain curve. While at first appearing to fail due to single crystal slip, it is found through EBSD analysis that the failure area is densely packed with fine grains with multiple LAGB interfaces between. Despite the high density of LAGBs between the grains, slip is able to transmit between the grains causing failure. Further analysis finds that the failure initiates close to a LAGB interface. As a result of this, the total strain and uniform elongation of Q5 is much less than that of the quenched condition single crystal samples due to this early LAGB failure.

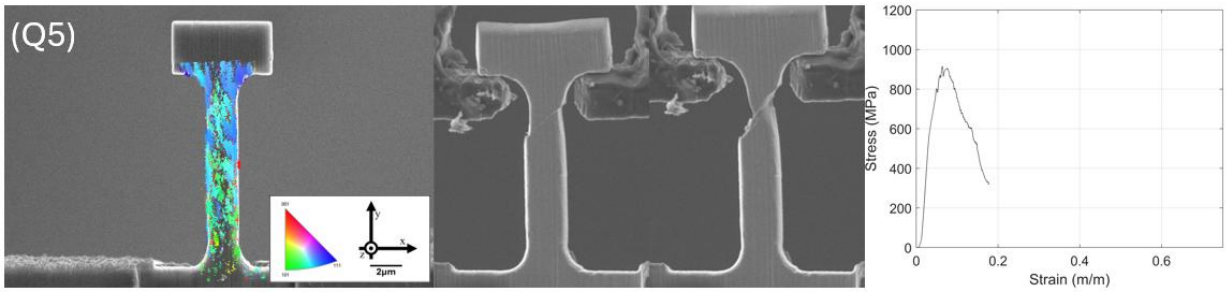

Figure 81. F82H microtensile bar Q5 during tensile test with associated stress strain curve and SEM image before testing with EBSD IPFZ map overlaid

Figure 82 shows tempered microtensile bar T8 during a the microtensile test. This tempered sample displays a lower yield stress and lower elongation than the average, due to an early fracture on a LAGB interface. However unlike quenched microtensile bars like Q6 and Q5 which also fracture on a LAGB and show a greatly reduced elongation with sudden fracture, T8 is able to deform plastically with strain hardening. Following failure initiation on the LAGB interface, a slower rate of stress decrease and a greater frequency of strain bursts is observed when compared to the quenched samples which also fractured on LAGB interfaces. Further in the tensile test, necking is observed accompanied by failure at the LAGB interface. It is suspected that the increased frequency of strain bursts is due to the fine carbides nucleated on the grain boundary interface. Despite failure at the grain boundary, mechanisms like grain boundary pinning and Zener pinning create obstacles for grain boundary movement. As the grain boundary is failing and moving, the carbide precipitates create a fine array of obstacles which impede the motion of the grain boundary, causing strain bursts as the grain repeatedly slips, and re-bonds when it encounters another precipitate obstacle. It seems like while the LAGB failure is still preferred over single crystal slip in both tempered and quenched state, LAGBs of the tempered condition are able to sustain stable plastic flow through effective dislocation emission to other boundaries as opposed to the quenched condition.

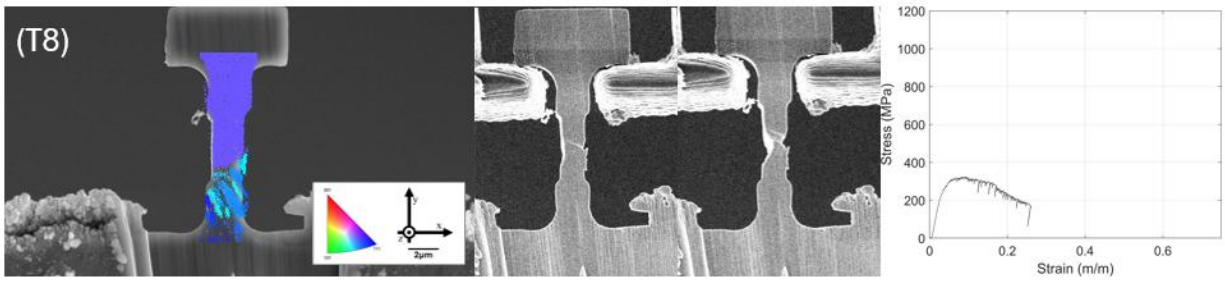

Figure 82. F82H microtensile bar T8 during tensile test with associated stress strain curve and SEM image before testing with EBSD IPFZ map overlaid

Figure 83 shows tempered microtensile bar T1 with its associated stress strain curve. Despite a HAGB interface being included within the gauge section at a near 45° angle preferential

for shear stress transfer to this interface, single crystal slip on the top grain actually causes failure of the tensile bar. This unexpected result helps to support the fact that carbides nucleated at HAGB interfaces in tempered F82H increase the strength of these interfaces. While all the quenched samples which included HAGB interfaces had failure initiate at the grain boundary, T1 suggests that the nucleation of carbides at HAGBs has significant interface strengthening effect. In general this correlates previous studies on HAGB nucleation of carbides in F82H. Carbides nucleate preferentially on interfaces within F82H with a preference for HAGBs over LAGBs [71]. This strengthening effect seen in T1 bolsters the theory of expected mechanical strength increase due to the presence of these carbides.

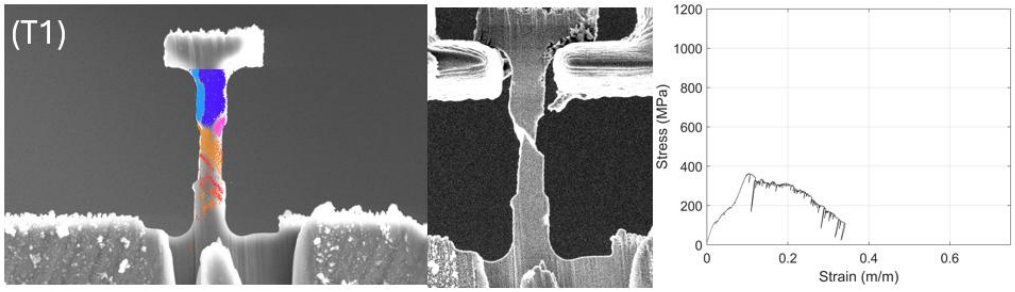

Figure 83. F82H microtensile bar T1 during tensile test with associated stress strain curve and SEM image before testing with EBSD IPFZ map overlaid

Comparing these individual tensile tests reveal that the presence of LAGB interfaces in both the quenched and tempered conditions cause locations for preferential failure initiation. In cases where LAGBs were included within the gauge section, initial failure tended to form from LAGBs across both quenched and tempered microtensile bars. Frequent load drops and strain bursts in the tempered conditions show evidence for carbide precipitates nucleating on grain boundaries, inhibiting sudden failure of the LAGB interface. HAGB interfaces showed a different phenomena between the quenched and tempered state however. HAGB initiated failure was preferred in the quenched condition over LAGB failure. But upon tempering, HAGB interfaces showed a greater resistance to failure, preferring single crystal slip to fracture along the boundary.

6.5 Conclusions

In conclusion, 25 microtensile bars were fabricated and tested on F82H. A joint laser-FIB approach was used to rapidly make microtensile bars for uniaxial tensile testing. A picoindenter setup was used to test the tensile bars which were divided between 15 made from quenched F82H and 10 tempered F82H. EBSD, small scale mechanical testing, and in-situ deformation imaging combined to allow for detailed information to be made on the deformation behavior of F82H between quenched and tempered states. In total, the following conclusions can be made:

- The CRSS of F82H reduces following tempering with no noticeable change in slip systems activated.

- The measured yield strength and UTS of F82H tested on the microscale is roughly equivalent to bulk scale studies and does not seem to follow the expected length scale trend of smaller is stronger. This is theorized to be due to the fine lath structure.
- Overall, tempering increased strain to failure by a factor of 2.1 but decreased yield strength and UTS by a factor of 1.83 and 1.91 respectively.
- The presence of grain boundaries overall decreases the strength of both the quenched and tempered microtensile samples.
- Tempering decreased the strength drop between single crystal and polycrystalline samples showing the effect of carbides on mechanical strength
- LAGBs were preferred for fracture initiation in both quenched and tempered samples causing premature failure and reduced yield strength
- HAGBs were preferred for fracture only in the quenched samples. Some tempered samples including HAGBs were not observed to fracture on these boundaries.
- Carbides nucleation on HAGBs are thought to be the main driving factor between this difference in grain boundary behavior. Furthermore, frequent strain bursts in the tempered F82H are evidence for the greater obstacle concentration for impeding failure due to slip.

Chapter 8

Conclusions

This dissertation aimed at probing the mechanical effects of carbides at martensitic boundaries in F82H. To do this, quenched F82H, devoid of carbides, was tested and compared against tempered F82H, with carbides precipitated. Small scale mechanical testing was used due to its capabilities of isolating defect interactions within small volumes of material in order to probe the effect of these carbides. However, in order to do this, a two challenges in SSMT needed to be overcome: the time intensive sample preparation process and the interpretation of SSMT results to macroscopic scale. Once these challenges were addressed, small scale mechanical testing was showcased on F82H using both micromechanical spectroscopy and microtensile testing. SSMT allowed for the detailed study of the interactions of carbides within the F82H. The study of each of these effects form the major chapters of this dissertation and the major conclusions of each chapter are outlined below:

Chapter 4 explored the usage of fs-laser machining for SSMT sample preparation.

- A procedure was developed to rapidly make micron scale 2D structures using a joint fs-laser and FIB approach which saved hours of sample preparation time from each SSMT sample made.
- This procedure was successfully tested on gallium metal, which has an extremely low melting point.
- The success of this procedure in making testable specimen on Ga showed a lack of heat affected zone in fs-laser machining using specific parameters and paved the way for its use on F82H for micromechanics.

Chapter 5 investigated length scale effects in SSMT.

- Two scales of microtensile bars were made and correlated with fs-laser machined bulk tensile bars on Zircaloy-4, another nuclear relevant material.
- Deformation of the microscale tensile bars showed a clear “smaller is stronger” trend where smaller samples appeared stronger than bulk scale samples
- Defect considerations across different length scales were analyzed laying the foundation for SSMT data interpretation in F82H

Chapter 6 measured the effect of carbides on the internal friction of F82H

- The novel μMS technique was tested successfully on F82H
- Damping capacity and internal friction increased following tempering with an increase in elastic modulus.

- Analysis of damping mechanisms found that carbides nucleated at HAGB samples did not heavily contribute to damping.
- Damping due to dislocations interacting with carbides on lath boundaries is suspected to be heavily influential on the internal friction of F82H.

Chapter 7 measured the effect of carbides on the uniaxial tension mechanical deformation of F82H

- Tempering decreased the yield strength of F82H but significantly increased the ductility relative to the quenched state.
- Low angle grain boundaries were preferred for fracture initiation sites in both the quenched and tempered states
- High angle grain boundaries were only preferred for fracture initiation by the quenched state. High angle grain boundaries were strengthened in the tempered state, preferring single crystal slip of adjacent grains rather than grain boundary failure.
- The presence of grain boundaries generally weakened the structure of F82H compared to single crystal samples but the weakened strength was mitigated through tempering.

This dissertation aimed at probing the effect of carbide nucleation in F82H. While complex and requiring further research, some general conclusions can be made about the topic. Carbides seem to have a tendency to nucleate with preference for high angle grain boundaries over low angle grain boundaries within F82H. However this nucleation at high angle grain boundaries does not strongly contribute to the increased damping capacity of tempered martensite. Instead carbides formed at low angle grain boundaries like laths are able to interact with dislocations to greatly increase damping and internal friction in F82H. This means that for resisting dynamic stresses like vibrations and cyclical loading, a greater amount of these low angle grain boundaries would greatly increase resistance to dynamic loading capabilities. Also, with the lack of carbide nucleation like in quenched F82H, the greatly reduced damping capacity would cause a decreased resistance to cyclical fatigue due to the increased transmitted stress amplitudes within the material. This would provide an explanation for why martensitic welds made from quenched martensite fail under dynamic loading conditions. In contrast, due to static tension loading conditions carbide precipitation to high angle grain boundaries has a strengthening effect on the microstructure. The preferential carbide nucleation is then used to strengthen these interfaces, causing an increased resistance to failure initiation on grain boundaries. Furthermore, these carbides strengthen these high angle grain boundaries enough to the point that the lowered critical resolved shear stress of tempered F82H can be overcome, triggering slip rather than grain boundary failure in adjacent grains. Low angle grain boundaries which do not nucleate carbides as readily do not benefit from this mechanism and often initiate failure along these boundaries.

In summary, under dynamic loading, high angle grain boundaries are less preferred to low angle grain boundaries due to carbide preferential nucleation not allowing for energy dissipation mechanisms to strongly interact. However under static tension loading, high angle grain boundaries are preferred to low angle grain boundaries due to carbide preferential nucleation strengthening of the interface.

Chapter 9

References

[1] World Nuclear Performance Report 2023, World Nuclear Association, 2023.

[2] Record-breaking year for nuclear electricity generation, World Nuclear News (2025). https://world-nuclear-news.org/articles/record-breaking-year-for-nuclear-electricity-generation (accessed October 21, 2025).

[3] J. Mahaffey, Atomic Awakening, Simon and Schuster, 2010.

[4] Radioactive Quack Cures, Museum of Radiation and Radioactivity (n.d.). https://www.orau.org/health-physics-museum/collection/radioactive-quack-cures/index.html (accessed April 22, 2025).

[5] Most U.S. nuclear power plants were built between 1970 and 1990 - U.S. Energy Information Administration (EIA), (n.d.). https://www.eia.gov/todayinenergy/detail.php?id=30972 (accessed April 22, 2025).

[6] N. Muellner, N. Arnold, K. Gufler, W. Kromp, W. Renneberg, W. Liebert, Nuclear energy - The solution to climate change?, Energy Policy 155 (2021) 112363. https://doi.org/10.1016/j.enpol.2021.112363.

[7] M. Roser, Why did renewables become so cheap so fast?, Our World in Data (2020). https://ourworldindata.org/cheap-renewables-growth (accessed October 30, 2025).

[8] L. Larsen, A. Abou-Jaoude, N. Guaita, N. Stauff, Nuclear Energy Cost Estimates for Net Zero World Initiative, 2024. https://doi.org/10.2172/2283652.

[9] P. Eash-Gates, M.M. Klemun, G. Kavlak, J. McNerney, J. Buongiorno, J.E. Trancik, Sources of Cost Overrun in Nuclear Power Plant Construction Call for a New Approach to Engineering Design, Joule 4 (2020) 2348–2373. https://doi.org/10.1016/j.joule.2020.10.001.

[10] P.H. Tice, A Strategy for Financing the Nuclear Future, (n.d.).

[11] G. Rothwell, Projected electricity costs in international nuclear power markets, Energy Policy 164 (2022) 112905. https://doi.org/10.1016/j.enpol.2022.112905.

[12] R.L. Kennedy Isabelle Pula and Brian, Support for expanding nuclear power is up in both parties since 2020, Pew Research Center (2025). https://www.pewresearch.org/short-reads/2025/10/16/support-for-expanding-nuclear-power-is-up-in-both-parties-since-2020/ (accessed October 21, 2025).

[13] E. Morse, Nuclear Fusion, Springer International Publishing, Cham, 2018. https://doi.org/10.1007/978-3-319-98171-0.

[14] B.M. of Engineering, Op-ed: Fusion power is a strong alternative energy source, Fung Institute for Engineering Leadership (2020). https://funginstitute.berkeley.edu/news/op-ed-fusion-power-is-a-strong-alternative-energy-source/ (accessed October 21, 2025).

[15] SPARC®: Proving commercial fusion energy is possible, (n.d.). https://cfs.energy/technology/sparc (accessed November 24, 2025).

[16] In Conversation: Will Regan, Pacific Fusion, FusionXInvest (n.d.). https://fusionxinvest.com/insight/7409/in-conversation-will-regan-pacific-fusion/ (accessed November 24, 2025).

[17] Inertia | Proven Fusion Science meets a Proven Fusion Team, (n.d.). https://inertia.com (accessed November 24, 2025).
[18] S. Takeda, A.R. Keeley, S. Managi, How Many Years Away is Fusion Energy? A Review, J Fusion Energ 42 (2023) 16. https://doi.org/10.1007/s10894-023-00361-z.
[19] (PDF) Achieving an optimum slowing-down energy distribution functions and corresponding reaction rates for the (D+3He and T+3He) fusion reactions, ResearchGate (n.d.). https://www.researchgate.net/publication/325374052_Achieving_an_optimum_slowing-down_energy_distribution_functions_and_corresponding_reaction_rates_for_the_D3He_and_T3He_fusion_reactions (accessed October 17, 2025).
[20] A. Horvath, E. Rachlew, Nuclear power in the 21st century: Challenges and possibilities, Ambio 45 (2016) 38–49. https://doi.org/10.1007/s13280-015-0732-y.
[21] S. Takeda, A.R. Keeley, S. Managi, How Many Years Away is Fusion Energy? A Review, J Fusion Energ 42 (2023) 16. https://doi.org/10.1007/s10894-023-00361-z.
[22] A shot for the ages: Fusion ignition breakthrough hailed as 'one of the most impressive scientific feats of the 21st century' | Lawrence Livermore National Laboratory, (n.d.). https://www.llnl.gov/article/49301/shot-ages-fusion-ignition-breakthrough-hailed-one-most-impressive-scientific-feats-21st (accessed October 31, 2025).
[23] Giant international fusion project is in big trouble, (n.d.). https://www.science.org/content/article/giant-international-fusion-project-big-trouble (accessed October 30, 2025).
[24] admin, Facts & Figures, ITER - the Way to New Energy (2023). https://www.iter.org/facts-figures (accessed October 21, 2025).
[25] C. Bustreo, N. Ben Ayed, M. Biberacher, G. Bongiovì, E. Börcsök, R. Čadenović, V. Cok, G. Colucci, E. De Marchi, D.N. Dongiovanni, Z. Ferencz, R. Geysmans, A. Giacometti, F. Gracceva, C.R. Jones, R. Kembleton, J. Kenens, U. Lamut, Y. Lechon, D. Lerede, N.J. Lopes Cardozo, G. Meskens, A. von Müller, V. Olahne Groma, C. Oltra, M.T. Orlando, J. Povh, A. Prades, L. Savoldi, P. Stankiewicz, A. Trotta, C. Turcanu, S. Vitiello, S.H. Ward, Socio economic perspectives on fusion power for a sustainable future energy system, Fusion Engineering and Design 208 (2024) 114679. https://doi.org/10.1016/j.fusengdes.2024.114679.
[26] B. Lindley, T. Roulstone, G. Locatelli, M. Rooney, Can fusion energy be cost-competitive and commercially viable? An analysis of magnetically confined reactors, Energy Policy 177 (2023) 113511. https://doi.org/10.1016/j.enpol.2023.113511.
[27] What is ITER?, ITER (n.d.). http://www.iter.org/proj/inafewlines (accessed July 22, 2024).
[28] A. Quadling, W.E. Lee, J. Astbury, Materials challenges for successful roll-out of commercial fusion reactors, J. Phys. Energy 4 (2022) 030401. https://doi.org/10.1088/2515-7655/ac73b2.
[29] C. Cabet, F. Dalle, E. Gaganidze, J. Henry, H. Tanigawa, Ferritic-martensitic steels for fission and fusion applications, Journal of Nuclear Materials 523 (2019) 510–537. https://doi.org/10.1016/j.jnucmat.2019.05.058.
[30] S.J. Zinkle, J.T. Busby, Structural materials for fission & fusion energy, Materials Today 12 (2009) 12–19. https://doi.org/10.1016/S1369-7021(09)70294-9.
[31] R. Hill, History of strength of materials, Journal of the Mechanics and Physics of Solids 2 (1954) 138. https://doi.org/10.1016/0022-5096(54)90010-1.
[32] Stress–strain curve, Wikipedia (2025). https://en.wikipedia.org/w/index.php?title=Stress%E2%80%93strain_curve&oldid=1304514955 (accessed December 2, 2025).

[33] P. Hosemann, C. Shin, D. Kiener, Small scale mechanical testing of irradiated materials, J. Mater. Res. 30 (2015) 1231–1245. https://doi.org/10.1557/jmr.2015.26.
[34] A. Jaksic, J. Nikolov, A. Palma, Special issue: applications of radiation in science and technology, Eur. Phys. J. Spec. Top. 232 (2023) 1459–1463. https://doi.org/10.1140/epjs/s11734-023-00907-4.
[35] G. Was, Fundamentals of Radiation Materials Science, Springer Berlin Heidelberg, Berlin, Heidelberg, 2007. https://doi.org/10.1007/978-3-540-49472-0.
[36] C.N. Andoh, Binary Collision and Molecular Dynamics Simulation of Fe-Ni-Cr Alloys at Supercritical Water Condition, 2016.
[37] M.J. Norgett, M.T. Robinson, I.M. Torrens, A proposed method of calculating displacement dose rates, Nuclear Engineering and Design 33 (1975) 50–54. https://doi.org/10.1016/0029-5493(75)90035-7.
[38] S. Chen, D. Bernard, J. Tommasi, C. De Saint Jean, Improved model for atomic displacement calculation, EPJ Web Conf. 239 (2020) 08003. https://doi.org/10.1051/epjconf/202023908003.
[39] S. Chen, D. Bernard, On the calculation of atomic displacements using damage energy, Results in Physics 16 (2020) 102835. https://doi.org/10.1016/j.rinp.2019.102835.
[40] K. Nordlund, F. Djurabekova, Multiscale modelling of irradiation in nanostructures, J Comput Electron 13 (2014) 122–141. https://doi.org/10.1007/s10825-013-0542-z.
[41] M. Zhang, J. Zhao, X. Meng, Z. Chen, Q. Wang, X. Guan, T. Wang, Crystallographic orientation dependent of blisters formation on tungsten surface exposed to helium ions, Journal of Nuclear Science and Technology 58 (2021) 1071–1078. https://doi.org/10.1080/00223131.2021.1911872.
[42] C. Fan, S. Pan, X. Hu, B. He, M. Huang, Mechanisms of helium irradiation blistering and surface deformation in tungsten, Acta Materialia 254 (2023) 118993. https://doi.org/10.1016/j.actamat.2023.118993.
[43] Y. Chen, Y. Yang, Y. Huang, T. Allen, B. Alexandreanu, K. Natesan, Void Swelling and Microstructure of Austenitic Stainless Steels Irradiated in the BOR - 60 Reactor, 2012. https://doi.org/10.2172/1224950.
[44] B. Kombaiah, Y. Zhou, K. Jin, A. Manzoor, J.D. Poplawsky, J.A. Aguiar, H. Bei, D.S. Aidhy, P.D. Edmondson, Y. Zhang, Nanoprecipitates to Enhance Radiation Tolerance in High-Entropy Alloys, ACS Appl. Mater. Interfaces 15 (2023) 3912–3924. https://doi.org/10.1021/acsami.2c17540.
[45] L.L. Snead, Y. Katoh, S. Connery, Swelling of SiC at intermediate and high irradiation temperatures, Journal of Nuclear Materials 367–370 (2007) 677–684. https://doi.org/10.1016/j.jnucmat.2007.03.097.
[46] F. Li, L. Guo, Y. Chen, Y. Long, Y. Wei, Z. Xie, H. Luo, W. Lin, Z. Zhou, H. Wang, Microstructure evolution and void swelling of ODS ferritic/martensitic steel under high damage irradiation, Materials Characterization 205 (2023) 113272. https://doi.org/10.1016/j.matchar.2023.113272.
[47] L.K. Mansur, Theory and experimental background on dimensional changes in irradiated alloys, Journal of Nuclear Materials 216 (1994) 97–123. https://doi.org/10.1016/0022-3115(94)90009-4.
[48] W.A. Coghlan, L.K. Mansur, Characteristics of irradiation creep in the first wall of a fusion reactor, Journal of Nuclear Materials 104 (1981) 1245–1250. https://doi.org/10.1016/0022-3115(82)90772-3.

[49] Physics-based model of irradiation creep for ferritic materials under fusion energy operation conditions | Journal of Applied Physics | AIP Publishing, (n.d.). https://pubs.aip.org/aip/jap/article/132/22/225101/2838120/Physics-based-model-of-irradiation-creep-for (accessed December 2, 2025).
[50] D.A. Brown, M.B. Chadwick, R. Capote, A.C. Kahler, A. Trkov, M.W. Herman, A.A. Sonzogni, Y. Danon, A.D. Carlson, M. Dunn, D.L. Smith, G.M. Hale, G. Arbanas, R. Arcilla, C.R. Bates, B. Beck, B. Becker, F. Brown, R.J. Casperson, J. Conlin, D.E. Cullen, M.-A. Descalle, R. Firestone, T. Gaines, K.H. Guber, A.I. Hawari, J. Holmes, T.D. Johnson, T. Kawano, B.C. Kiedrowski, A.J. Koning, S. Kopecky, L. Leal, J.P. Lestone, C. Lubitz, J.I. Márquez Damián, C.M. Mattoon, E.A. McCutchan, S. Mughabghab, P. Navratil, D. Neudecker, G.P.A. Nobre, G. Noguere, M. Paris, M.T. Pigni, A.J. Plompen, B. Pritychenko, V.G. Pronyaev, D. Roubtsov, D. Rochman, P. Romano, P. Schillebeeckx, S. Simakov, M. Sin, I. Sirakov, B. Sleaford, V. Sobes, E.S. Soukhovitskii, I. Stetcu, P. Talou, I. Thompson, S. van der Marck, L. Welser-Sherrill, D. Wiarda, M. White, J.L. Wormald, R.Q. Wright, M. Zerkle, G. Žerovnik, Y. Zhu, ENDF/B-VIII.0: The 8th Major Release of the Nuclear Reaction Data Library with CIELO-project Cross Sections, New Standards and Thermal Scattering Data, Nuclear Data Sheets 148 (2018) 1–142. https://doi.org/10.1016/j.nds.2018.02.001.
[51] ch302.cm.utexas.edu/nuclear/radioactivity/selector.php?name=band-stability, (n.d.). https://ch302.cm.utexas.edu/nuclear/radioactivity/selector.php?name=band-stability (accessed December 2, 2025).
[52] M.R. Gilbert, S.L. Dudarev, S. Zheng, L.W. Packer, Transmutation, gas production, and helium embrittlement in materials under neutron irradiation., (n.d.).
[53] M. Moschetti, P.A. Burr, E. Obbard, J.J. Kruzic, P. Hosemann, B. Gludovatz, Design considerations for high entropy alloys in advanced nuclear applications, Journal of Nuclear Materials 567 (2022) 153814. https://doi.org/10.1016/j.jnucmat.2022.153814.
[54] admin, Tritium breeding, ITER - the Way to New Energy (2023). https://www.iter.org/machine/supporting-systems/tritium-breeding (accessed December 4, 2025).
[55] ITER Talks (2): The ITER Blanket System, 2021. https://www.youtube.com/watch?v=-pLdtF0fJRE (accessed July 22, 2024).
[56] Y. Kawamura, T. Hirose, W. Guan, Y. Miyoshi, T. Katagiri, A. Wakasa, Y. Someya, K. Ochiai, H. Uto, J. Kim, Y. Koga, M. Nakajima, T. Nozawa, Y. Sakamoto, H. Tanigawa, T. Hayashi, Overview of progress on water cooled ceramic breeder blanket in Japan, Fusion Engineering and Design 201 (2024) 114260. https://doi.org/10.1016/j.fusengdes.2024.114260.
[57] Y. Kawamura, H. Gwon, W. Guan, H. Tanigawa, T. Hirose, A. Wakasa, S. Yoshino, T. Ouchi, K. Hattori, N. Chiba, T. Kushida, S. Mori, H. Iida, T. Yamamoto, T. Yamanishi, H. Uto, Y. Someya, K. Ochiai, H. Sakasegawa, J. Kim, H. Nakamura, H. Tanigawa, S. Ohira, T. Hayashi, Progress of water cooled ceramic breeder test blanket module system, Fusion Engineering and Design 161 (2020) 112050. https://doi.org/10.1016/j.fusengdes.2020.112050.
[58] ITER Talks (1): Introduction to ITER, 2021. https://www.youtube.com/watch?v=kDaTQSmsJC8 (accessed July 22, 2024).
[59] G. Qiu, D. Zhan, L. Cao, Z. Jiang, Review on development of reduced activated ferritic/martensitic steel for fusion reactor, J. Iron Steel Res. Int. 29 (2022) 1343–1356. https://doi.org/10.1007/s42243-022-00796-2.
[60] A. Kohyama, A. Hishinuma, D.S. Gelles, R.L. Klueh, W. Dietz, K. Ehrlich, Low-activation ferritic and martensitic steels for fusion application, Journal of Nuclear Materials 233–237 (1996) 138–147. https://doi.org/10.1016/S0022-3115(96)00327-3.

[61] M. Moschetti, P. Burr, E. Obbard, J.J. Kruzic, P. Hosemann, B. Gludovatz, Design considerations for high entropy alloys in advanced nuclear applications, Journal of Nuclear Materials 567 (2022). https://doi.org/10.1016/j.jnucmat.2022.153814.
[62] Q. Huang, X. Wang, S. Sun, Y. Liu, H. Liao, P. Zheng, L. Peng, Y. Zhai, Development of reduced activation ferritic/martensitic steels in China, Journal of Nuclear Materials 568 (2022) 153887. https://doi.org/10.1016/j.jnucmat.2022.153887.
[63] Hiroyasu Tanigawa, Development of Reduced Activation Ferritic/Martensitic Steel, IFERC Newsletter (2013).
[64] W. Callister, D. Rethwisch, Material Science and Engineering – An Introduction, 2007.
[65] Time-Temperature-Transformation (TTT) Diagram | Metallurgy for Dummies, (n.d.). https://www.metallurgyfordummies.com/time-temperature-transformation-ttt-diagram.html (accessed July 22, 2024).
[66] U.R. Kattner, The CALPHAD method and its role in material and process development, NIST 13 (2016) 3–15.
[67] A.L. Roitburd, G.V. Kurdjumov, The nature of martensitic transformations, Materials Science and Engineering 39 (1979) 141–167. https://doi.org/10.1016/0025-5416(79)90055-7.
[68] J.D. Verhoeven, Metallurgy of Steel for Bladesmiths & Others who Heat Treat and Forge Steel, (n.d.).
[69] Strengthening mechanisms of reduced activation ferritic/martensitic steels: A review | International Journal of Minerals, Metallurgy and Materials, (n.d.). https://link.springer.com/article/10.1007/s12613-020-2121-1 (accessed October 31, 2025).
[70] S. Taller, G. VanCoevering, B.D. Wirth, G.S. Was, Predicting structural material degradation in advanced nuclear reactors with ion irradiation, Sci Rep 11 (2021) 2949. https://doi.org/10.1038/s41598-021-82512-w.
[71] S. Kano, H.L. Yang, R. Suzue, Y. Matsukawa, Y. Satoh, H. Sakasegawa, H. Tanigawa, H. Abe, Precipitation of carbides in F82H steels and its impact on mechanical strength, Nuclear Materials and Energy 9 (2016) 331–337. https://doi.org/10.1016/j.nme.2016.09.017.
[72] Z. Hou, P. Hedström, Y. Xu, W. Di, J. Odqvist, Microstructure of Martensite in Fe–C–Cr and its Implications for Modelling of Carbide Precipitation during Tempering, ISIJ International 54 (2014) 2649–2656. https://doi.org/10.2355/isijinternational.54.2649.
[73] J. Zhou, Y. Shen, N. Jia, Strengthening mechanisms of reduced activation ferritic/martensitic steels: A review, Int J Miner Metall Mater 28 (2021) 335–348. https://doi.org/10.1007/s12613-020-2121-1.
[74] J. Parkin, S. Birosca, Crystallographic orientation influence on slip system activation and deformation mechanisms in Waspaloy during in-situ mechanical loading, Journal of Alloys and Compounds 865 (2021) 158548. https://doi.org/10.1016/j.jallcom.2020.158548.
[75] P. Hosemann, Small-scale mechanical testing on nuclear materials: bridging the experimental length-scale gap, Scripta Materialia 143 (2018) 161–168. https://doi.org/10.1016/j.scriptamat.2017.04.026.
[76] A. Dong, J. Duckering, J. Peterson, S. Lam, D. Routledge, P. Hosemann, Femtosecond Laser Machining of Micromechanical Tensile Test Specimens, JOM 73 (2021) 4231–4239. https://doi.org/10.1007/s11837-021-04971-w.
[77] C. Harvey, A.J. Torrez, S. Lam, H. Kim, S.A. Maloy, J.G. Gigax, Demonstration of a High-Throughput Tensile Testing Technique Using Femtosecond Laser-Fabricated Tensile Bars in AISI 316 and Additively Manufactured Grade 91 Steel, JOM 73 (2021) 4240–4247. https://doi.org/10.1007/s11837-021-04964-9.

[78] J.-H. Choi, H. Kim, J.-Y. Kim, K.-H. Lim, B.-C. Lee, G.-D. Sim, Micro-cantilever bending tests for understanding size effect in gradient elasticity, Materials & Design 214 (2022) 110398. https://doi.org/10.1016/j.matdes.2022.110398.
[79] Y. Hu, S. Lam, M.J.K. Lodhi, B.W. Spencer, F. Teng, P. Hosemann, Experimental Evaluation of Interfacial Bonding Strength Between 304 Stainless Steel Substrate and Electrodeposited Nickel Coating Using Mesoscale Mechanical Testing Methods, JOM 77 (2025) 3513–3525. https://doi.org/10.1007/s11837-025-07288-0.
[80] D. Kiener, P. Hosemann, S.A. Maloy, A.M. Minor, In situ nanocompression testing of irradiated copper, Nature Materials 10 (2011) 608–613. https://doi.org/10.1038/nmat3055.
[81] H. Vo, A. Reichardt, C. Howard, M.D. Abad, D. Kaoumi, P. Chou, P. Hosemann, Small-Scale Mechanical Testing on Proton Beam-Irradiated 304 SS from Room Temperature to Reactor Operation Temperature, JOM 67 (2015) 2959–2964. https://doi.org/10.1007/s11837-015-1596-0.
[82] D. Liu, Q. Yu, S. Kabra, M. Jiang, P. Forna-Kreutzer, R. Zhang, M. Payne, F. Walsh, B. Gludovatz, M. Asta, A.M. Minor, E.P. George, R.O. Ritchie, Exceptional fracture toughness of CrCoNi-based medium- and high-entropy alloys at 20 kelvin, Science 378 (2022) 978–983. https://doi.org/10.1126/science.abp8070.
[83] M. Alfreider, M. Meindlhumer, T. Ziegelwanger, R. Daniel, J. Keckes, D. Kiener, Revealing dynamic-mechanical properties of precipitates in a nanostructured thin film using micromechanical spectroscopy, MRS Bulletin 49 (2024) 49–58. https://doi.org/10.1557/s43577-023-00549-w.
[84] M. Alfreider, I. Issa, O. Renk, D. Kiener, Probing defect relaxation in ultra-fine grained Ta using micromechanical spectroscopy, Acta Materialia 185 (2020) 309–319. https://doi.org/10.1016/j.actamat.2019.12.011.
[85] M. Weller, The Snoek relaxation in bcc metals—From steel wire to meteorites, Materials Science and Engineering: A 442 (2006) 21–30. https://doi.org/10.1016/j.msea.2006.02.232.
[86] J.L. Snoek, Effect of small quantities of carbon and nitrogen on the elastic and plastic properties of iron, Physica 8 (1941) 711–733. https://doi.org/10.1016/S0031-8914(41)90517-7.
[87] R. Blackwell, Internal Friction Effects in Tempered Martensite, Nature 211 (1966) 733–734. https://doi.org/10.1038/211733a0.
[88] K.M. Entwistle, The Internal Friction of Metals, Metallurgical Reviews 7 (1962) 175–240. https://doi.org/10.1179/mtlr.1962.7.1.175.
[89] L. Baker, J. Parker, S. Daniel, The use of internal friction techniques as a quality control tool in the mild steel industry, Journal of Materials Processing Technology - J MATER PROCESS TECHNOL 143 (2003) 442–447. https://doi.org/10.1016/S0924-0136(03)00431-X.
[90] C. Goracci, A.U. Tavares, A. Fabianelli, F. Monticelli, O. Raffaelli, P.C. Cardoso, F. Tay, M. Ferrari, The adhesion between fiber posts and root canal walls: Comparison between microtensile and push-out bond strength measurements, Eur. J. Oral Sci. 112 (2004) 353–361. https://doi.org/10.1111/j.1600-0722.2004.00146.x.
[91] D. Frazer, F. Teng, D. Murray, A. Pomo, A. Winston, J.I. Cole, J.F. Jue, J. Giglio, Micro-tensile testing of the bond line in hot isostatic pressed aluminum, Journal of Nuclear Materials 561 (2022) 153532. https://doi.org/10.1016/j.jnucmat.2022.153532.
[92] B.N. Jaya, M.Z. Alam, Small-scale mechanical testing of materials, Current Science 105 (2013) 1073–1099.
[93] T. Ishitani, H. Koike, T. Yaguchi, T. Kamino, Implanted gallium-ion concentrations of focused-ion-beam prepared cross sections, Journal of Vacuum Science & Technology B:

Microelectronics and Nanometer Structures Processing, Measurement, and Phenomena 16 (1998) 1907–1913. https://doi.org/10.1116/1.590106.
[94] C. Lehrer, L. Frey, S. Petersen, M. Mizutani, M. Takai, H. Ryssel, Defects and gallium-contamination during focused ion beam micro machining, in: 2000 International Conference on Ion Implantation Technology Proceedings. Ion Implantation Technology - 2000 (Cat. No.00EX432), IEEE, Alpbach, Austria, 2000: pp. 695–698. https://doi.org/10.1109/IIT.2000.924248.
[95] J. Liu, R. Niu, J. Gu, M. Cabral, M. Song, X. Liao, Effect of Ion Irradiation Introduced by Focused Ion-Beam Milling on the Mechanical Behaviour of Sub-Micron-Sized Samples, Sci Rep 10 (2020) 10324. https://doi.org/10.1038/s41598-020-66564-y.
[96] B.N. Chicbkov, C. Momma, S. Nolte, Femtosecond, picosecond and nanosecond laser ablation of solids, (n.d.).
[97] B. Tordoff, C. Hartfield, A.J. Holwell, S. Hiller, M. Kaestner, S. Kelly, J. Lee, S. Müller, F. Perez-Willard, T. Volkenandt, R. White, T. Rodgers, The LaserFIB: new application opportunities combining a high-performance FIB-SEM with femtosecond laser processing in an integrated second chamber, Appl. Microsc. 50 (2020) 24. https://doi.org/10.1186/s42649-020-00044-5.
[98] B.N. Chicbkov, C. Momma, S. Nolte, Femtosecond, picosecond and nanosecond laser ablation of solids, (n.d.).
[99] C. Momma, B.N. Chichkov, S. Nolte, F. Von Alvensleben, A. Tünnermann, H. Welling, B. Wellegehausen, Short-pulse laser ablation of solid targets, Optics Communications 129 (1996) 134–142. https://doi.org/10.1016/0030-4018(96)00250-7.
[100] Z. He, L. Lei, S. Lin, S. Tian, W. Tian, Z. Yu, F. Li, Metal Material Processing Using Femtosecond Lasers: Theories, Principles, and Applications, Materials 17 (2024) 3386. https://doi.org/10.3390/ma17143386.
[101] P.B. Corkum, F. Brunel, N.K. Sherman, T. Srinivasan-Rao, Thermal Response of Metals to Ultrashort-Pulse Laser Excitation, Phys. Rev. Lett. 61 (1988) 2886–2889. https://doi.org/10.1103/PhysRevLett.61.2886.
[102] Q. McCulloch, J.G. Gigax, P. Hosemann, Femtosecond Laser Ablation for Mesoscale Specimen Evaluation, JOM 72 (2020) 1694–1702. https://doi.org/10.1007/s11837-020-04045-3.
[103] R. Le Harzic, N. Huot, E. Audouard, C. Jonin, P. Laporte, S. Valette, A. Fraczkiewicz, R. Fortunier, Comparison of heat-affected zones due to nanosecond and femtosecond laser pulses using transmission electronic microscopy, Applied Physics Letters 80 (2002) 3886–3888. https://doi.org/10.1063/1.1481195.
[104] Y. Hirayama, M. Obara, Heat-affected zone and ablation rate of copper ablated with femtosecond laser, Journal of Applied Physics 97 (2005) 064903. https://doi.org/10.1063/1.1852692.
[105] S. Valette, E. Audouard, R. Le Harzic, N. Huot, P. Laporte, R. Fortunier, Heat affected zone in aluminum single crystals submitted to femtosecond laser irradiations, Applied Surface Science 239 (2005) 381–386. https://doi.org/10.1016/j.apsusc.2004.06.003.
[106] J.-H. Choi, H. Kim, J.-Y. Kim, K.-H. Lim, B.-C. Lee, G.-D. Sim, Micro-cantilever bending tests for understanding size effect in gradient elasticity, Materials & Design 214 (2022) 110398. https://doi.org/10.1016/j.matdes.2022.110398.
[107] M.J. Pfeifenberger, M. Mangang, S. Wurster, J. Reiser, A. Hohenwarter, W. Pfleging, D. Kiener, R. Pippan, The use of femtosecond laser ablation as a novel tool for rapid micro-

mechanical sample preparation, Materials & Design 121 (2017) 109–118. https://doi.org/10.1016/j.matdes.2017.02.012.
[108] X. Wang, P. Lu, N. Dai, C. Liao, Y. Wang, Q. Zheng, X. Guo, Q. Zhang, Femtosecond laser direct fabrication of metallic microcantilevers for a micro-corrosion-fatigue test, J. Micromech. Microeng. 17 (2007) 1307–1313. https://doi.org/10.1088/0960-1317/17/7/013.
[109] C.G. Wilson, The plastic deformation of single crystals of gallium, Journal of the Less Common Metals 5 (1963) 245–257. https://doi.org/10.1016/0022-5088(63)90030-4.
[110] X. Wang, X. Lu, W. Xiao, X. Liu, L. Li, H. Chang, Z. Yu, X. Yang, L. Chang, K. Sun, Q. Wang, C. Jiao, L. Hu, Fast Solidification of Pure Gallium at Room Temperature and its Micromechanical Properties, Advanced Materials Interfaces 10 (2023) 2202100. https://doi.org/10.1002/admi.202202100.
[111] S. Lam, D. Frazer, F. Cappia, M. Nelson, S. Samuha, S. Pitts, B. Harris, P. Hosemann, Length scale effects of micro- and meso-scale tensile tests of unirradiated and irradiated Zircaloy-4 cladding, Journal of Nuclear Materials 604 (2025) 155469. https://doi.org/10.1016/j.jnucmat.2024.155469.
[112] G. Schnell, H. Lund, S. Bartling, C. Polley, A. Riaz, V. Senz, A. Springer, H. Seitz, Heat accumulation during femtosecond laser treatment at high repetition rate – A morphological, chemical and crystallographic characterization of self-organized structures on Ti6Al4V, Applied Surface Science 570 (2021) 151115. https://doi.org/10.1016/j.apsusc.2021.151115.
[113] X. Jia, X. Zhao, Ultrafast laser ablation of copper with GHz bursts: A numerical study on the effects of repetition rate, pulse number and burst fluence on ablation efficiency and heat-affected zone, Optics & Laser Technology 158 (2023) 108803. https://doi.org/10.1016/j.optlastec.2022.108803.
[114] E. Tenckhoff, Deformation mechanisms, texture, and anisotropy in zirconium and zircaloy, (1988). https://www.osti.gov/biblio/5932937.
[115] D. Kamerman, F. Cappia, K. Wheeler, P. Petersen, E. Rosvall, T. Dabney, H. Yeom, K. Sridharan, M. Ševeček, J. Schulthess, Development of axial and ring hoop tension testing methods for nuclear fuel cladding tubes, Nuclear Materials and Energy 31 (2022) 101175. https://doi.org/10.1016/j.nme.2022.101175.
[116] R. Daum, S. Majumda, H. Tsai, T. Bray, D. Koss, A. Motta, M. Billone, Mechanical Property Testing of Irradiated Zircaloy Cladding Under Reactor Transient Conditions, in: Small Specimen Test Techniques: Fourth Volume, ASTM International100 Barr Harbor Drive, PO Box C700, West Conshohocken, PA 19428-2959, 2002: pp. 195–210. https://doi.org/10.1520/STP10821S.
[117] M. Nelson, S. Samuha, D. Kamerman, P. Hosemann, Temperature-Dependent Mechanical Anisotropy in Textured Zircaloy Cladding, Journal of Nuclear Materials 595 (2024) 155045. https://doi.org/10.1016/j.jnucmat.2024.155045.
[118] D. Kamerman, M. Nelson, Multiaxial Plastic Deformation of Zircaloy-4 Nuclear Fuel Cladding Tubes, Nuclear Technology 209 (2023) 872–886. https://doi.org/10.1080/00295450.2022.2160174.
[119] Standard Test Methods of Tension Testing of Metallic Materials (ASTM E8/E8M), (2016). https://www.astm.org/e0008_e0008m-16a.html.
[120] H.-B. Ma, J. Yan, Y.-H. Zhao, T. Liu, Q.-S. Ren, Y.-H. Liao, J.-D. Zuo, G. Liu, M.-Y. Yao, Oxidation behavior of Cr-coated zirconium alloy cladding in high-temperature steam above 1200 °C, Npj Mater Degrad 5 (2021) 7. https://doi.org/10.1038/s41529-021-00155-8.

[121] B.N. Jaya, M.Z. Alam, Small-scale mechanical testing of materials, Current Science 105 (2013) 1073–1099.
[122] S. Wurster, R. Treml, R. Fritz, M.W. Kapp, E. Langs, M. Alfreider, C. Ruhs, P.J. Imrich, G. Felber, D. Kiener, Novel Methods for the Site Specific Preparation of Micromechanical Structures: Presented at the Metallography Conference 2014 in Leoben, Austria, Practical Metallography 52 (2015) 131–146. https://doi.org/10.3139/147.110331.
[123] T.T. Zhu, A.J. Bushby, D.J. Dunstan, Materials mechanical size effects: a review, Materials Technology 23 (2008) 193–209. https://doi.org/10.1179/175355508X376843.
[124] R. Le Harzic, N. Huot, E. Audouard, C. Jonin, P. Laporte, S. Valette, A. Fraczkiewicz, R. Fortunier, Comparison of heat-affected zones due to nanosecond and femtosecond laser pulses using transmission electronic microscopy, Applied Physics Letters 80 (2002) 3886–3888. https://doi.org/10.1063/1.1481195.
[125] A. Mouskeftaras, O. Koritsoglou, G. Duchateau, O. Utéza, From Femtosecond Laser-Induced Plasma Formation Inside Glass to Stress Wave Generation and Propagation: Experiments and Modelling, in: 2023 Conference on Lasers and Electro-Optics Europe & European Quantum Electronics Conference (CLEO/Europe-EQEC), 2023: pp. 1–1. https://doi.org/10.1109/CLEO/Europe-EQEC57999.2023.10231963.
[126] J.G. Gigax, O. El-Atwani, Q. McCulloch, B. Aytuna, M. Efe, S. Fensin, S.A. Maloy, N. Li, Micro- and mesoscale mechanical properties of an ultra-fine grained CrFeMnNi high entropy alloy produced by large strain machining, Scripta Materialia 178 (2020) 508–512. https://doi.org/10.1016/j.scriptamat.2019.11.042.
[127] Kate Richardson, Heather Medema, ADVANCED FUELS CAMPAIGN 2020 Accomplishments, Idaho National Laboratory, 2020.
[128] F. Cappia, Non-destructive Examinations of ATF-2 Baseline Rodlets, 2020. https://doi.org/10.2172/1637596.
[129] D. Kamerman, B. Durtschi, N. Woolstenhulme, B. Curnutt, T. Labossiere-Hickman, R. Skifton, F. Cappia, An Integral Light Water Reactor Irradiation Experiment for Accident Tolerant Fuel Development, (2023). https://doi.org/10.2139/ssrn.4341149.
[130] Jean-Jacques Fundenberger, Benoit Beausir, Analysis Tools for Electron and X-ray diffraction ATEX-software, (2017).
[131] M. Nelson, S. Samuha, B. Kombaiah, D. Kamerman, P. Hosemann, Enhanced stress relaxation behavior via basal 〈a〉 dislocation activity in Zircaloy-4 cladding, Journal of Nuclear Materials 601 (2024) 155337. https://doi.org/10.1016/j.jnucmat.2024.155337.
[132] C.L. Whitmarsh, REVIEW OF ZIRCALOY-2 AND ZIRCALOY-4 PROPERTIES RELEVANT TO N.S. SAVANNAH REACTOR DESIGN, 1962. https://doi.org/10.2172/4827123.
[133] A. Hermann, M. Martin, P. Porschke, S. Yagnik, DUCTILITY DEGRADATION OF IRRADIATED FUEL CLADDING, (n.d.).
[134] H.C. Chu, S.K. Wu, K.F. Chien, R.C. Kuo, Effect of radial hydrides on the axial and hoop mechanical properties of Zircaloy-4 cladding, Journal of Nuclear Materials 362 (2007) 93–103. https://doi.org/10.1016/j.jnucmat.2006.11.008.
[135] S. Bang, H. Kim, J. Noh, D. Kim, K. Keum, Y. Lee, Temperature-dependent axial mechanical properties of Zircaloy-4 with various hydrogen amounts and hydride orientations, Nuclear Engineering and Technology 54 (2022) 1579–1587. https://doi.org/10.1016/j.net.2021.11.007.

[136] W.F. Hosford, ed., Strain-Rate and Temperature Dependence of Flow Stress, in: Solid Mechanics, Cambridge University Press, Cambridge, 2010: pp. 84–101. https://doi.org/10.1017/CBO9780511841422.007.
[137] R. Roy, F. Long, M.R. Daymond, A mechanistic study of grain boundary behaviour during irradiation-induced growth in zirconium, Acta Materialia 276 (2024) 120075. https://doi.org/10.1016/j.actamat.2024.120075.
[138] A. Dong, H. Vo, E. Olivas, J. Bickel, C. Hardie, P. Hosemann, S. Maloy, The effect of sample thickness on micro-mesoscale tensile properties of 304SS, HT-9, and CuCrZr, Journal of Nuclear Materials 575 (2023) 154207. https://doi.org/10.1016/j.jnucmat.2022.154207.
[139] R.L. Klueh, D.R. Harries, High-chromium ferritic and martensitic steels for nuclear applications, ASTM, W. Conshohocken, PA, 2001.
[140] P. Hosemann, J.G. Swadener, D. Kiener, G.S. Was, S.A. Maloy, N. Li, An exploratory study to determine applicability of nano-hardness and micro-compression measurements for yield stress estimation, Journal of Nuclear Materials 375 (2008) 135–143. https://doi.org/10.1016/j.jnucmat.2007.11.004.
[141] A. Granato, K. Lücke, Theory of Mechanical Damping Due to Dislocations, Journal of Applied Physics 27 (1956) 583–593. https://doi.org/10.1063/1.1722436.
[142] A.S. Nowick, Internal Friction and Dynamic Modulus of Cold-Worked Metals, Journal of Applied Physics 25 (1954) 1129–1134. https://doi.org/10.1063/1.1721827.
[143] I. Golovin, Blanter-Golovin-Neuhauser-Sinning, Internal Friction in Metallic Materials, 2007. https://doi.org/10.1007/978-3-540-68758-0.
[144] T.-S. Kê, Internal friction of cold-worked metals at various temperatures, JOM 2 (1950) 575–580. https://doi.org/10.1007/BF03399034.
[145] R.P. Krupitzer, C.J. Szczepanski, R. Gibala, Effects of preferred orientation on Snoek phenomena in commercial steels, Materials Science and Engineering: A 521–522 (2009) 43–46. https://doi.org/10.1016/j.msea.2008.09.130.
[146] M. Alfreider, I. Issa, O. Renk, D. Kiener, Probing defect relaxation in ultra-fine grained Ta using micromechanical spectroscopy, Acta Materialia 185 (2020) 309–319. https://doi.org/10.1016/j.actamat.2019.12.011.
[147] J.G. Gigax, H. Vo, Q. McCulloch, M. Chancey, Y. Wang, S.A. Maloy, N. Li, P. Hosemann, Micropillar compression response of femtosecond laser-cut single crystal Cu and proton irradiated Cu, Scripta Materialia 170 (2019) 145–149. https://doi.org/10.1016/j.scriptamat.2019.05.004.
[148] L. Morsdorf, E. Emelina, B. Gault, M. Herbig, C.C. Tasan, Carbon redistribution in quenched and tempered lath martensite, Acta Materialia 205 (2021) 116521. https://doi.org/10.1016/j.actamat.2020.116521.
[149] H. Ino, S. Takagi, T. Sugeno, On the relaxation strength of the snoek peak, Acta Metallurgica 15 (1967) 29–34. https://doi.org/10.1016/0001-6160(67)90152-6.
[150] V.H. Carneiro, J. Grilo, D. Soares, I. Duarte, H. Puga, The Influence of Precipitation Hardening on the Damping Capacity in Al–Si–Mg Cast Components at Different Strain Amplitudes, Metals 12 (2022) 804. https://doi.org/10.3390/met12050804.
[151] G. Schoeck, Internal Friction Due to Precipitation, Physica Status Solidi (b) 32 (1969) 651–658. https://doi.org/10.1002/pssb.19690320216.
[152] S. Li, L. Deng, X. Wu, H. Wang, Y. Min, Low-frequency internal friction investigating of the carbide precipitation in solid solution during tempering in high alloyed martensitic steel, Materials Science and Engineering: A 527 (2010) 6899–6903. https://doi.org/10.1016/j.msea.2010.07.097.

[153] S.A. Kim, W.L. Johnson, Elastic constants and internal friction of martensitic steel, ferritic-pearlitic steel, and α-iron, NIST (2007) 633–639.
[154] T. Hirose, T. Nozawa, R.E. Stoller, D. Hamaguchi, H. Sakasegawa, H. Tanigawa, H. Tanigawa, M. Enoeda, Y. Katoh, L.L. Snead, Physical properties of F82H for fusion blanket design, Fusion Engineering and Design 89 (2014) 1595–1599. https://doi.org/10.1016/j.fusengdes.2013.12.005.
[155] X. Li, S. Schönecker, X. Li, J. Zhao, L. Vitos, The influence of temperature on the elastic properties of body-centered cubic reduced activation steels, Materials & Design 197 (2021) 109282. https://doi.org/10.1016/j.matdes.2020.109282.
[156] S.A. Kim, W.L. Johnson, Elastic constants and internal friction of martensitic steel, ferritic-pearlitic steel, and α-iron, Materials Science and Engineering: A 452–453 (2007) 633–639. https://doi.org/10.1016/j.msea.2006.11.147.
[157] M. Souissi, H. Numakura, Elastic Properties of Fe–C and Fe–N Martensites, ISIJ International 55 (2015) 1512–1521. https://doi.org/10.2355/isijinternational.55.1512.
[158] K.M. Knowles, The Plane Strain Young's Modulus in Cubic Materials, J Elast 128 (2017) 147–173. https://doi.org/10.1007/s10659-017-9621-x.
[159] Z. Wang, F. Li, Characterization of Quenching and Tempering of a Martensitic Steel Based on Precise Internal Friction Measurement Using Electromechanical Impedance, Physica Status Solidi (a) n/a (n.d.) 2500028. https://doi.org/10.1002/pssa.202500028.
[160] T. Miura, K. Fujii, K. Fukuya, M. Ando, H. Tanigawa, Micro-tensile testing of reduced-activation ferritic steel F82H irradiated with Fe and He ions, Nuclear Materials and Energy 17 (2018) 24–28. https://doi.org/10.1016/j.nme.2018.08.004.
[161] T.-Y. Chang, S. Lam, D. Frazer, F. Teng, Y. Wang, H. Gietl, P. Hosemann, S. Pitts, The role of specimen size and grain boundary characteristics in the yield strength of tungsten in microtensile tests, Fusion Engineering and Design 219 (2025) 115293. https://doi.org/10.1016/j.fusengdes.2025.115293.
[162] Introduction to Dislocations, Elsevier, 2011. https://doi.org/10.1016/C2009-0-64358-0.
[163] C. Du, F. Maresca, M.G.D. Geers, J.P.M. Hoefnagels, Ferrite slip system activation investigated by uniaxial micro-tensile tests and simulations, Acta Materialia 146 (2018) 314–327. https://doi.org/10.1016/j.actamat.2017.12.054.
[164] Slip geometry: the critical resolved shear stress, (n.d.). https://www.doitpoms.ac.uk/tlplib/slip/slip_geometry.php (accessed November 10, 2025).
[165] J.S.K.-L. Gibson, R. Pei, M. Heller, S. Medghalchi, W. Luo, S. Korte-Kerzel, Finding and Characterising Active Slip Systems: A Short Review and Tutorial with Automation Tools, Materials (Basel) 14 (2021) 407. https://doi.org/10.3390/ma14020407.
[166] T.V. Phan, Grain scale simulation of local deformation behavior, Asia Pacific Journal on Computational Engineering 1 (2014) 10. https://doi.org/10.1186/s40540-014-0010-7.
[167] K. Shiba, R.L. Klueh, Y. Miwa, J.P. Robertson, A. Hishinuma, Tensile behavior of F82H with and without spectral tailoring, Journal of Nuclear Materials 283–287 (2000) 358–361. https://doi.org/10.1016/S0022-3115(00)00362-7.
[168] M. Ando, H. Tanigawa, H. Kurotaki, Y. Katoh, Mechanical properties of neutron irradiated F82H using micro-tensile testing, Nuclear Materials and Energy 16 (2018) 258–262. https://doi.org/10.1016/j.nme.2018.07.008.
[169] A.F. Rowcliffe, J.P. Robertson, R.L. Klueh, K. Shiba, D.J. Alexander, M.L. Grossbeck, S. Jitsukawa, Fracture toughness and tensile behavior of ferritic–martensitic steels irradiated at low

temperatures, Journal of Nuclear Materials 258–263 (1998) 1275–1279. https://doi.org/10.1016/S0022-3115(98)00163-9.
[170] H.T. Vo, O. Anderoglu, P. Hosemann, S.A. Maloy, The effects of microstructures and radiation damage on the deformation behavior of a HT-9 alloy using microtensile testing, Materials Characterization 174 (2021) 110972. https://doi.org/10.1016/j.matchar.2021.110972.

Chapter 9

Appendices

Appendix 1: Closing Statement on Fusion Energy

During my studies, I had the opportunity to listen to a lecture from UC Berkeley's now retired professor for plasma physics of MCF systems. At the end of the talk, he responded to a question regarding the success of fusion energy. Now at the end of his decades long career focused on studying nuclear fusion and knowing the current downtrodden state of fusion energy, he responded that of course fusion energy was successful: the technology funded his whole career, his children's education, and gave him a fulfilled life. I think to look at fusion energy as a black and white issue of success or failure is far too simple and a steadfast fixation on the end goal diminishes the importance of the lessons learned along the way. The Apollo 11 landing on the moon while being a monumental feat, obscured the even more important research on integrated circuits, digital computing, and GPS which happened as a result of the space program. Fusion energy lies at the intersection of politics, global warming, geopolitical struggles, economics, computing, physics, and engineering. If ITER succeeds in producing commercialized fusion energy, I think the success lies not within the cheap electricity it produces. Rather I think the science developed along the way, the great scientists it births, and the physical proof that people can put aside their differences and work together on the hardest challenge facing humanity will prove to be vastly more important.

Appendix 2: CV

Sebastian Lam

Graduate Student Researcher & PhD Candidate, Department of Nuclear Engineering, The University of California, Berkeley
Email: srlam323@berkeley.edu

Education .....

Ph.D. Nuclear Engineering (Minor: Materials Science and Engineering)
The University of California, Berkeley, *Expected 2025*
Dissertation: *The Effects of Carbides on the Mechanical Properties of Martensitic Interfaces in F82H Fusion Steel*
Advisor: *Professor Peter Hosemann*
B.S. Joint Materials Science and Engineering/Nuclear Engineering
The University of California, Berkeley, *2021*

Professional Employment & Research Experience .....

Engineering Intern ..... ***May 2016 – Aug 2017***
Engineering & Operations, Abbott Laboratories

Undergraduate Researcher ..... ***Jan 2018 – May 2021***
Hosemann Nuclear Materials Group, Nuclear Engineering, The University of California, Berkeley

- Investigated the corrosion behavior of SiC in nuclear environments and SiC based CVD/PVD coatings for nuclear applications using TEM
- Designed techniques for in-situ mechanical testing of SiC fibers

Undergraduate Researcher ..... ***Apr 2020 – Aug 2020***
MST-8, Los Alamos National Laboratory - Texas A&M University

- Developed a FEM model for oxide growth in FeCrAl alloys in liquid metal

Graduate Visiting Scholar ..... ***Apr 2021 – Aug 2021***
Center for Integrated Nanotechnologies/MST-8, Los Alamos National Laboratory

- Characterized liquid metal corrosion mechanisms of FeCrAl alloys
- Established a high throughput method for testing femtosecond laser machined meso-mechanical test specimen

Graduate Visiting Scholar ..... ***Apr 2024 – Sep 2024***
Department of Materials Physics, Montanuniversität Leoben

- Used micromechanical spectroscopy to probe the resonance frequency of microcantilevers and quantify energy dissipation evolution in RAFM steels for fusion reactors.

Graduate Student Researcher ..... ***May 2021 – Present***
Hosemann Nuclear Materials Group, Nuclear Engineering, The University of California, Berkeley

- Used small scale mechanical testing to probe the mechanical effects of carbides in ferritic/martensitic steels at martensitic interfaces
- Developed and designed a femtosecond laser system for manufacturing ion traps and microfluidic devices
- Investigated radiation effects of steels in nuclear fusion environments
- Mechanically investigated Additively Manufactured PBF steels for property gradients

Skills

Data Analysis/Programming: Python, MATLAB, CAD
Materials Characterization & Techniques:

- Sample Preparation
- Scanning Electron Microscopy (SEM)
- Focused Ion Beam Milling (FIB)
- Energy Dispersive Spectroscopy (EDS)
- Electron Backscatter Diffraction (EBSD)
- X-Ray Diffraction (XRD)
- Laser Induced Breakdown Spectroscopy (LIBS)
- Laser Ablation Inductively Coupled Plasma Mass Spectrometry (LAICPMS)
- X-Ray Photoelectron Spectroscopy (XPS)
- Powder Bed Fusion Additive Manufacturing (PBF-AM)
- Micro- and Macro-mechanical testing

Publications

Chang, Tzu-Yi, **Sebastian Lam,** David Frazer, Fei Teng, Yachun Wang, Hanns Gietl, Peter Hosemann, and Stephanie Pitts. 2025. "The Role of Specimen Size and Grain Boundary Characteristics in the Yield Strength of Tungsten in Microtensile Tests." *Fusion Engineering and Design* 219: 115293. doi:10.1016/j.fusengdes.2025.115293.

Dong, A., J. Duckering, J. Peterson, **S. Lam,** D. Routledge, and P. Hosemann. 2021. "Femtosecond Laser Machining of Micromechanical Tensile Test Specimens." *JOM* 73(12): 4231–39. doi:10.1007/s11837-021-04971-w.

Harvey, Cayla, Avery J. Torrez, **Sebastian Lam,** Hyosim Kim, Stuart A. Maloy, and Jonathan G. Gigax. 2021. "Demonstration of a High-Throughput Tensile Testing Technique Using Femtosecond Laser-Fabricated Tensile Bars in AISI 316 and Additively Manufactured Grade 91 Steel." *JOM* 73(12): 4240–47. doi:10.1007/s11837-021-04964-9.

Hosemann, P., R. Auguste, **S. Lam,** M. Butterling, M. O. Liedke, A. G. Attallah, E. Hirschmann, et al. 2021. "Defect Characterization Using Positron Annihilation Spectroscopy on Laser-Ablated Surfaces." *JOM* 73(12): 4221–30. doi:10.1007/s11837-021-04965-8.

Hu, Yuxin, **Sebastian Lam,** M. J. K. Lodhi, Benjamin W. Spencer, Fei Teng, and Peter Hosemann. 2025. "Experimental Evaluation of Interfacial Bonding Strength Between 304 Stainless Steel Substrate and Electrodeposited Nickel Coating Using Mesoscale Mechanical Testing Methods." *JOM* 77(5): 3513–25. doi:10.1007/s11837-025-07288-0.

Lam, S., D. Frazer, F. Cappia, M. Nelson, S. Samuha, S. Pitts, B. Harris, and P. Hosemann. 2025. "Length Scale Effects of Micro- and Meso-scale Tensile Tests of Unirradiated and Irradiated Zircaloy-4 Cladding." *Journal of Nuclear Materials* 604: 155469. doi:10.1016/j.jnucmat.2024.155469.

Lam, S., M. Alfreider, D. Kiener, P. Hosemann, The proof of minimal heat impact during femtosecond machining of small scale mechanical test samples – example gallium, *(2025 Planned)*

Lam, S., M. Alfreider, D. Kiener, P. Hosemann, Understanding energy dissipation mechanisms of carbon in F82H using micromechanical spectroscopy, *(2025 Planned)*

Lam, S., P. Hosemann, Micromechanical effects of carbide nucleation at martensitic interfaces in F82H, *(2025 Planned)*

Lee, Andrew C., Adam Barsotti, Jiyun Kang, Abhinav Parakh, Oscar Paz-Suaznabar, Andrew Sleugh, **Sebastian Lam,** et al. 2025. "Direct Observation of Strain-Enhanced Hydrogen Segregation and Failure at High-Angle Grain Boundaries in Nickel." *Acta Materialia* 297: 121358. doi:10.1016/j.actamat.2025.121358.

Lee, Andrew C., Abhinav Parakh, **Sebastian Lam,** Andrew Sleugh, Ottman Tertuliano, David Doan, Johanna Nelson Weker, Peter Hosemann, and X. Wendy Gu. 2023. "Dynamic Fracture Processes in Hydrogen Embrittled Iron." *Acta Materialia* 259: 119234. doi:10.1016/j.actamat.2023.119234.

Lee, Andrew C., Abhinav Parakh, Andrew Sleugh, Ottman A. Tertuliano, **Sebastian Lam,** Johanna Nelson Weker, Peter Hosemann, and X. Wendy Gu. 2023. "Detection of Voids in Hydrogen Embrittled Iron Using Transmission X-Ray Microscopy." *International Journal of Hydrogen Energy* 48(5): 1968–78. doi:10.1016/j.ijhydene.2022.10.059.

Loeb, Abraham, Toby Adamson, Sophie Bergstrom, Richard Cloete, Shai Cohen, Kevin Conrad, Laura Domine, **Sebastian Lam,** et al. 2023. "Discovery of Spherules of Likely Extrasolar Composition in the Pacific Ocean Site of the CNEOS 2014-01-08 (IM1) Bolide." doi:10.48550/arXiv.2308.15623.

Mun. J, J. Park, J. Hong, **S. Lam,** P. Hosemann, H. Ryu.. 2025. “Smallscale mechanical testing of interfacial toughness in Cr-Coated zircaloy-4”, *(2025 Planned)*

Niu, Tongjun, Ross Lee, **Sebastian Lam,** Joseph Hafen, Steven Lukow, Nan Li, Peter Hosemann, and Jonathan Gigax. 2025. “A Novel Machine Learning-Driven Approach to High Throughput Mechanical Testing.” *JOM* 77(4): 2121–33. doi:10.1007/s11837-024-07063-7.

Samuha, S., **S. Lam,** J. Bickel, A. Ben-Bassat, P. Balu, C. Grigoropoulos, P. Chou, P. Hosemann. Laser-induced microstructural engineering in cold worked 316L stainless steel: A combined mechanistic and modeling perspective *(2025 Planned)*

Schoell, Ryan, Joey Kabel, **Sebastian Lam,** Amit Sharma, Johann Michler, Peter Hosemann, and Djamel Kaoumi. 2022. “Corrosion Behavior of a Series of Combinatorial Physical Vapor Deposition Coatings on SiC in a Simulated Boiling Water Reactor Environment.” *Journal of Nuclear Materials* 572: 154022. doi:10.1016/j.jnucmat.2022.154022

Appendix 3: Links to SSMT Videos

F82H Micromechanical Spectroscopy Video:

https://youtu.be/-TK3IxaV7mc

F82H Microtensile Compilation Video:

https://youtu.be/2dZtCXcaUyk

KW Tensile Testing for Compliance Correction Video:

https://youtu.be/HKChSAs6iig